



ANNUAL REVIEWS **Further**

Click [here](#) to view this article's online features:

- Download figures as PPT slides
- Navigate linked references
- Download citations
- Explore related articles
- Search keywords

The Galaxy in Context: Structural, Kinematic, and Integrated Properties

Joss Bland-Hawthorn¹ and Ortwin Gerhard²

¹Sydney Institute for Astronomy, School of Physics, University of Sydney,
New South Wales 2006, Australia; email: jbh@physics.usyd.edu.au

²Max Planck Institute for Extraterrestrial Physics, 85741 Garching, Germany;
email: gerhard@mpe.mpg.de

Annu. Rev. Astron. Astrophys. 2016. 54:529–96

First published online as a Review in Advance on
August 8, 2016

The *Annual Review of Astronomy and Astrophysics* is
online at astro.annualreviews.org

This article's doi:
[10.1146/annurev-astro-081915-023441](https://doi.org/10.1146/annurev-astro-081915-023441)

Copyright © 2016 by Annual Reviews.
All rights reserved

Keywords

Galaxy: structural components, stellar kinematics, stellar populations,
dynamics, evolution, Local Group, cosmology

Abstract

Our Galaxy, the Milky Way, is a benchmark for understanding disk galaxies. It is the only galaxy whose formation history can be studied using the full distribution of stars from faint dwarfs to supergiants. The oldest components provide us with unique insight into how galaxies form and evolve over billions of years. The Galaxy is a luminous (L_*) barred spiral with a central box/peanut bulge, a dominant disk, and a diffuse stellar halo. Based on global properties, it falls in the sparsely populated “green valley” region of the galaxy color-magnitude diagram. Here we review the key integrated, structural and kinematic parameters of the Galaxy, and point to uncertainties as well as directions for future progress. Galactic studies will continue to play a fundamental role far into the future because there are measurements that can only be made in the near field and much of contemporary astrophysics depends on such observations.

Contents

1. PROLOGUE	530
2. THE GALAXY IN CONTEXT	534
2.1. Environment and Evolution	534
2.2. Galaxy Classification and Integrated Properties	535
3. GALACTIC CENTER	537
3.1. Location	537
3.2. Distance	538
3.3. Solar Offset and Galactic Plane	543
3.4. Black Hole and Solar Angular Velocity	544
4. INNER GALAXY	545
4.1. Nuclear Star Cluster and Stellar Disk	545
4.2. Bulge	548
4.3. The “Long Bar” Outside the Bulge	553
4.4. Pattern Speed	555
5. STELLAR DISK	556
5.1. Stellar Photometry	558
5.2. Stellar Chemistry	562
5.3. Stellar Kinematics	564
5.4. Stellar Dynamics	568
5.5. Outer Disk	572
6. HALO	572
6.1. Stellar Halo	573
6.2. Hot Halo	576
6.3. Dark Halo	578
6.4. Rotation Curve and Baryon Fraction Profile	581
7. CONCLUDING REMARKS	583

1. PROLOGUE

Galactic studies are a fundamental cornerstone of contemporary astrophysics. Nowadays, we speak of near-field cosmology in which detailed studies of the Galaxy underlie our understanding of universal processes over cosmic time (Freeman & Bland-Hawthorn 2002). Within the context of the cold dark matter paradigm, the Galaxy built up over billions of years through a process of hierarchical accretion (see **Figure 1**). Our Galaxy has recognizable components that are likely to have emerged at different stages of the formation process. In particular, the early part of the bulge may have collapsed first, seeding the early stages of a massive black hole, followed by a distinct phase that gave rise to the thick disk. The inner halo may have formed about the same time, whereas the outer halo has built up later through the progressive accretion of shells of material over cosmic time (Prada et al. 2006). The dominant thin disk reflects a different form of accretion over the same long time frame (Brook et al. 2012).

We live in an age when vast surveys have been carried out across the entire sky in many wave bands. At optical and IR wavelengths, billions of stars have been cataloged with accurate photometric magnitudes and colors (Skrutskie et al. 2006, Ivezić et al. 2012, Saito et al. 2012). But only a fraction of these stars have high-quality spectral classifications, radial velocities, and distances, with an even smaller fraction having useful elemental abundance determinations. The

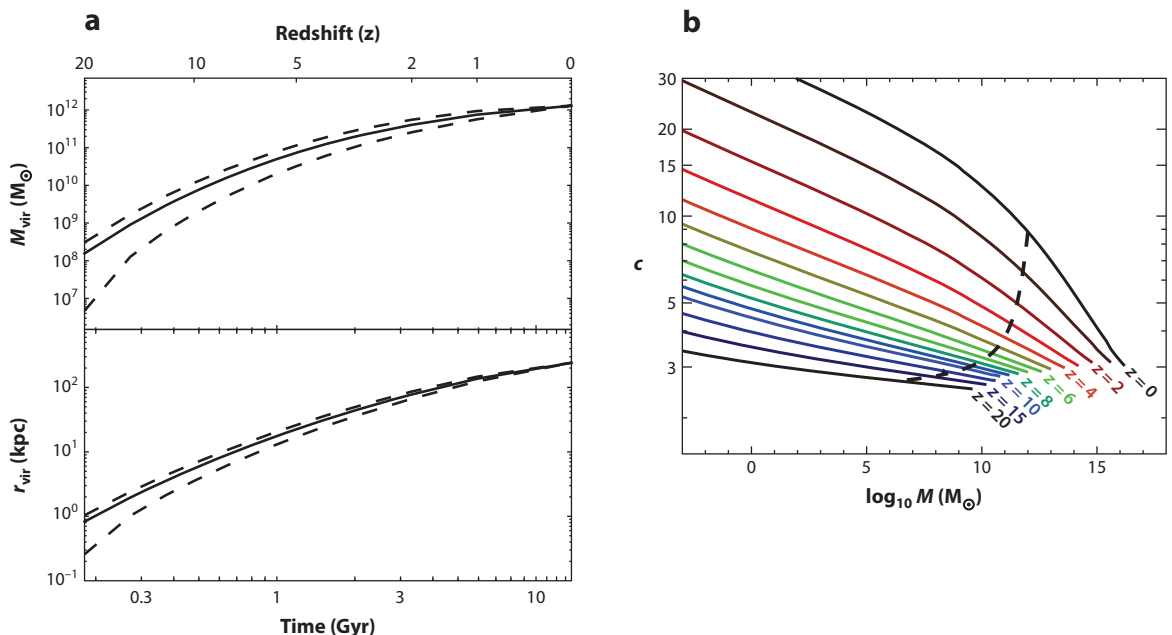


Figure 1

(a) The estimated growth of the Galaxy's virial mass (M_{vir}) and radius (r_{vir}) from $z = 20$ to the present day, $z = 0$. Throughout this review, we use $b = 0.7$, $\Omega_{\text{M}} = 0.3$, and $\Omega_{\Lambda} = 0.7$. The virial radius at any epoch is the approximate extent over which the growing Galaxy has stabilized. This plot was derived from 5,000 runs of the tree merger code of Parkinson et al. (2008): the dashed lines encompass 67% of the predicted halos at each epoch (1σ uncertainty). (b) The discrete curves show how the Navarro, Frenk & White (NFW) concentration parameter c depends on halo mass M_{vir} as a function of cosmic epoch, indicated by the different line colors. If Galactic dark matter is correctly described by an NFW halo, the dashed line shows how c evolves with mass (and therefore cosmic time). The central regions form early on, and most of the accreted matter settles to the outer halo. Adapted from Correa et al. (2015) with permission.

difficulty of measuring a star's age continues to hamper progress in Galactic studies, but this stumbling block will be partly offset by the ESA *Gaia* astrometric survey already under way. By the end of the decade, this mission will have measured accurate distances and velocity vectors for many millions of stars arising from all major components of the Galaxy (de Bruijne et al. 2015). In light of this impending data set, we review our present understanding of the main dynamical and structural parameters that describe our home, the Milky Way.

We run into a problem familiar to cartographers. How is one to describe the complexity of the Galaxy? No two galaxies are identical; even the best morphological analogues with the Milky Way have important differences (**Figure 2**). Historically, astronomers have resorted to defining discrete components with the aim of measuring their structural parameters (see **Table 1**). We continue to see value in this approach and proceed to define what we mean by each subsystem and the best estimates that can be made at the present time. In reality, these “components” exhibit strong overlap by virtue of sharing the same evolving Galactic potential (e.g., Guedes et al. 2013) and the likelihood that stars migrate far from their formation sites (Sellwood & Binney 2002, Minchev & Famaey 2010).

Even with complete data (density field, distribution function, chemistry), it is unlikely that any one component can be entirely separated from another. In particular, how are we to separate the bar/bulge from the inner disk and inner halo? A distinct possibility is that most of our small bulge (compared to M31) has formed through a disk instability associated with bar formation, rather

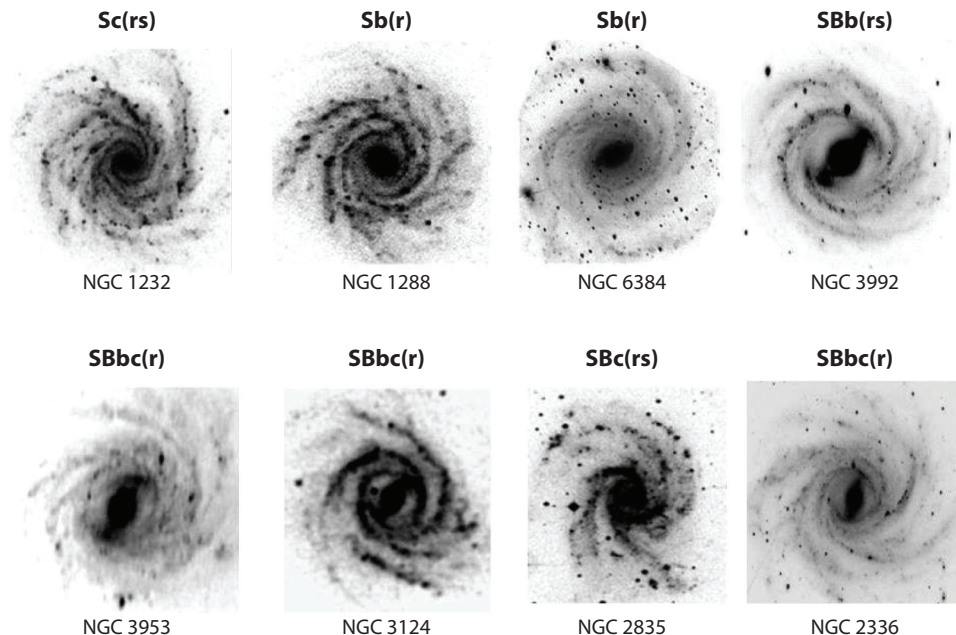


Figure 2

Milky Way analogues. A selection of galaxies that broadly resemble the Galaxy (Efremov 2011). All images have been rectified to a flat projection. Classifications within the de Vaucouleurs morphological classification scheme are also shown.

than during a dissipational early collapse phase. The same challenge exists in separating the thin disk from the thick disk. Some have argued for a gradual transition but there is now good evidence that a major part of the thick disk is chemically distinct from the dominant thin disk, suggesting a different origin. In this context, Binney (2013) has argued that the Galaxy’s stellar populations are better described by phase-space distribution functions (DFs) that are self-consistent with the underlying gravitational potential (Section 5).

Our goal here is to identify the useful structural and kinematic parameters that aid comparison with other galaxies and place our Galaxy in context. These “measurables” are also important for comparing with numerical simulations of synthetic galaxies. A simulator runs a disk simulation and looks to compare the evolutionary phase where the bar/bulge instability manifests itself. In principle, only a statistically good fit is needed without resorting to any parameterization (Sharma et al. 2011). But in practice, the comparison is likely to involve global properties like rotation curves, scale lengths, total mass (gas, stars, dark matter), stellar abundances, and the star-formation history. Here we focus on establishing what the best estimates are for the Galaxy’s global properties and the parameters that describe its traditional components.

Kerr & Lynden-Bell (1986) revisited the 1964 IAU (International Astronomical Union) standards for the Sun’s distance and circular velocity ($R_0 = 10$ kpc, $\Theta_0 = 250$ km s⁻¹) relative to the Galactic Center and proposed a downward revision ($R_0 = 8.5$ kpc, $\Theta_0 = 220$ km s⁻¹). Both values can now be revised further to reflect the new observational methods at our disposal three decades on. Our goal in this review is to provide an at-a-glance summary of the key structural and kinematic parameters to aid the increasing focus on Galactic studies. For reasons that become clear in later sections, we cannot yet provide summary values that are all internally consistent in

Table 1 Description of Galactic parameters

R_0	Distance of Sun from the Galactic Center [3.2]
z_0	Distance of Sun from the Galactic Plane [3.3]
Θ_0, Ω_0	Circular speed, angular velocity at Sun with respect to Galactic Center [3.4, 6.4.2]
$U_\odot, V_\odot, W_\odot$	U, V, W component of solar motion with respect to LSR [5.3.3]
\mathbf{v}_\odot	Solar motion with respect to LSR [5.3.3]
V_{LSR}	Possible LSR streaming motion with respect to Θ_0 [5.3.3, 6.4.2]
A, B	Oort's constants [6.4.2]
r_{vir}	Galactic virial radius [6.3]
$M_{\text{vir}}, M_{\text{vir,timing}}$	Galactic virial mass, virial timing mass [6.3]
M_\star, \dot{m}_\star	Galactic stellar mass, global star-formation rate [6.4, 2.2]
$M_{\text{bary}}, f_{\text{bary}}^a$	Galactic baryon mass, baryon fraction [6.2, 6.4.3]
$M_{\text{b}}^{\text{dyn}}, M_{\text{b}}^\star, M_{\text{clb}}/M_{\text{b}}^\star$	Bulge dynamical mass and stellar mass, classical bulge fraction [4.2.4]
$\sigma_x^{\text{b}}, \sigma_y^{\text{b}}, \sigma_z^{\text{b}}, \sigma_{\text{rms}}^{\text{b}}$	Half-mass bulge velocity dispersions in (x, y, z) and rms [4.2.3]
$\phi_{\text{bp}}, (b/a)_{\text{bp}}$	b/p-bulge orientation and axis ratio from top [4.2.1]
$h_{\text{bp}}, (c/a)_{\text{bp}}$	Central vertical scale height and edge-on axis ratio of b/p bulge [4.2.1]
x_X	Radius of maximum X [4.2.1]
$M_{\text{tlb}}, M_{\text{slb}}$	Stellar masses of thin and superthin long bar [4.3]
$\phi_{\text{lb}}, R_{\text{lb}}$	Long bar orientation and half length [4.3]
$h_{\text{tlb}}, h_{\text{slb}}$	Vertical scale heights of thin and superthin long bar [4.3]
Ω_b, R_{CR}	Bar pattern speed and corotation radius [4.4]
$M_\bullet, r_{\text{infl}}$	Mass and dynamical influence radius of supermassive black hole [3.4]
$M_{\text{NSC}}, M_{\text{NSD}}$	Masses of nuclear star cluster and nuclear stellar disk [4.1]
$r_{\text{NSC}}, (c/a)_{\text{NSC}}$	Nuclear star cluster half-mass radius and axis ratio [4.1]
$r_{\text{NSD}}, h_{\text{NSD}}$	Nuclear stellar disk break radius and vertical scale height [4.1]
M_{hot}	Coronal (hot) halo mass [6.2]
$M_{\text{s}}, M_{\text{sub}}$	Stellar halo mass and substructure mass [6.1.2]
$\alpha_{\text{in}}, \alpha_{\text{out}}, r_{\text{s}}$	Stellar halo inner, outer density slope, break radius [6.1.1]
$q_{\text{in}}, q_{\text{out}}$	Inner and outer mean flattening [6.1.1]
$\sigma_r^{\text{s}}, \sigma_\theta^{\text{s}}, \sigma_\phi^{\text{s}}$	Stellar halo velocity dispersions in r, θ, ϕ near the Sun [6.1.3]
\bar{v}_ϕ^{s}	Local halo rotation velocity [6.1.3]
$M^{\text{t}}, M^{\text{T}}$	Thin, thick disk stellar masses [5.1.3, 5.2.2]
$R^{\text{t}}, R^{\text{T}}$	Thin, thick disk exponential scale length in R [5.1.3, 5.2.2]
$z^{\text{t}}, z^{\text{T}}$	Thin, thick disk exponential scale height in z [5.1.3]
f_ρ, f_Σ	Thick disk fraction in local density, in integrated column density [5.1.3]
$\sigma_R^{\text{t}}, \sigma_z^{\text{t}}$	Old thin disk velocity dispersion in R, z at 10 Gyr [5.4]
$\sigma_R^{\text{T}}, \sigma_z^{\text{T}}$	Thick disk velocity dispersion in R, z [5.4]
$\Sigma_{\text{tot}}, \rho_{\text{tot}}, \epsilon_{\text{tot}}$	Local mass surface density, mass density, dark matter energy density [5.4.2]

^a f_{bary} is the ratio of baryonic mass to total mass integrated to a radius in which both quantities have been determined (e.g., r_{vir}).

Note: Our convention is to use R for a projected radius in two dimensions (e.g., disk) and r for a radius in three dimensions (e.g., halo). Numbers in brackets, [], point to relevant sections of this review.

Abbreviations: b/p, box/peanut; LSR, local standard of rest; rms, root mean square.

a plausible dynamical description of the Galaxy; this is an important aim for the next few years. For more scientific context, we recommend reviews from the past decade that consider major components of the Galaxy: Helmi (2008), Ivezić et al. (2012), Rix & Bovy (2013), and Rich (2013).

This is an era of extraordinary interest and investment in Galactic studies exemplified above all by the *Gaia* astrometric mission and many other space-based and ground-based surveys. In the next section (Section 2), we provide a context for these studies. The Galaxy is then described in terms of traditional components: Galactic Center (Section 3), Inner Galaxy (Section 4), Disk Components (Section 5), and Halo (Section 6). Finally, we discuss the likely developments in the near term and attempt to provide some pointers to the future (Section 7).

2. THE GALAXY IN CONTEXT

We glimpse the Galaxy at a moment in time when globally averaged star-formation rates (SFRs) are in decline and nuclear activity is low. In key respects, the Milky Way is typical of large galaxies today in low-density environments (Kormendy et al. 2010), especially with a view to global parameters (e.g., current SFR \dot{m}_* , baryon fraction f_{bary}) given its total stellar mass (cf. de Rossi et al. 2009), as we discuss below. But in other respects, it is relatively unusual, caught in transition between the “red sequence” of galaxies and the “blue cloud” (Mutch et al. 2011). Moreover, unlike M31, our Galaxy has not experienced a major merger for the past 10 Gyr, indicating a remarkably quiescent accretion history for a luminous galaxy (Stewart et al. 2008). Most L_* galaxies lie near the turnover of the galaxy luminosity function where star-formation quenching starts to become effective (Benson et al. 2003). But this may not be the last word for the Galaxy: The Magellanic gas stream is evidence for very substantial ($\sim 10^9 M_\odot$) and ongoing gas accretion in the present day (Putman et al. 1998, Fox et al. 2014). The Galaxy stands out in another respect: It is uncommon for an L_* galaxy to be orbited by two luminous dwarf galaxies that are both forming stars (Robotham et al. 2012). Nonetheless, the Galaxy will always be the most important benchmark for galaxy evolution because it provides information that few other galaxies can offer—the fully resolved constituents that make up an L_* galaxy in the present epoch.

2.1. Environment and Evolution

The Galaxy is one of the two dominant members of the Local Group, a low-mass system constituting a loosely bound collection of spirals and dwarf galaxies. The Local Group has an internal velocity dispersion of about 60 km s^{-1} (van den Bergh 1999) and is located in a low-density filament in the far outer reaches of the Virgo supercluster of galaxies (Tully et al. 2014). Galaxy groups with one or two dominant spirals are relatively common, but close analogues of the Local Group are rare. The presence of an infalling binary pair—the Small and Large Magellanic Clouds (SMC, LMC)—around an L_* galaxy is only seen in a few percent of cases in the Galaxy and Mass Assembly survey (Driver et al. 2011). This frequency drops to less than 1% if we add the qualification that the massive binary pair are actively forming stars.

With a view to past and future evolution, it is instructive to look at numerical simulations of the Local Group. The Constrained Local Universe Simulations—the CLUES project (<http://www.clues-project.org>)—are optimized for a study of the formation of the Local Group within a cosmological context (Forero-Romero et al. 2013, Yepes et al. 2014). The accretion history of the Local Group is relatively quiet, consistent with its cold internal dynamics. The largest simulations with the most advanced prescriptions for feedback (e.g., the Feedback in Realistic Environments or FIRE project, Hopkins et al. 2014) are providing new insight on why only a small fraction of the dark minihalos in orbit about the Galaxy are visible as dwarf galaxies (Wetzel et al. 2016). But we are still a long way from a detailed understanding of how the dark matter and baryons work together to produce present-day galaxies.

The future orbital evolution and merging of the Local Group has been considered by several groups (Cox & Loeb 2008, van der Marel et al. 2012a, Peebles & Tully 2013). These models are being successively refined as proper motions of stars in M31 become available. We learn that the Galaxy and M31 will reach pericenter passage in about 4 Gyr and finally merge in ~ 6 Gyr. The models serve to remind us that the Galaxy is undergoing at least three strong interactions (LMC, SMC, Sgr) and therefore cannot be in strict dynamical equilibrium. This evolution can be accommodated in terms of structural and kinematic parameters (adiabatic invariants) that are slowly evolving at present (Binney 2013).

2.2. Galaxy Classification and Integrated Properties

For most of the past century, galaxy studies made use of morphological classification to separate them into different classes. But high-quality, multiband photometric and spectroscopic surveys have provided us with a different perspective (Blanton & Moustakas 2009). The bulge-to-disk ratio, e.g., from Sérsic index fitting to photometric images, continues to play an important role in contemporary studies (Driver et al. 2011). Many observed properties correlate with the total stellar mass M_* and the global SFR \dot{m}_* . Galaxies fall into a “red sequence” where star formation has been largely quenched, and a “blue cloud” (main sequence) where objects are actively forming stars, with an intervening “green valley.” Mutch et al. (2011) first established that the Galaxy today appears to fall in the green valley, much like M31, interestingly. Their method is based on the Copernican principle that the Galaxy is unlikely to be extraordinary given global estimates for M_* and \dot{m}_* . In large galaxy samples, these quantities are expected to correlate closely with photometric properties like absolute magnitude and color index with a scatter of about 0.2 dex. In **Figure 3**, we show the results of the most recent analysis of this kind (Licquia et al. 2015).

Flynn et al. (2006) recapitulate the long history in deriving Galaxy global properties. Chomiuk & Povich (2011) present an exhaustive study across many wave bands and techniques to arrive at a global SFR \dot{m}_* for the Galaxy. They attempt to unify the choice of initial mass function (IMF) and stellar population synthesis model across methods, and find $\dot{m}_* \approx 1.9 M_\odot \text{ year}^{-1}$, which is within range of the widely quoted value of $1\text{--}3 M_\odot \text{ year}^{-1}$ by McKee & Williams (1997). Licquia & Newman (2015) revisit this work and conclude that $\dot{m}_* = 1.65 \pm 0.19 M_\odot \text{ year}^{-1}$ for an adopted Kroupa IMF. Likewise, there are many estimates of the Galaxy’s total stellar mass, most from direct integration of starlight and an estimate of the total stellar mass-to-light ratio, Υ^* , from which they estimate the total stellar mass to be $6 \pm 1 \times 10^{10} M_\odot$ for a Galactocentric distance of $R_0 \approx 8.3$ kpc. In Section 6.4, we estimate a total stellar mass of $5 \pm 1 \times 10^{10} M_\odot$ and a revised R_0 from combining estimates of the mass of the bulge and the disk from dynamical model fitting to stellar surveys and to the Galactic rotation curve.

To transform these quantities into the magnitude system, one method is to select a large set of disk galaxies from the Sloan Digital Sky Survey (SDSS) photometric survey with measured bolometric properties over a spread in inclination and internal extinction. Licquia et al. (2015) select possible analogues that match M_* and \dot{m}_* in the Galaxy given the uncertainties. In **Figure 3a**, we present the total absolute magnitudes and unbiased galaxy colors for the analogues using the SDSS *ugriz* bands; most appear to fall in the green valley, in agreement with Mutch et al. (2011). Given these data, the likely values for the Galaxy are presented in **Table 2** without the uncertainties. Note the lack of consistency between the quoted SDSS magnitudes and colors because they are derived using different calibration methods as recommended for SDSS DR8 (Aihara et al. 2011), but the differences are mostly below the statistical errors quoted by Licquia et al. (2015). In **Figure 3b**, the analogues show a lot of scatter when transformed to color-magnitude space in which the green valley is less well defined. Although the Galaxy’s location has moved, it still resides in the green valley.

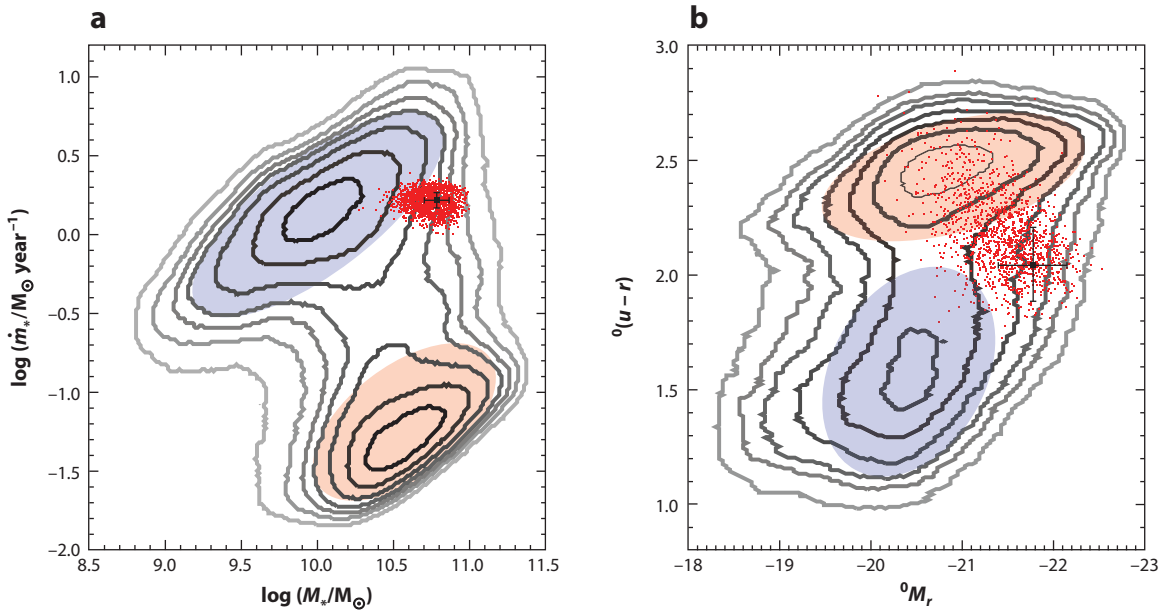


Figure 3

(a) Sample of 3,500 Milky Way analogues (*red dots*) drawn from the Sloan Digital Sky Survey with the same stellar mass M_* and star-formation rate \dot{m}_* , given the measurement uncertainties. The Galaxy, indicated by a cross, resides in the “green valley” just below the “blue cloud” (see also Mutch et al. 2011). (b) When mapped to absolute magnitude–color space, the Milky Way analogues are dispersed over a wider region extending into the red sequence. The error bar is noticeably offset from the center of the distribution due to corrections for inclination reddening and Eddington bias. The increased scatter compared to panel *a* is a consequence of the broad range of $g-r$ colors that can correspond to a specific star-formation rate. The magnitude and color superscript “0” indicates that the results are corrected to $z = 0$. In both figures, the contours indicate the density of galaxies in the projected plane. Adapted from Licquia et al. (2015) with permission.

The same inconsistency is seen in the Johnson magnitudes (Table 2), which are derived via color transformations from the SDSS magnitudes (Blanton & Roweis 2007). The `cmodel` and `model` magnitudes in *ugriz* bands are converted to an equivalent set of *U B V R I* magnitudes and color indices, respectively (see http://www.sdss.org/dr12/algorithms/magnitudes/#mag_model). This results in small differences between the color derived from single-band absolute magnitudes as opposed to the color inferred from the best SDSS color measurement, but these differences mostly fall below the uncertainties.

For either the SDSS or the Johnson magnitudes, there are no earlier works that cover the five bands; most studies concentrate on *B* and *V* (de Vaucouleurs & Pence 1978, Bahcall & Soneira 1980). De Vaucouleurs (1983), updating his earlier work, derived $M_B = -20.2 \pm 0.15$ assuming a distance of $R_0 = 8.5 \pm 0.5$ kpc and a color term $B - V = 0.53 \pm 0.04$, similar to values derived by Bahcall & Soneira (1980): $M_B = -20.1$, $M_V = -20.5$, and $B - V = 0.45$. Van der Kruit (1986) took the novel approach of using observations from the *Pioneer* probes en route to Jupiter and beyond to measure optical light from the Galaxy and found $M_B = -20.3 \pm 0.2$ and $B - V = 0.83 \pm 0.15$. These values are mostly dimmer and bluer than the modern values in Table 2. The latter find strong support with the dynamically determined *I*-band values ($M_I = -22.4$, $\Upsilon_I^* = 1.4$) from Piffl et al. (2014a) and ($M_I = -22.5$, $\Upsilon_I^* = 1.3$) from Bovy & Rix (2013), and are in close agreement with Flynn et al. (2006).

$M_{\Delta\lambda}$: Galaxy absolute magnitude

$M_{\Delta\lambda_1} - M_{\Delta\lambda_2}$: Galaxy color index

$\Upsilon_{\Delta\lambda}^*$: Galaxy mass-to-light ratio

\dot{m}_* : Galaxy total star-formation rate; $1.65 \pm 0.19 \text{ M}_\odot \text{ year}^{-1}$

Table 2 Global magnitudes, color indices, and mass-to-light ratios for the Galaxy

Absolute magnitude, ^a $M_{\Delta\lambda}$	u −19.87 U −20.67	g −21.00 B −20.70	r −21.64 V −21.37	i −21.87 R −21.90	z −22.15 I −22.47
Color index, ^b ($M_{\Delta\lambda_1} - M_{\Delta\lambda_2}$)	$u - r$ 1.96 $U - V$ 0.86	$u - g$ 1.29 $U - B$ 0.14	$g - r$ 0.65 $B - V$ 0.73	$r - i$ 0.28 $V - R$ 0.54	$i - z$ 0.28 $R - I$ 0.58
Mass-to-light ratio, Υ^*	u 1.61 U 1.66	g 1.77 B 1.73	r 1.50 V 1.70	i 1.34 R 1.45	z 1.05 I 1.18

^aThe Sloan Digital Sky Survey (SDSS) and Johnson photometry are calibrated (typical errors ~ 0.1 mag) with respect to the AB and Vega magnitude systems, respectively.

^bDifferent calibration schemes are needed for the SDSS total magnitudes and the unbiased galaxy colors, which leads to inconsistencies between magnitude differences and color indices (courtesy of Licquia et al. 2015).

Note: Magnitudes and colors derived for the Galaxy from Milky Way analogues drawn from the SDSS using the Kroupa initial mass function. All values assume $R_0 = 8.2$ kpc and $R_d = 2.6$ kpc for the Galaxy.

It is clear from **Figure 3** that the Milky Way is a very luminous, reddish galaxy, somewhat at odds with its traditional classification as an Sb–Sbc galaxy. This has raised questions in the past about where it falls on the Tully–Fisher relation (e.g., Malhotra et al. 1996, Hammer et al. 2012). But this high luminosity is consistent with its high circular velocity (~ 240 km s^{−1}) discussed in Section 6.4. In **Table 2**, the Galaxy is slightly fainter in *ugriz* absolute magnitude and slightly less massive in both stellar and baryonic mass than the average for its rotation speed. When considering both the current uncertainties in Milky Way properties and the scatter of galaxies about the relation, the Galaxy is consistent with the Tully–Fisher relation to better than 1σ uncertainty. The Milky Way appears to be a kinematically typical spiral galaxy for its intrinsic luminosity.

3. GALACTIC CENTER

3.1. Location

The Galactic Center (GC), as we understand it today, was first identified through the discovery of Sgr A by radio astronomers (Piddington & Minnett 1951). Based on its unique radio emission properties and its precise coincidence with the dynamical center of the rotating inner H I disk (Oort & Rougoor 1960), the IAU officially adopted Sgr A as the center of the Galaxy, making its position the zero of longitude and latitude in a new system of Galactic coordinates (Blaauw et al. 1959). Later Balick & Brown (1974) discovered the unresolved source Sgr A^{*}, now known to be at the location of the Milky Way’s supermassive black hole (SMBH), at $(l_c, b_c) = (-0.056^\circ, -0.046^\circ)$ (Reid & Brunthaler 2004).

Thirty years ago, Kerr & Lynden-Bell (1986, p. 1024) gave this working definition of the GC:

Currently it is assumed that the Galactic Center coincides sufficiently well with the Galaxy’s barycenter that a distinction between the point of greatest star density (or any other central singularity) and the barycenter (center of mass) is not necessary. It is also assumed that to sufficient accuracy for the internal dynamics of the Galaxy, the Galactic Center defines an inertial coordinate system. These assumptions could prove to be untrue if for instance the center of the distribution of the mysterious mass in the heavy halo were displaced from the mass center of the visible Galaxy.

Galactic Center:

location of radio source Sgr A^{*}; its Galactic coordinates (l_c, b_c) are $(-0.056^\circ, -0.046^\circ)$

SMBH: supermassive black hole of the Milky Way

Indeed, in a hierarchical universe the first assumption is almost certainly violated beyond tens of kiloparsecs: We discuss in Section 6 that the Galaxy continues to accrete satellite galaxies carrying both stars and dark matter; furthermore, the Milky Way’s dark matter halo interacts both with infalling dark matter and with other halos in the Local Group. However, as discussed below, the inner Milky Way appears to have “settled down” to a well-defined and well-centered midplane; thus we may assume that the region of greatest star density coincides with the barycenter of the mass within the Solar Circle.

The second part of the definition may ultimately also come into question. Numerical simulations reveal that dark matter halos tumble at the level of a few radians per Hubble time. The baryonic components are largely bound to the dark matter but may slosh around within them. Furthermore, the spin axis of the Galactic Plane is likely to precess with respect to a celestial coordinate frame defined by distant quasars or radio sources. Over the lifetime of the *Gaia* mission, this precession ($\sim 30 \mu\text{as year}^{-1}$) should be detectable (Perryman et al. 2014).

3.2. Distance

The distance of the Sun to the GC, R_0 , is one of the fundamental scaling parameters for the Galaxy. All distances determined from angular sizes or from radial velocities and a rotation model are proportional to R_0 . Also the sizes, luminosities, and masses of objects such as molecular clouds scale with R_0 , as do most estimates of global Galactic luminosity and mass. Because R_0 is one of the key parameters, we consider its measured value in some detail here. Previous reviews on this subject have been written by Kerr & Lynden-Bell (1986), Reid (1993), Genzel et al. (2010), and Gillessen et al. (2013), and a recent compilation of results is given by Malkin (2013).

Similar to their discussions, we divide methods of determining R_0 into direct (primary), model-based, and secondary ones. Direct methods compare an angular dimension or velocity near the GC with a physical length scale or radial velocity (RV), with minimal modeling assumptions and without having to use additional calibrations. Model-based methods determine R_0 as one of the model parameters through a global fit to a set of data. Secondary methods finally use standard candle tracers whose distances are based on secondary calibrations such as period-stellar luminosity relations, and whose distributions are known or assumed to be symmetric with respect to the GC. In the following, we briefly review the different methods. **Table 3** gives the list of independent recent determinations of R_0 , which we use for obtaining an overall best estimate below.

3.2.1. Direct estimates. As discussed more fully in Sections 3.4 and 6.4, the SMBH is believed to be at rest at the dynamical center of the Milky Way (Reid & Brunthaler 2004, Reid 2008). Thus R_0 can be determined by measuring the distance to the SMBH’s radiative counterpart, Sgr A*. At ~ 8 kpc distance, the expected parallax of Sgr A* is $\sim 100 \mu\text{as}$. This would be resolvable with very long baseline interferometry (VLBI), but unfortunately the image of Sgr A* is broadened by interstellar scattering (e.g., Bower et al. 2004). However, Reid et al. (2009b) measured trigonometric parallaxes of H_2O masers in Sgr B2, a molecular cloud complex that they estimated is located ~ 130 pc in front of Sgr A*.

A second direct estimate of the distance to the SMBH comes from monitoring proper motions (PMs) and line-of-sight (LOS) velocities for stellar orbits near Sgr A* (Eisenhauer et al. 2003, Ghez et al. 2008, Gillessen et al. 2009b, Morris et al. 2012), in particular, for that of star S2, which has by now been followed for a complete orbit around the dynamical center. The main systematic uncertainties are source confusion, tying the SMBH to the astrometric reference frame, and the potential model; relativistic orbit corrections lead to an increase in the value of R_0 by ~ 0.1 kpc (Genzel et al. 2010). See also Gillessen et al. (2009a), who combined the existing two major data sets in a joint analysis.

Table 3 Recent measurements of distance R_0 to the Galactic Center

Label	Reference	Method	Location	T	R_0 (kpc)
Rd+09	Reid et al. (2009b)	Trig. parallax of Sgr B	GC	d	7.90 ± 0.75
Mo+12	Morris et al. (2012)	Orbit of S0-2 around Sgr A*	GC	d	7.70 ± 0.40
Gi+09	Gillessen et al. (2009b)	Stellar orbits around Sgr A*	GC	d	8.33 ± 0.35
Ch+15	Chatzopoulos et al. (2015)	NSC statistical parallax	GC	d	8.27 ± 0.13
Do+13	Do et al. (2013)	NSC statistical parallax	GC	d	8.92 ± 0.56
BB15	Bajkova & Bobylev (2015)	Trig. parallaxes of HMSFRs	DSN	m	8.03 ± 0.32
Rd+14	Reid et al. (2014)	Trig. parallaxes of HMSFRs	DSN	m	8.34 ± 0.19
Ho+12	Honma et al. (2012)	Trig. parallaxes of HMSFRs	DSN	m	8.05 ± 0.45
ZS13	Zhu & Shen (2013)	Near- R_0 rotation young tracers	DSN	m	8.08 ± 0.62
Bo13	Bobylev (2013)	Near- R_0 rotation SFR+Cepheids	DSN	m	7.45 ± 0.66
Sch12	Schönrich (2012)	Near- R_0 rotation SEGUE stars	DSN	m	8.27 ± 0.41
Ku+15	Küpper et al. (2015)	Tidal tails of Pal-5	IH	m	8.30 ± 0.35
VH+09	Vanhollebeke et al. (2009)	Bulge stellar population model	B	m	8.70 ± 0.50
Pi+15	Pietrukowicz et al. (2015)	Bulge RR Lyrae stars	B	s	8.27 ± 0.40
De+13	Dékány et al. (2013)	Bulge RR Lyrae stars	B	s	8.33 ± 0.15
Da09	Dambis (2009)	Disk/halo RR Lyrae stars	DSN	s	7.58 ± 0.57
Ma+13	Matsunaga et al. (2013)	Nuclear bulge T-II Cepheids	B	s	7.50 ± 0.60
Ma+11	Matsunaga et al. (2011)	Nuclear bulge Cepheids	B	s	7.90 ± 0.36
Gr+08	Groenewegen et al. (2008)	Bulge Cepheids	B	s	7.98 ± 0.51
Ma+09	Matsunaga et al. (2009)	Bulge Mirae	B	s	8.24 ± 0.43
GrB05	Groenewegen & Blommaert (2005)	Bulge Mirae	B	s	8.60 ± 0.81
FA14	Francis & Anderson (2014)	Bulge red clump giants	B	s	7.50 ± 0.30
Ca+13	Cao et al. (2013)	Bulge red clump giants	B	s	8.20 ± 0.20
Fr+11	Fritz et al. (2011)	NSC red clump giants	GC	s	7.94 ± 0.76
FA14	Francis & Anderson (2014)	All globular clusters	B, IH	s	7.40 ± 0.28
Bi+06	Bica et al. (2006)	Halo globular clusters	IH	s	7.10 ± 0.54

Note: Recent determinations of the distance to the GC, R_0 , used for weighted averages and in **Figure 4**. Labels given in column 1 are used in **Figure 4**. The listed uncertainties include statistical and systematic errors, added in quadrature when both are published. Where a systematic error is not quoted by the authors or included in their total published error, we estimated it from results obtained by them under different assumptions, when possible (GrB05, Fr+11, BB15, Rd+14, Bo13, Bi+06). For Ca+13, no error was given; we estimated one from the metallicity dependence of the red clump giant calibration by Nataf et al. (2013). In the remaining cases (ZS13, Sch12, Kue+15, Da09), we took the systematic error to be equal to the statistical error. Abbreviations: (Column 3) HMSFR, high-mass star-formation region; NSC, nuclear star cluster; SFR, star-formation region. (Column 4) B, bulge; DSN, disk and Solar Neighborhood; GC, Galactic Center; IH, inner halo. (Column 5) T, type of measurement; d, direct; m, model-based; s, secondary.

The statistical parallax of the nuclear star cluster (NSC) obtained by comparing stellar PMs and LOS velocities has been used as a third direct estimate of R_0 (Genzel et al. 2000, Trippe et al. 2008, Do et al. 2013). This method has now become accurate enough that projection and finite field-of-view effects in combination with orbital anisotropies need to be modeled (Chatzopoulos et al. 2015).

3.2.2. Model-based estimates. VLBI astrometry has provided accurate parallaxes and PMs for over 100 OH, SiO, and methanol masers in high-mass star-formation regions (HMSFRs) in the Galactic disk (Honma et al. 2007, 2012; Reid et al. 2009a, 2014; Sato et al. 2010). Most of these sources are located in the Galactic spiral arms. By fitting a spiral arm model together with a model

for Galactic circular rotation to the positions and velocities of the HMSFRs, precise estimates of R_0 can be obtained together with rotation curve and other parameters (for a different analysis, see Bajkova & Bobylev 2015). Because distances are determined geometrically, no assumptions on tracer luminosities or extinction are necessary. The main remaining systematic uncertainties thus are the assumption of axisymmetric rotation, the detailed parameterization of the rotation curve model, and the treatment of outliers.

Another long-standing approach is based on analyzing the velocity field near the Solar Circle, using PMs and LOS velocities of various tracers. These methods assume an axisymmetric velocity field and, in some cases, include the perturbing effects of a spiral arm model. In the traditional form, the data are used to solve for the Oort constants A, B (Section 6.4) from the PMs and for $2AR_0$ from the RVs, to finally estimate R_0 (Mihalas & Binney 1981, Zhu & Shen 2013). Another variation is to use young stars or SFRs assumed to follow circular orbits precisely (Sofue et al. 2011, Bobylev 2013). An analysis less sensitive to the uncertain perturbations from spiral arms and other substructure is that by Schönrich (2012), who uses a large number of stars with PMs and RVs from the Sloan Extension for Galactic Understanding and Exploration (SEGUE) survey (Yanny et al. 2009) to determine R_0 by combining the rotation signals in the radial and azimuthal velocities for stars within several kiloparsecs from the Sun.

A promising new method is based on the detailed dynamical modeling of halo streams. Although stream modeling has mostly been used to obtain estimates for the mass and shape of the dark matter halo (see Section 6.3), Küpper et al. (2015) showed that with accurate modeling R_0 can also be well constrained as part of a multiparameter fit to detailed density and LOS velocity measurements along the stream.

Vanhollebeke et al. (2009) compared predictions from a stellar population model for the Galactic bulge and intervening disk with the observed star counts. They used a density model based on near-IR (NIR) data from Binney et al. (1997) and varied the star-formation history and metallicity distribution of bulge stars. The value of R_0 from their best-fitting models depends heavily on the magnitudes of red clump stars, showing a close connection to secondary methods.

3.2.3. Secondary estimates. There is a long history of secondary R_0 measurements based on the distance distributions of RR Lyrae stars, Cepheids, Mira stars, red clump giants (RCGs), and globular clusters (Reid 1993). Individual distances are derived from external calibrations of period-luminosity (PL) relations for the variable stars and from horizontal branch (HB) magnitudes for RCGs and globular clusters. The main systematic errors in these methods come from uncertainties in the calibrations but also from the extinction corrections and reddening law and from how the distance distribution in the survey volume is related to the center of the Galaxy.

RR Lyrae stars, pulsationally unstable HB stars with characteristic absolute magnitudes $M_I = 0.2$, $M_K = -0.5$ (Catelan et al. 2004), are the primary distance tracers for old, metal-poor populations. Large numbers of RR Lyrae stars, identified by the Optical Gravitational Lensing Experiment (OGLE, Udalski et al. 2008) and Vista Variables in the Via Lactea (VVV, Minniti et al. 2010) surveys, were recently used to map out the old metal-poor population in the bulge (Pietrukowicz et al. 2015 and Dékány et al. 2013, respectively). Individual distances are more accurate by a factor of ~ 2 in the NIR than in optical data, owing to higher precision and reduced metallicity dependence in the PL relation and less sensitivity to reddening. With the large bulge samples the centroid of the distribution can be determined more accurately than it was in earlier work (e.g., Groenewegen et al. 2008, Majaess 2010). On larger Galactic scales, Dambis (2009) calibrated thick disk and halo RR Lyrae populations separately by statistical parallax to then estimate R_0 .

Type II Cepheids trace old, typically metal-poor populations; they are brighter than RR Lyrae stars but much less numerous. Groenewegen et al. (2008) used NIR data for 39 population II Cepheids in the bulge from the OGLE survey; a related work is by Majaess (2010). Matsunaga et al. (2011, 2013) analyzed 3 classical Cepheids and 16 type II Cepheids from an NIR survey of the inner ~ 30 pc in the nuclear bulge.

Groenewegen & Blommaert (2005) obtained a PL relation for 2,691 Mira long-period variables in the OGLE bulge fields, whereas Matsunaga et al. (2009) studied 100 Miras in the nuclear bulge. For these pulsating RGB stars the extinction corrections are smaller, but calibrations from the LMC and globular clusters were needed to estimate R_0 from these data.

Since the work by Paczynski & Stanek (1998), RCGs have been recognized as important distance probes in the Galaxy (see Girardi 2016, in this volume). RCGs are He-core-burning stars with a narrow range of luminosities, especially in medium-to-old-age populations such as that in the Galactic bulge. Typical absolute magnitudes are $M_I = -0.5$, $M_K = -1.6$, with a dispersion of ~ 0.1 – 0.2 mag, and systematic effects due to age and metallicity variations are relatively small and fairly well understood. Surveys toward the inner Galaxy are frequently done in the NIR to minimize extinction (Babusiaux & Gilmore 2005, Nishiyama et al. 2006) or in the I band (Paczynski & Stanek 1998, Nataf et al. 2013). The K -band studies tend to give slightly shorter distances. Fritz et al. (2011) used RCGs in several NIR bands to determine a distance to the central NSC.

The centroid of the distance distribution of globular clusters, the basis for the famous early work by Shapley (1918), continues to be used for estimating R_0 (Bica et al. 2006, Francis & Anderson 2014). These studies are based on the catalog of Harris (2010, and earlier), where individual distances are estimated from HB magnitudes and reddening. The distance distribution of the clusters is somewhat asymmetric, and R_0 values found are on the low side of the distribution in **Table 3**. Systematic effects could be due to missing clusters behind the GC or to errors in the HB magnitudes, e.g., from extinction uncertainties or stellar confusion in crowded cluster fields (Genzel et al. 2010). However, the method provides a rare opportunity to estimate R_0 from Galactic halo tracers.

3.2.4. Overall best estimate and discussion. **Table 3** gives the list of recent determinations that we use for obtaining an overall best estimate for R_0 . For each method, we kept at most three determinations to prevent overweighting often-employed techniques with similar systematic uncertainties; for example, there are many determinations of R_0 using RCGs as standard candles. We omitted determinations that were later updated by the same group of authors based on improved data but kept independent reanalyses of published data by other authors. We also did not include R_0 estimates that used priors based on measured values already taken into account (e.g., McMillan 2011).

Figure 4 shows the overall distribution of these 26 measurements with time and the separate distributions for tracers in the GC, bulge, disk, and halo, respectively. To obtain a best estimate for R_0 , we consider weighted means for the total and various subsamples. For any N_m measurements, we compute (a) the standard error of the weighted mean (SE) and (b) the unbiased standard error of the weighted mean (UE, square root of $1/N_m$ times the unbiased weighted sample variance), and following Reid (1993), (c) we consider possible correlations between some of the measurements. These can arise, e.g., because HB or PL calibrations use very similar theoretical models or calibrators or are based on a common LMC distance; because two data sets, although independent, can only be obtained for the same small number of stars; or because several measurements are all based on the assumption that the velocity field near the Solar Circle is axisymmetric. Clearly, some of these correlations have stronger influence than others. For a conservative error evaluation,

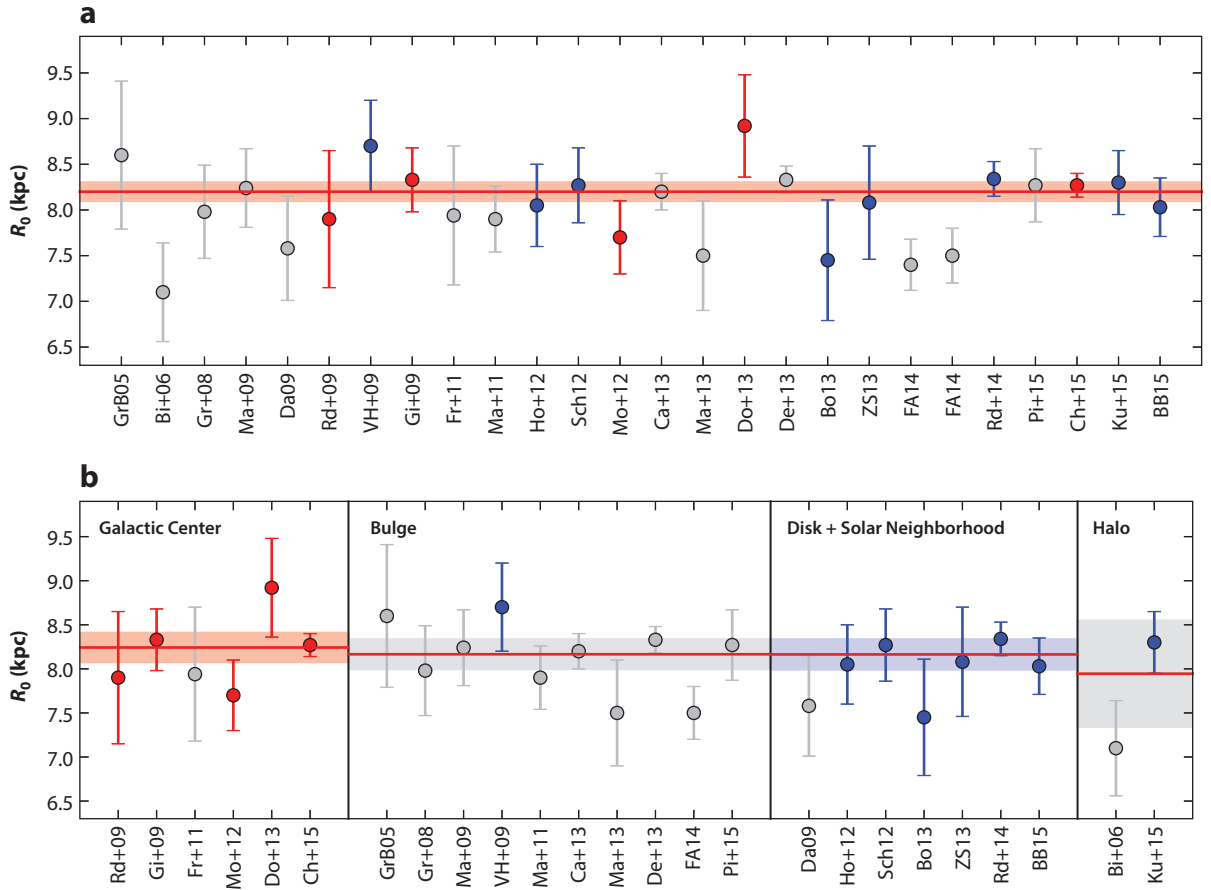


Figure 4

Recent measurements of R_0 from **Table 3**, using different methods. Red, blue, and gray points denote direct, model-based, and secondary estimates, respectively. (a) Time sequence for all, with our adopted best estimate, $R_0 = 8.2 \pm 0.1$ kpc. (b) Separate time sequences for determinations in the Galactic Center, bulge, disk and Solar Neighborhood, and inner halo (not using the FA14 globular cluster value that includes the inner metal-rich clusters). The horizontal lines show weighted mean values for the respective components, and colored bands show 1σ UUE (uncorrelated unbiased standard errors).

we retain $N_{\text{uc}} = 11$ independent measurements for the total sample, and $N_{\text{uc}} = (4, 4, 3, 2)$ for the separate (GC, bulge, disk and Solar Neighborhood, inner halo, respectively) tracer samples. We note that the sets of methods kept for the different regions are largely independent. In each case, we determine an uncorrelated sample error (UUE) by replacing N_m in UE with N_{uc} .

Using the notation $R_0 \pm \text{UUE}$ [UE, SE], we find $R_0 = 8.14 \pm 0.10$ [0.07, 0.06] kpc for the total sample; $R_0 = 8.17 \pm 0.12$ [0.09, 0.07] kpc for measurements made in 2013 or later; $R_0 = 8.29 \pm 0.03$ [0.03, 0.08] kpc for the 4 measurements with errors ≤ 0.2 kpc (Ch+15, Rd+14, De+13, Ca+13); $R_0 = 8.22 \pm 0.07$ [0.07, 0.07] kpc for the 11 uncorrelated best determinations; $R_0 = 8.21 \pm 0.08$ [0.05, 0.06] kpc excluding the 2 values outside their (2σ) of the overall weighted mean; and $R_0 = 8.19 \pm 0.08$ [0.06, 0.06] kpc for all values excluding halo. All data samples give very consistent results; the fact that SE and UE generally agree within $\sim 20\%$ suggests that the errors given for the individual R_0 measurements are mostly realistic. Based on the scatter and

UUEs of the various sample means, we adopt here our best estimate for the distance to the GC: $R_0 = 8.2 \pm 0.1$ kpc. This value is significantly lower than the IAU standard ($R_0 = 8.5$ kpc).

The weighted sample means for tracers in the different regions of the Galaxy are $R_0 = 8.24 \pm 0.16$ [0.13, 0.11] kpc for the GC sample, $R_0 = 8.17 \pm 0.17$ [0.11, 0.09] kpc for the bulge sample, $R_0 = 8.16 \pm 0.17$ [0.11, 0.13] kpc for the disk and Solar Neighborhood sample, and $R_0 = 7.95 \pm 0.60$ [0.60, 0.29] kpc for the inner halo sample. The fact that tracers in the GC, bulge, and disk result in similar estimates for R_0 within small errors (also for UUE with largely independent respective methods) suggests that the different Galactic components are well centered and, thus, that relative sloshing motions between these components must currently be unimportant. Together with the good alignment of the Milky Way bar and H I disk with the Galactic Plane (Section 3.3), this suggests that the inner Milky Way has settled to a well-determined equilibrium state. Even the inner halo tracers on scales of 10–20 kpc are consistent with having the same GC as the bulge and disk, within ~ 0.6 kpc error.

We anticipate significant improvements in many of these distance measurements based on data from the *Gaia* satellite, which will provide accurate parallaxes and proper motions for large numbers of Milky Way stars. These data will greatly improve our dynamical understanding of the Galactic disk, but also of the bulge and bar outside highly extincted regions, and lead to much-improved secondary calibrations, e.g., for RR Lyrae stars and RCGs. The direct estimate of R_0 from stellar orbits around Sgr A* is expected to improve steadily as the time base line increases and more orbits can be reliably constrained, especially with accurate astrometric and spectroscopic monitoring of the next close pericenter passage (2018 for the star S2).

R_0 : Sun's distance from the Galactic Center, 8.2 ± 0.1 kpc
 z_0 : solar offset from local disk midplane, 25 ± 5 pc

3.3. Solar Offset and Galactic Plane

Early estimates of the Sun's vertical position with respect to the Galactic Plane date back to van Tulder's (1942) analysis of stellar catalogs, from which was determined $z_0 = 14 \pm 2$ pc toward the North Galactic Pole. In support of the early value, Conti & Vacca (1990) obtained $z_0 = 15 \pm 3$ pc using 150 Wolf-Rayet stars within 20 kpc of the Sun. *Pioneer 10* observations of the optical background light in the Galaxy indicated $z_0 = 13 \pm 3$ pc (Toller 1990), and modeling the *Cosmic Background Explorer* (COBE) NIR surface brightness distribution resulted in $z_0 = 14 \pm 4$ pc (Binney et al. 1997, Drimmel & Spergel 2001).

But more expansive studies of the nearby disk show that these are underestimates. Chen et al. (2001) demonstrated the importance of correctly treating the larger-scale parameters of the disk population in such studies, using the SDSS photometric survey. Although the radial scale length is relatively unimportant, a vertically extended population with a well-established scale height is critical. The following estimates are based on either OB stars, open clusters, or optical star counts for a range of stellar populations, and they are broadly consistent: $z_0 = 24 \pm 3$ pc (Stothers & Frogel 1974), $z_0 = 28 \pm 5$ pc (Pandey et al. 1988), $z_0 = 21 \pm 4$ pc (Humphreys & Larsen 1995), $z_0 = 27 \pm 3$ pc (Mendez & van Altena 1998), $z_0 = 28 \pm 6$ pc (Chen et al. 1999), $z_0 = 27 \pm 4$ pc (Chen et al. 2001), and $z_0 = 24 \pm 2$ pc (Maíz-Apellániz 2001). Although the last estimate from *Hipparcos* OB stars has the smallest error, the distribution of young stars may be more sensitive to various perturbations, as illustrated by Gould's belt. Therefore we adopt here the best estimate from the complete SDSS photometric survey, i.e., $z_0 = 25 \pm 5$ pc (Jurić et al. 2008), which captures all these values.

The Galactic midplane was defined based on the very flat distribution of H I gas in the inner Galaxy, with an estimated uncertainty in the position of the Galactic pole of $\sim 0.1^\circ$ (Blaauw et al. 1960). Because the Sun was found to lie in the H I principal plane within the errors, and the measured offset relative to Population I stars was not considered reliable, the $b = 0$ plane was defined to pass through the Sun and Sgr A (not Sgr A*). Because we know now that $z_0 \simeq 25$ pc,

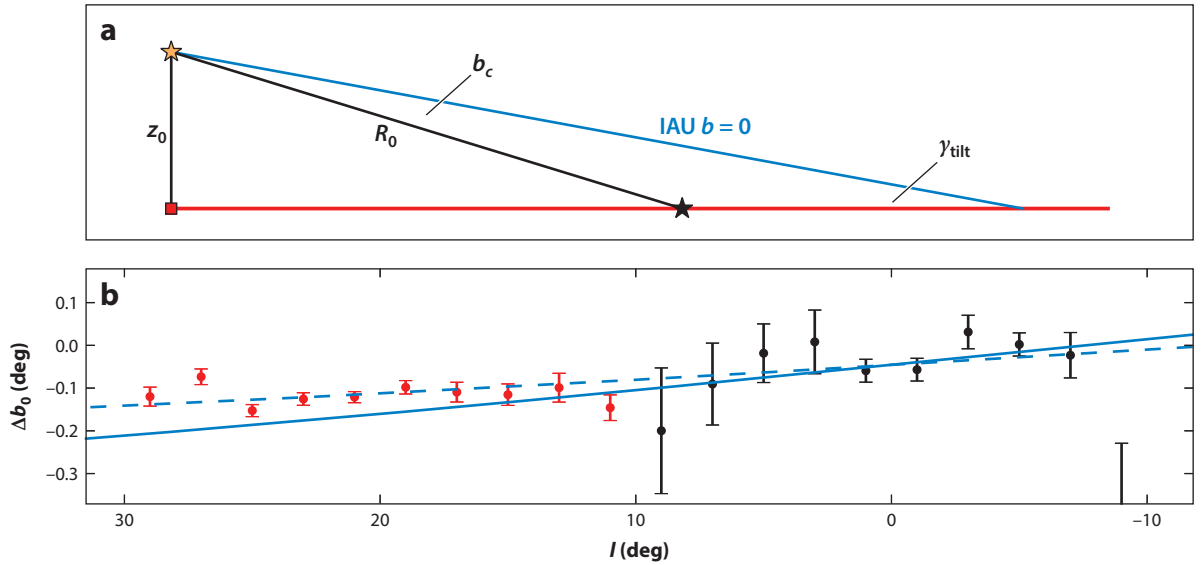


Figure 5

(a) Illustration of the tilt of the true Galactic disk plane (red) versus the $b=0$ plane (blue), as predicted from solar offset z_0 and assuming that the true plane passes through Sgr A* (black star). After Goodman et al. (2014). (b) Measured offsets Δb_0 of bulge (black) and long bar (red) peak star counts from the $b=0$ plane. The full line shows the predicted offsets for a 1D bar with bar angle of 27° (Section 4), lying precisely in the true Galactic Plane defined by $z_0 = 25$ pc, $R_0 = 8.2$ kpc, and $b_c = -0.046^\circ$, so that $\gamma_{\text{tilt}} = 0.13^\circ$. The dashed line is obtained when assuming an additional rotation of the true plane around the Sun–Galactic Center line by 0.14° . Deviations from the plane in the long-bar region are less than $\sim 0.05^\circ \simeq 5$ pc, of order 0.1% of the length of the long bar. Adapted from Wegg et al. (2015) with permission. Abbreviation: IAU, International Astronomical Union.

the true Galactic Plane is likely to be slightly inclined relative to the plane $b=0$. If it is assumed that Sgr A* lies precisely in the Galactic Plane (see Section 3.4), the required inclination angle is $\simeq 0.13^\circ$ (see **Figure 5** and Goodman et al. 2014). Objects located in the Galactic Plane between the Sun and the GC then appear at slightly negative latitudes. NIR star counts in the inner Galaxy have enough signal-to-noise to detect such offsets. The mean latitude of the peak of RCG counts in the Galactic long bar (see Section 4.3) is indeed found at $b \simeq -0.12^\circ$, corresponding to an offset of 14 pc at ~ 6 kpc distance (Wegg et al. 2015). The observed peak latitudes agree with those predicted for the inclined plane to within ~ 5 pc or $\sim 0.1\%$ of the half-length of the bar (**Figure 5**). The Galactic long bar is thus consistent with lying in a tilted midplane passing through Sgr A* and the point $z_0 = 25$ pc below the Sun to within $\sim 0.1\%$. Both stars and HI gas suggest that the Galactic disk inside the Solar Circle is very nearly flat.

3.4. Black Hole and Solar Angular Velocity

Measurements in the Milky Way have provided the best evidence for a central SMBH to date; see Reid (2009) and Genzel et al. (2010) for recent reviews. IR studies of the motions of gas clouds in the Sgr A region first indicated a central point mass of several $10^6 M_\odot$ (e.g., Lacy et al. 1980). Later, PM measurements of stars in the dense NSC showed evidence for a Keplerian increase of the stellar velocity dispersion to several 100 km s^{-1} at ~ 0.01 pc from the GC, corresponding to a central mass of $\sim 2\text{--}3 \times 10^6 M_\odot$ (Eckart & Genzel 1997, Ghez et al. 1998). Currently, from accurate LOS velocities and astrometric measurements with adaptive optics, stellar orbits have

been determined for some 30 of the so-called S stars in the central arcsecond, including one complete 15.8-year orbit for the star S2. All orbits are well fitted by a common enclosed mass and elliptical orbit focal point. From multiorbit fits, rescaled to $R_0 = 8.2$ kpc, the total enclosed mass is $M_\bullet = 4.3 \times 10^6 M_\odot$ (Ghez et al. 2008) and $M_\bullet = 4.2 \times 10^6 M_\odot$ (Gillessen et al. 2009b), and $M_\bullet = (4.20 \pm 0.36) \times 10^6 M_\odot$ from a joint analysis of the combined Very Large Telescope (VLT) and Keck data (Gillessen et al. 2009a). The error given is combined statistical and systematic and is expected to improve steadily with increasing time base line of the measurements; it has an important contribution from a degeneracy between M_\bullet and R_0 .

Therefore, external constraints on R_0 reduce the range of black hole mass allowed by the orbit measurements. Combining with their measurement of the NSC statistical parallax, Chatzopoulos et al. (2015) found $M_\bullet = (4.23 \pm 0.14) \times 10^6 M_\odot$. Using instead the overall best $R_0 = 8.2 \pm 0.1$ kpc from Section 3.2, the mass of the black hole becomes $M_\bullet = (4.2 \pm 0.2 \times 10^6) M_\odot$. This corresponds to a Schwarzschild radius of ~ 0.1 AU and a dynamical radius of influence of $r_{\text{infl}} \simeq 3.8$ pc, where the interior mass of the NSC $M(r < r_{\text{infl}}) = 2M_\bullet$ (Chatzopoulos et al. 2015). The inferred mass is also consistent with the orbital roulette value obtained by Beloborodov et al. (2006) from the stellar motions in the clockwise disk of young stars around Sgr A*. For $M_\bullet = 4.2 \times 10^6 M_\odot$ and a bulge velocity dispersion of $\sigma \simeq 113 \text{ km s}^{-1}$ (Section 4.2.3), the Milky Way falls below the best-fitting $(M_\bullet - \sigma)$ relation for elliptical galaxies and classical bulges by a factor of ~ 5 –6 (Kormendy & Ho 2013, Saglia et al. 2016).

From the orbit fit, any extended mass distribution within the orbit of S2 can contribute no more than 10% of the enclosed mass. The S2 star has approached the central mass within 125 AU at pericenter, requiring a minimum interior mass density of $\rho_\bullet(<125 \text{ AU}) = 5 \times 10^{15} M_\odot \text{ pc}^{-3}$. This is so large that one can rule out any known form of compact object other than a black hole (Reid 2009, Genzel et al. 2010). From matching the positions of SiO maser stars visible in both the NIR and the radio bands, the positions of the compact mass and the radio source Sgr A* have been shown to coincide within $\sim 2 \text{ mas} = 16 \text{ AU}$ (Reid et al. 2003, Gillessen et al. 2009b). The size of Sgr A* in millimeter radio observations is $< 1 \text{ AU}$ (Shen et al. 2005, Doeleman et al. 2008). These facts taken together make it highly likely that Sgr A* is the radiative counterpart of the black hole at the center of the Galaxy.

The apparent PM of Sgr A* relative to a distant quasar (J1745-283) has been measured with great precision using VLBI (Reid & Brunthaler 2004, Reid 2008). The PM perpendicular to the Galactic Plane is entirely consistent with the reflex motion of the vertical peculiar velocity of the Sun, with residual $-0.4 \pm 0.9 \text{ km s}^{-1}$, suggesting strongly that the SMBH is essentially at rest at the GC. Indeed the Brownian motion of the SMBH due to perturbations from the stars orbiting inside its gravitational influence radius is expected to be $\sim 0.2 \text{ km s}^{-1}$ (Merritt et al. 2007). On the assumption that Sgr A* is motionless at the GC, its measured PM in the Galactic Plane determines the total angular velocity of the Sun with high accuracy: $\Omega_{g,\odot} = 30.24 \pm 0.12 \text{ km s}^{-1} \text{ kpc}^{-1}$. For $R_0 = 8.2 \pm 0.1$ kpc from Section 3.2, the inferred value of the total solar tangential velocity relative to the GC is $V_{g,\odot} = 248 \pm 3 \text{ km s}^{-1}$. We return to these constraints in our discussion of the Galactic rotation curve in Section 6.4, which brings together many of the major themes of this review.

4. INNER GALAXY

4.1. Nuclear Star Cluster and Stellar Disk

Becklin & Neugebauer (1968) discovered an extended NIR source centered on Sgr A: the Milky Way's NSC. The source had a diameter of $\sim 5 \text{ arcmin} \simeq 12 \text{ pc}$ and was elongated along the Galactic Plane, and its surface brightness fell with projected radius on the sky $\propto R_s^{-0.8 \pm 0.1}$. NSCs

M_\bullet : mass of the Galactic SMBH, $4.2 \pm 0.2 \times 10^6 M_\odot$

$\rho_\bullet(<125 \text{ AU})$: mass density within the pericenter of star S2, $5 \times 10^{15} M_\odot \text{ pc}^{-3}$

r_{infl} : the Galactic SMBH's dynamical influence radius, 3.8 pc

$\Omega_{g,\odot}$: Sun's total angular velocity relative to Sgr A*, $30.24 \pm 0.12 \text{ km s}^{-1} \text{ kpc}^{-1}$

$V_{g,\odot}$: Sun's tangential velocity relative to Sgr A*, $248 \pm 3 \text{ km s}^{-1}$

Erratum >

NSC: nuclear star cluster

$L_{4.5,\text{NSC}}$: luminosity of the Galactic NSC, $(4.1 \pm 0.4) \times 10^7 L_{\odot}$

r_{NSC} : half-light radius of the Galactic NSC, 4.2 ± 0.4 pc

c/a : axis ratio of the Galactic NSC, 0.71 ± 0.04

M_{NSC} : Galactic NSC mass, $(1.8 \pm 0.3) \times 10^7 M_{\odot}$

NSD: nuclear stellar disk

r_{NSD} : break radius of the Galactic NSD, $\simeq 90$ pc

b_{NSD} : vertical scale height of the Galactic NSD, 45 pc

M_{NSD} : stellar mass of the Galactic NSD, $(1.4 \pm 0.6) \times 10^9 M_{\odot}$

are commonly seen in the centers of disk galaxies, and many contain an active galactic nucleus and thus an SMBH (e.g., Böker 2010). NIR spectroscopy has shown that most of the luminous stars in the Galactic NSC are old (> 5 Gyr) late-type giant and RCG stars (the “old” NSC, Pfuhl et al. 2011). But also a surprising number of massive early-type stars were found in this volume (Krabbe et al. 1995), including massive young stars in one and possibly two disks with diameters of 1–2 arcmin rotating around the SMBH (Paumard et al. 2006, Bartko et al. 2009) and a remarkable concentration of B stars within 1 arcsec of the SMBH, the so-called S stars (Eckart et al. 1995). Recent reviews on the NSC can be found in Genzel et al. (2010) and Schödel et al. (2014b).

The structure and dynamics of the NSC must be studied in the IR because of the very high extinction toward the GC ($A_K \sim 2.6$ mag, $A_V \sim 40$ mag; Fritz et al. 2011, Nishiyama et al. 2008). Recent analysis of *Spitzer*/IRAC 3.6- μm and 4.5- μm images (Schödel et al. 2014a) has shown that the old NSC is centered on Sgr A* and point-symmetric, and it is flattened along the Galactic Plane with minor-to-major projected axis ratio $q = 0.71 \pm 0.02$. Chatzopoulos et al. (2015) obtain $q = 0.73 \pm 0.04$ from fitting K -band star counts; they also show that NSC dynamics requires a flattened star cluster with an axis ratio consistent with this value. The NSC radial density profile is discussed in these papers and by Fritz et al. (2016). When fitting the 4.5- μm data with a Sérsic profile, Schödel et al. (2014a) obtain a total 4.5- μm luminosity $L_{4.5,\text{NSC}} = (4.1 \pm 0.4) \times 10^7 L_{\odot}$ and a spherical half-light radius of $r_{\text{NSC}} = 4.2 \pm 0.4$ pc.

The dynamical mass within 100 arcsec = 4 pc is $(8.9 \pm 1) \times 10^6 M_{\odot}$ (Chatzopoulos et al. 2015); thus $M/L_{4.5} = 0.44 \pm 0.06 M_{\odot}/L_{4.5,\odot}$, and the total mass of the NSC for the Sérsic model is $M_{\text{NSC}} = (1.8 \pm 0.3) \times 10^7 M_{\odot}$. An additional error in M_{NSC} not accounted for in this estimate comes from the fact that the surface density profile of the NSC goes below that of the much larger, surrounding nuclear stellar disk at projected $R_r \gtrsim 100$ arcsec, making its outer density profile uncertain (Chatzopoulos et al. 2015). The rotation properties and velocity dispersions were measured by Trippe et al. (2008) and Fritz et al. (2016) from stellar PMs and LOS velocities, and by Feldmeier et al. (2014) from NIR integrated spectra. The NSC is approximately described by an isotropic rotator model, with slightly slower rotation (Chatzopoulos et al. 2015). There are indications for a local kinematic misalignment in the LOS velocities but not in the PMs (Feldmeier et al. 2014, Fritz et al. 2016), which, if confirmed, might indicate some contribution to the NSC mass by infalling star clusters (Antonini et al. 2012); this needs further study. Another unsolved problem is the apparent core in the NSC density profile (Buchholz et al. 2009); this might indicate that the NSC is not fully relaxed, consistent with the relaxation time estimated as ≈ 10 Gyr throughout the NSC (Merritt 2013).

The old NSC is embedded in a nuclear stellar disk (NSD) that dominates the 3D stellar mass distribution outside ~ 30 pc (Chatzopoulos et al. 2015) and within ~ 200 – 400 pc (Launhardt et al. 2002). From star counts, its vertical density profile is near-exponential with scale height $b_{\text{NSD}} \simeq 45$ pc (Nishiyama et al. 2013). This confirms an earlier analysis of COBE data by Launhardt et al. (2002) that covers a larger area but with lower resolution. The projected density profile along the major axis ($|l|$) is approximately a power law $\propto |l|^{-0.3}$ out to ~ 90 pc; thereafter it drops steeply toward the NSD’s outer edge at ~ 230 pc, approximately $\propto |l|^{-2}$. The axis ratio of the NSD inferred in these papers from the star counts and NIR data is $\sim 3:1$ at small radii and $\sim 5:1$ on the largest scale. The total stellar mass estimated by Launhardt et al. (2002) is $M_{\text{NSD}} = (1.4 \pm 0.6) \times 10^9 M_{\odot}$, of order 10% of the mass of the bulge. The rotation of the NSD has been seen in OH/IR stars and SiO masers (Lindqvist et al. 1992, Habing et al. 2006) and with Apache Point Observatory Galaxy Evolution Experiment (APOGEE) stars (Schönrich et al. 2015), with an observed gradient $\simeq 150 \text{ km s}^{-1} \text{ deg}^{-1}$ and an estimated rotation velocity of $\approx 120 \text{ km s}^{-1}$ at $R \simeq 100$ pc. These data suggest a dynamical mass on the lower side of the estimated stellar mass range. The NSD is likely

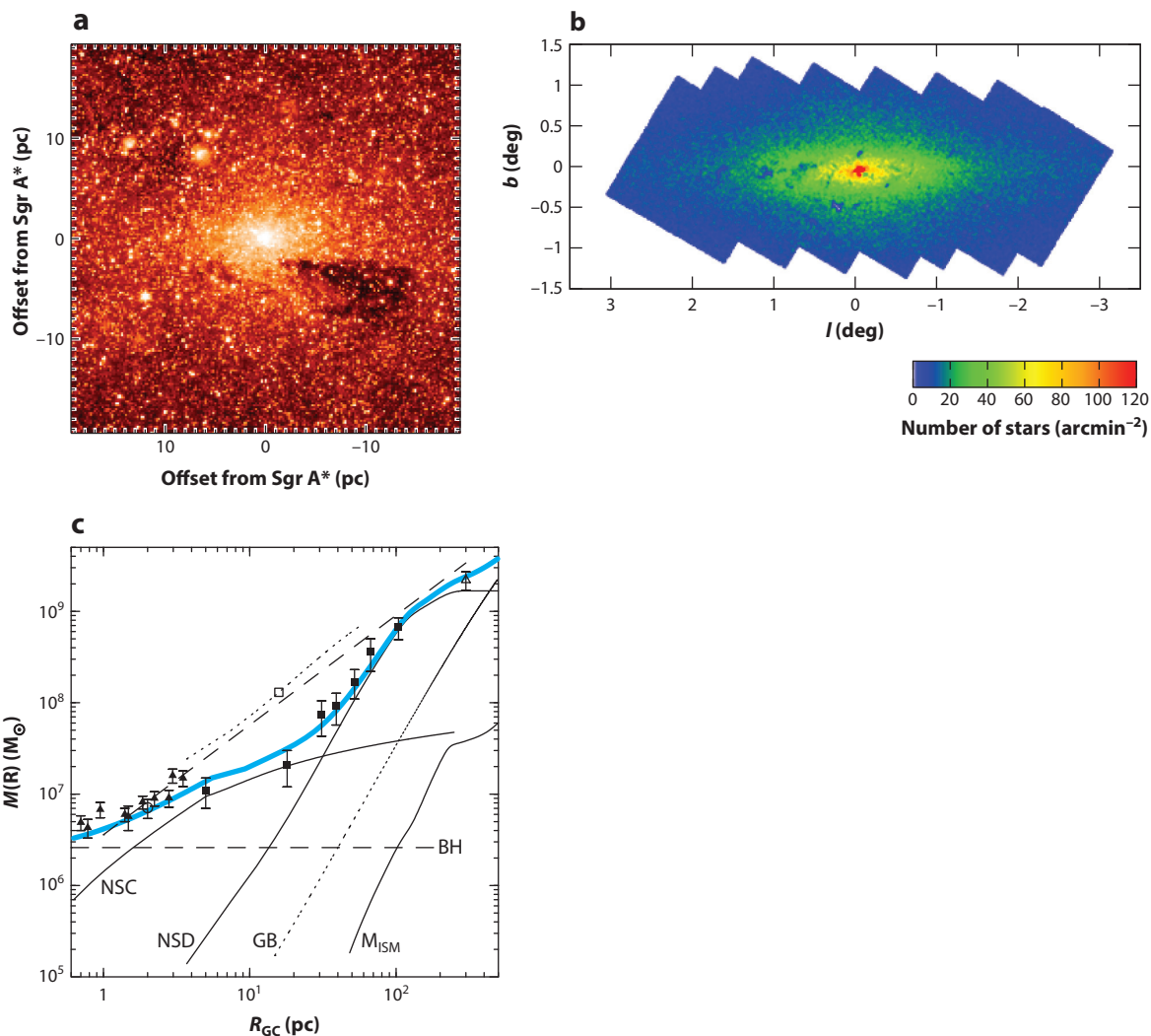


Figure 6

(a) Extinction-corrected 4.5- μm IRAC image of the nuclear star cluster (NSC). Adapted from Schödel et al. (2014a) with permission © ESO. (b) Extinction-corrected star count map of the nuclear stellar disk (NSD). The scale is 143 pc deg^{-1} at $R_0 = 8.2 \text{ kpc}$. The NSC is seen as the red dot in the center of this image. Adapted from Nishiyama et al. (2013) with permission. (c) Enclosed photometric mass within spherical radius for the NSC, NSD, Galactic bulge (GB), and total (*thick blue line*). Mass measurements overplotted as points with error bars. Adapted from Launhardt et al. (2002) with permission, © ESO.

related to past star formation in the zone of x_2 -orbits near the center of the barred potential (e.g., Molinari et al. 2011). Clearly, understanding the NSD better is relevant for the evolution of the Galactic bulge and probably also for the growth of the SMBH, and further information about its kinematics and stellar population would be important. **Figure 6** illustrates this still enigmatic Galactic component together with the NSC.

4.2. Bulge

For many years, the Galactic bulge was considered to be a structure built through mergers early in the formation of the Galaxy, now called a classical bulge. Particularly the old ages of bulge stars inferred from color-magnitude diagrams supported this view (Ortolani et al. 1995, Clarkson et al. 2008). The NIR photometry with the Diffuse Infrared Background Experiment instrument on board the COBE satellite first established the boxy nature of the bulge (Weiland et al. 1994, Binney et al. 1997), later confirmed by the 2MASS star count map (Skrutskie et al. 2006). Recent star count data have unambiguously established that the bulk of the bulge stars are part of a so-called box/peanut or b/p bulge structure representing the inner, 3D part of the Galactic bar (McWilliam & Zoccali 2010, Nataf et al. 2010, Wegg & Gerhard 2013), consistent with the observed cylindrical rotation (Kunder et al. 2012, Ness et al. 2013b). This corroborates long-standing evidence for a barred potential in the bulge region from noncircular motions seen in H_I and CO longitude-velocity (lv) diagrams (Binney et al. 1991, Englmaier & Gerhard 1999). The central parts of the Galaxy also contain the dense NSD, and some have argued for a separate, 200-pc-scale nuclear bar (Alard 2001, Rodriguez-Fernandez & Combes 2008). Finally, the peak in the density of the inner stellar halo is found in this region as well. Disentangling these various components clearly requires the best data possible. Results to date and open issues are summarized below. For more extensive reviews of the Galactic bulge see Rich (2013), Gonzalez & Gadotti (2016), and Shen & Li (2016).

4.2.1. The Galactic b/p bulge. A large fraction of the bulge stars follow a rotating, barred, b/p-shaped bulge with exponential density distribution, similar to the inner 3D part of an evolved N -body bar. The best available structural information for the dominant bulge population comes from large samples of RCGs, for which individual distances can be determined to $\sim 10\%$ accuracy. These He-core-burning stars have a narrow range of absolute magnitudes and colors, $\sigma(K_s) \simeq 0.17$ and $\sigma(J-K_s) \simeq 0.05$, and are predicted to trace the stellar population within 10% for metallicities in the range $[0.02, 1.5]$ solar (Salaris & Girardi 2002). In the color-magnitude diagram, RCGs appear spread because of distance, reddening, age (by $\sim 0.03 \text{ Gyr}^{-1}$ in K_s at age 10 Gyr), and metallicity [by $\sigma_{K_s}(\text{Fe}/\text{H}) \sim 0.11$ for the measured bulge metallicity distribution]. Among the 25,500 stars of the Abundances and Radial Velocity Galactic Origins Survey (ARGOS), RCGs are prominent down to $[\text{Fe}/\text{H}] = -1.0$, which comprises $\sim 95\%$ of their sample (Ness et al. 2013a); i.e., RCGs are representative for most of the bulge stars.

Using ~ 8 million RCGs from the VVV survey (Minniti et al. 2010) over the region $-10^\circ \leq l \leq 10^\circ$, $-10^\circ \leq b \leq 5^\circ$, Wegg & Gerhard (2013) obtained RCG LOS density distributions for ~ 300 sightlines outside the most crowded region $|b| < 1^\circ$ and combined these to a 3D map of the bulge RCG density assuming eightfold triaxial symmetry (**Figure 7a**). As shown in the figure, root-mean-square (rms) variations between eightfold symmetric points in the final map are indeed small; there is no evidence for asymmetries in the volume of the RCG measurement ($\pm 2.2 \times \pm 1.4 \times \pm 1.2 \text{ kpc}$). The RCG bulge is strongly barred, with a face-on projected axis ratio of $\sim 1:2.1$ for isophotes reaching $\sim 2 \text{ kpc}$ along the major axis; it has a strong b/p shape viewed side-on and a boxy shape as seen from the Sun, consistent with the earlier COBE and 2MASS data. Unsharp masking (Portail et al. 2015b) results in a strong off-centered X-shape structure (**Figure 7b**), similar to some galaxies in the sample of Bureau et al. (2006); see also Nataf et al. (2015).

The near side of the b/p bulge has its major axis in the first Galactic quadrant ($0^\circ < l < 90^\circ$). The bar angle between the major axis and the Sun-GC line found by Wegg & Gerhard (2013) is $\phi_{\text{bp}} = 27^\circ \pm 2^\circ$, with most of the error being systematic. This is consistent with earlier parametric determinations from OGLE I -band RCG star counts ($29^\circ \pm 2^\circ$, Cao et al. 2013; $25^\circ \pm 2^\circ$,

b/p: box/peanut

ϕ_{bp} : bar angle of the Galactic b/p bulge, $27^\circ \pm 2^\circ$

$(b/a)_{\text{bp}}$: axis ratio of the Galactic b/p bulge from top, 0.5 ± 0.05

$(c/a)_{\text{bp}}$: edge-on axis ratio of the Galactic b/p bulge ($x \sim 0$), 0.26

b_{bp} : vertical scale height of the Galactic b/p bulge ($x \sim 0$), 180 pc

x_X : radius of maximum X of the Galactic b/p bulge, $1.5 \pm 0.2 \text{ kpc}$

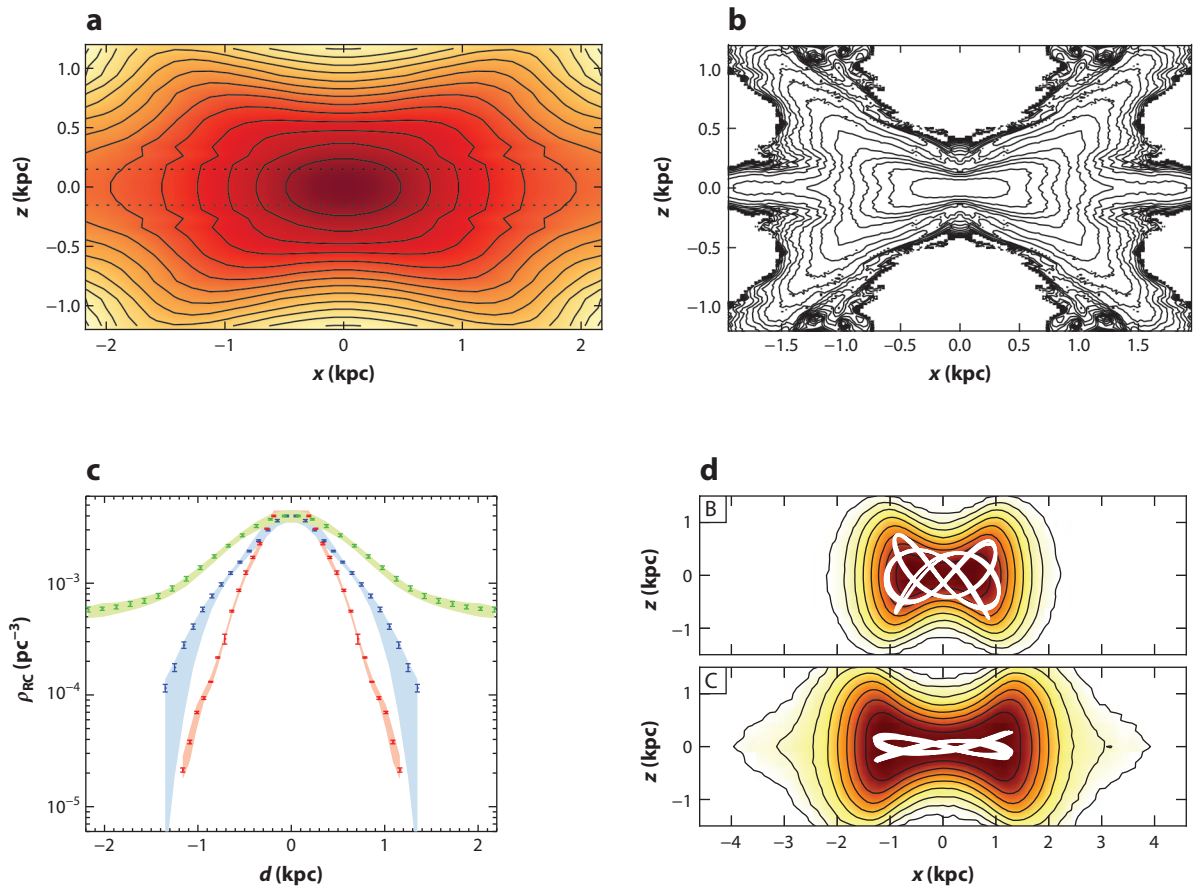


Figure 7

The Galactic box/peanut (b/p) bulge density measured from K -band RCG star counts. (a) Side-on projection showing the prominent b/p shape. Data from Wegg & Gerhard (2013); figure after Portail et al. (2015b). (b) X-structure in unsharp-masked image. Adapted from Portail et al. (2015b) with permission. (c) Density profiles along the bulge principal axes (x , y , z) in green, blue, and red (respectively). The error bars show the root-mean-square variations between eightfold symmetric points around the triaxially symmetric 3D map. Colored regions show estimated systematic errors. The density is typically accurate to $\sim 10\%$. Exponential scale lengths along the (x , y , z)-axes are (0.70:0.44:0.18) kpc near the center. Adapted from Wegg & Gerhard (2013) with permission. (d) Major orbit classes B, C supporting the b/p shape in dynamical models of the b/p bulge. Adapted from Portail et al. (2015a) with permission.

Rattenbury et al. 2007; 20° – 30° , Stanek et al. 1997), from nonparametric inversion of 2MASS red giant star counts (20° – 35° , López-Corredoira et al. 2005), and from modeling the asymmetry of the COBE NIR photometry ($\sim 25^\circ \pm 10^\circ$; Dwek et al. 1995, Binney et al. 1997, Freudenreich 1998, Bissantz & Gerhard 2002). The global bulge axis ratios obtained with parametric star count models are typically (1 : 0.4 : 0.3), similar to those found from modeling the COBE data. However, it is clear from **Figure 7** that a single vertical axis ratio does not capture the shape of the b/p bulge. **Figure 7c** shows that the density distributions inside ~ 1 kpc are nearly exponential, with scale lengths ($b_x : b_y : b_z$) = (0.70 : 0.44 : 0.18) kpc and axis ratios (10 : 6.3 : 2.6) (Wegg & Gerhard 2013). Further down the major axis, b_z/b_x increases to ~ 0.5 at $x \sim 1.5$ kpc, where the X shape is maximal, and then decreases rapidly outward.

4.2.2. Inner bulge and disk structure. The structure of the inner Galactic disk between the NSD and $R \sim 2$ kpc is not well known due to heavy extinction and crowding. Observations of maser stars and VVV Cepheids indicate a barred disk of young stars (Habing et al. 2006, Dékány et al. 2015). The cold kinematics of young bar stars has likely been seen in APOGEE LOS velocity histograms (Aumer & Schönrich 2015). The short $b_z = 180$ -pc vertical scale height in the bulge is perhaps indicative of a central disk-like, high-density, pseudo-bulge structure, as is seen in many early- and late-type b/p bulge galaxies (Bureau et al. 2006, Kormendy & Barentine 2010). NIR RCG star counts at $b = \pm 1^\circ$ have confirmed a structural change in the RCG longitude profiles at $|l| \simeq 4^\circ$ (Nishiyama et al. 2005, Gonzalez et al. 2011a, Wegg & Gerhard 2013). This has been interpreted by means of an N -body model in terms of a rounder, more nearly axisymmetric central parts of the b/p bulge (Gerhard & Martinez-Valpuesta 2012). As predicted by the model, the transition at $|l| \simeq 4^\circ$ is confined to a few degrees from the Galactic Plane (Gonzalez et al. 2012).

The nuclear bulge within ~ 200 pc is dominated by the NSD. Based on longitudinal asymmetries in a map of projected 2MASS star counts Alard (2001) presented indications for a 200-pc scale nuclear bar separate from the b/p bulge-bar. However, the large-scale Galactic bar by itself leads to similar inverted asymmetries in the center, just by projection (Gerhard & Martinez-Valpuesta 2012), so the observed asymmetries are not a tell-tale signature. Unfortunately, the distance resolution of the RCG is not sufficient to investigate the LOS structure of a tilted nuclear bar. Thus the most promising tests appear to be with models of the nuclear gas flow (Rodriguez-Fernandez & Combes 2008), but this requires understanding the larger-scale properties of the gas flow better (see Section 4.4), which influence the nuclear gas flow. Further studies in the IR, both photometric and spectroscopic, are clearly needed to shed more light on the inner bulge.

4.2.3. Does the Milky Way have a classical bulge? Kinematics and metallicities of bulge stars. Bulges in several disk galaxy-formation models have been found to harbor a rapid early starburst component, as well as a second component that forms later after disk build-up and instabilities and/or minor mergers (Samland & Gerhard 2003, Obreja et al. 2013). The former could be associated with a classical bulge even in the absence of a significant early merger-built bulge. The Milky Way bulge has a well-established vertical metallicity gradient (Zoccali et al. 2008, Johnson et al. 2011, Gonzalez et al. 2013) that has often been taken as the signature of a dissipatively formed classical bulge (see Pipino et al. 2008). However, because violent relaxation is inefficient during the bar and buckling instabilities, preexisting metallicity gradients, such that stars with lower binding energies have lower metallicities, would survive as outward metallicity gradients in the final b/p bulge (Martinez-Valpuesta & Gerhard 2013, Di Matteo et al. 2014). Recent spectroscopic surveys have attributed the vertical metallicity gradient to a superposition of several metallicity components whose relative contributions change with latitude (Babusiaux et al. 2010, Ness et al. 2013a). Hence the signature of a classical bulge must be found with more detailed kinematic and chemical observations.

The mean LOS rotation velocities of bulge stars are nearly independent of latitude, showing cylindrical rotation as is common in barred bulges. First found with planetary nebulas (Beaulieu et al. 2000), this was shown conclusively with Bulge Radial Velocity Assay (BRAVA) (Kunder et al. 2012), ARGOS (Ness et al. 2013b), and GIRAFFE Inner Bulge Survey (GIBS; Zoccali et al. 2014). Rotation velocities reached at $l \sim 10^\circ$ are ~ 75 km s $^{-1}$. LOS velocity dispersions at $l \sim 0$ are ~ 80 km s $^{-1}$ at $|b| = 8^\circ$ and increase rapidly toward the Galactic Plane, reaching ~ 120 km s $^{-1}$ in Baade’s window at $|b| = 4^\circ$. Based on the dynamical model of Portail et al. (2015b; see Section 4.2.4) mass-weighted velocity dispersions inside the bulge half-mass radius are $(\sigma_x^b, \sigma_y^b, \sigma_z^b) \approx (135, 105, 96)$ km s $^{-1}$, and the rms is $\sigma_{\text{rms}}^b \approx 113$ km s $^{-1}$, to within 3 km s $^{-1}$.

The ARGOS survey mapped the kinematics for different metallicities, showing that higher/lower metallicity stars have lower/higher velocity dispersions. Soto et al. (2007) and Babusiaux et al. (2010) found differences between the vertex deviations of metal-rich and metal-poor bulge stars and argue for the existence of two main bulge stellar populations, of which only the more metal-rich one follows the bar. Rojas-Arriagada et al. (2014) find two about equally numerous, metal-rich and metal-poor components in the metallicity distribution of their fields, whereas Ness et al. (2013a,b) find evidence for five populations. The metal-rich components trace the X shape and hence the barred bulge, but the origin of the metal-poor stars ($[\text{Fe}/\text{H}] \lesssim -0.5$) is currently debated. They could represent an old bulge formed through early mergers or a thick disk component participating in the instability together with the inner stellar halo (e.g., Babusiaux et al. 2010, Di Matteo et al. 2014).

Large numbers of RR Lyrae stars found in the OGLE and VVV bulge surveys have shown that the most metal-poor ($[\text{Fe}/\text{H}] = -1.0 \pm 0.2$), old population does not participate in the b/p bulge (Dékány et al. 2013, Pietrukowicz et al. 2015), consistent with the ARGOS result that only stars with $[\text{Fe}/\text{H}] \gtrsim 0.5$ participate in the split red clump (Ness et al. 2012). The RR Lyrae stars show no significant rotation (Kunder et al. 2016). By contrast, the ARGOS stars with $[\text{Fe}/\text{H}] < -1$ rotate still fairly rapidly; whether they could be stars from the stellar halo or a low-mass classical bulge spun up by the b/p bulge (Saha et al. 2012) or whether they could include a component of thick disk stars must still be checked in detail.

In summary, it is unclear at this time whether the Milky Way contains any classical bulge at all—comparing N -body-simulated b/p bulge models to the BRAVA data, Shen et al. (2010) found that the cylindrical rotation in the Galactic bulge could be matched by their models only if the initial models contained a classical bulge with $\lesssim 8\%$ of the initial disk mass ($\lesssim 25\%$ of the final bulge mass), and none was needed. However, there is strong evidence from structural and kinematic properties that the major part of the Galactic bulge was built from the disk through evolutionary processes similar to those observed in galaxy evolution simulations, as is also inferred for many external galaxies (so-called secular evolution; Kormendy 2013, Sellwood 2014).

4.2.4. Mass and mass-to-light ratio in the bulge. The stellar mass of the bulge can be estimated from a photometric model combined with a stellar population model. For example, Dwek et al. (1995) obtained $1.3 \times 10^{10} M_{\odot}$ from the COBE NIR luminosity and a Salpeter IMF ($2.0 \times 10^{10} M_{\odot}$ rescaled for Kroupa IMF, Licquia et al. 2015). Valenti et al. (2016) obtained a projected mass of $2.0 \pm 0.3 \times 10^{10} M_{\odot}$ from scaling the measured mass function in a small bulge field to the whole bulge using RCGs. The stellar mass corresponds to the dynamical mass only if the contribution of dark matter in the bulge region is unimportant.

The dynamical mass in the bulge can be determined from either gas kinematics in the bulge region or stellar kinematics combined with a dynamical model. For a barred bulge, simple rotation curve analysis does not apply, and analysis of the full gas velocity field requires hydrodynamical models (see Section 4.4). Stellar dynamical models require a well-determined tracer density, i.e., an NIR luminosity or tracer density distribution. Furthermore, because the dominant part of the Galactic bulge is the inner b/p part of the Galactic bar, the result depends somewhat on the spatial region defined as the bulge.

Zhao et al. (1994) built a self-consistent model of the bar/bulge using the Schwarzschild method and found a total bulge mass of $2 \times 10^{10} M_{\odot}$. Kent (1992) modeled the $2.4\text{-}\mu\text{m}$ Spacelab emission with an oblate isotropic rotator and constant mass-to-light ratio, finding a mass of $1.8 \times 10^{10} M_{\odot}$. Bissantz et al. (2003) determined the circular velocity at 2.2 kpc to be 190 km s^{-1} , modeling gas dynamics in the potential of the deprojected COBE NIR luminosity distribution from Bissantz

$M_{\text{b}}^{\text{dyn}}$: dynamical mass in the VVV bulge region, $1.84 \pm 0.07 \times 10^{10} M_{\odot}$

M_{b}^* : stellar mass in the VVV bulge region, $(1.4\text{--}1.7) \times 10^{10} M_{\odot}$

$M_{\text{b}}^*/M_{\text{*}}$: stellar mass in the bulge region to total stellar mass, 0.3 ± 0.06

$f_{\text{b,DM}}$: dark matter fraction in the VVV region, 10–25%

$(\sigma_x^{\text{b}}, \sigma_y^{\text{b}}, \sigma_z^{\text{b}}, \sigma_{\text{rms}}^{\text{b}})$: mass-weighted velocity dispersions within half-mass radius along (x, y, z) and rms, (135, 105, 96, 113) km s^{-1}

$M_{\text{clb}}/M_{\text{b}}^*$: classical bulge fraction, 0–25%

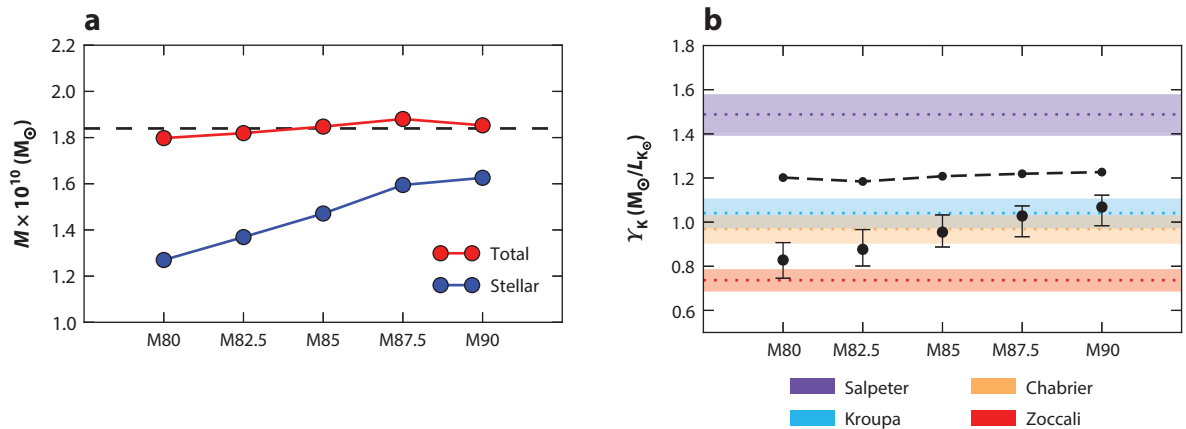


Figure 8

(a) Mass of the Galactic bulge in the VVV box for the five dynamical models of Portail et al. (2015b) with different dark matter halos. The blue curve refers to the stellar mass, whereas the red curve refers to the total mass. (b) Stellar mass-to-light ratio in the K band for the same five models. The model errors shown are dominated by systematic effects. The different colored lines indicate predictions for different initial mass functions (IMFs), as stated in the legend. The most recent measurements (Calamida et al. 2015) are close to a Kroupa IMF. The black dashed line is an estimate of the highest allowed mass-to-light ratio obtained by turning all dark matter in the VVV box into stars. This rules out a Salpeter IMF for the Galactic bulge with age 10 Gyr. Adapted from Portail et al. (2015b) with permission.

& Gerhard (2002). Assuming spherical symmetry, this leads to a total bulge mass of about $1.85 \times 10^{10} M_{\odot}$. However, several other studies have found lower masses (see Licquia et al. 2015).

In the most recent study, Portail et al. (2015b) find a very well-constrained total dynamical mass of $1.84 \pm 0.07 \times 10^{10} M_{\odot}$ in the VVV bulge region (the box $\pm 2.2 \times \pm 1.4 \times \pm 1.2$ kpc), by fitting made-to-measure dynamical models to the combined VVV RCG star density and BRAVA kinematics (Figure 8). The data can be fit well by models with a range of dark-to-stellar mass ratios. Comparing the implied total surface mass density with the COBE surface brightness and stellar population models, a Salpeter IMF for a 10-Gyr-old population can be ruled out, predicting significantly more mass than is dynamically allowed. For an IMF between those of Kroupa (2001), Chabrier (2003), and Zoccali et al. (2000), 10–40% of the mass in the bulge region would be required to be in dark matter. Recently Calamida et al. (2015) derived the bulge IMF in the SWEEPS (Sagittarius Window Eclipsing Extrasolar Planet Search) field, removing foreground disk stars, and found a double power-law form remarkably similar to a Kroupa or Chabrier IMF. The models of Portail et al. (2015b) then predict a total stellar mass in this region of $1.4\text{--}1.7 \times 10^{10} M_{\odot}$, including stars in the inner disk, and a dark matter fraction of 10–25%. The estimated total stellar mass in the bulge and disk of the Galaxy is $M_{*} \approx 4.7\text{--}5.7 \times 10^{10} M_{\odot}$ (Section 6.4), so the ratio of stellar mass in the bulge region to total stellar mass is $M_{\text{b}}^{*}/M_{*} = 0.3 \pm 0.06$.

The stellar mass involved in the peanut shape is important for constraining the origin of the bulge populations (Section 4.2.3). Li & Shen (2012) applied an unsharp masking technique to the side-on projection of the model of Shen et al. (2010), removing an elliptical bulge model from the total. This revealed a centered X structure accounting for about 7% of their model bulge. Portail et al. (2015b) removed a best-matched ellipsoidal density from the 3D RCG bulge density of Wegg & Gerhard (2013), finding that 24% of the bulge stellar mass remained in the residual X shape. Most reliable would be a dynamical, orbit-based definition of the mass in the peanut shape. However, in the bulge models of Portail et al. (2015b), stars in the X shape do not stream along

$x_1 v_1$ “banana” orbits (Pfenniger & Friedli 1991), which follow the arms of the X shape. Instead, the peanut shape is supported by “brezel” orbit families, which contribute density everywhere between the arms of the X structure (Portail et al. 2015a; see **Figure 7d**). In these models, the fraction of stellar orbits that contribute to the X structure account for 40–45% of the bulge stellar mass.

4.3. The “Long Bar” Outside the Bulge

In N -body models for disk galaxy evolution, b/p bulges are the inner 3D parts of a longer, planar bar that formed through buckling out of the galaxy plane and/or orbits in vertical resonance (Combes et al. 1990, Raha et al. 1991, Athanassoula 2005). There is also evidence that b/p bulges in external galaxies are embedded in longer, thinner bars (Bureau et al. 2006). Thus also the Milky Way is expected to have a thin bar component extending well outside the b/p bulge. However, finding the Galactic planar bar and characterizing its properties has proven difficult, because of intervening dust extinction and the superposition with the star-forming disk at low latitudes toward the inner Galaxy.

Hammersley et al. (2000) drew attention to an overdensity of stars in the Milky Way disk plane reaching outward from the bulge region to $l \simeq 28^\circ$. NIR star count studies with UK Infrared Deep Sky Survey (UKIDSS) and other surveys confirmed this structure (Cabrera-Lavers et al. 2007, 2008). Its vertical scale length is less than 100 pc, so this is clearly a disk feature. With *Spitzer* Galactic Legacy Infrared Mid-Plane Survey Extraordinaire (GLIMPSE) mid-IR star counts, which are less affected by dust than K -band data, Benjamin et al. (2005) similarly found a strong bar-like overdensity of sources at positive longitudes. Because of its wide longitude extent and the narrow extent along the LOS this structure was termed the long bar.

Based on the combined 2MASS, UKIDSS, VVV, and GLIMPSE surveys, Wegg et al. (2015) investigated the long bar in a wide area in latitude and longitude, $|b| \leq 9^\circ$ and $|l| \leq 40^\circ$, using RCG stars and correcting for extinction star by star. They found that the Galactic bar extends to $l \sim 25^\circ$ at $|b| \sim 5^\circ$ from the Galactic Plane and to $l \sim 30^\circ$ at lower latitudes. Their long bar has an angle to the LOS of 28° – 33° , which is consistent with the bar angle inferred for the bulge at $|l| < 10^\circ$. The vertical scale height of the RCG stars decreases continuously from the b/p bulge to the long bar. Thus the central b/p bulge appears to be the vertical extension of a longer, flatter bar, similar to that seen in external galaxies and N -body models.

These recent results are based on a larger and more uniform data base and on a more uniform analysis than the earlier work on the long bar, using cross-checked star-by-star extinction corrections and a statistical rather than color-magnitude-diagram-based selection of RCG stars. This leads to smaller errors in the RCG magnitude distributions and reduced scatter between neighboring fields, particularly near the Galactic Plane. These results therefore supersede in particular the earlier claim that the long bar is an independent bar structure at angle $\sim 45^\circ$ and misaligned with the b/p bulge.

Comparing parametric models for the RCG magnitude distributions with the data, Wegg et al. (2015) find a total bar (half) length of $R_{\text{lb}} = 5.0 \pm 0.2$ kpc. Projections of their best model for the combined bulge and long bar are shown in **Figure 9**. Panel *a(i)* illustrates the asymmetries, seen by observers at the Sun, due to the bar shape and geometry. The side-on view in panel *a(iii)* clearly shows the Milky Way’s central b/p bulge and the decrease of the scale height in the long-bar region. In the central face-on view, panel *a(ii)*, the projected b/p bulge resembles the bar-lens structures described by Laurikainen et al. (2011), which are considered to be the more face-on counterparts of b/p bulges (Laurikainen et al. 2014; see the image of NGC 4314 in **Figure 10**).

In the same analysis, Wegg et al. (2015) find evidence for two vertical scale heights in the long bar, also illustrated in **Figure 9b**. The thin bar component has $b_{\text{ub}} \simeq 180$ pc, and its density

ϕ_{lb} : angle of the Galactic long bar, 28° – 33°

R_{lb} : half-length of the Galactic bar, 5.0 ± 0.2 kpc

b_{ub} : scale height of the Galactic thin bar, 180 pc

b_{slb} : scale height of the Galactic superthin bar, 45 pc

M_{db} : stellar mass of the Galactic thin bar, $\sim 7 \pm 1 \times 10^9 M_\odot$

M_{slb} : stellar mass of the Galactic superthin bar, $\sim 3 \times 10^9 M_\odot$

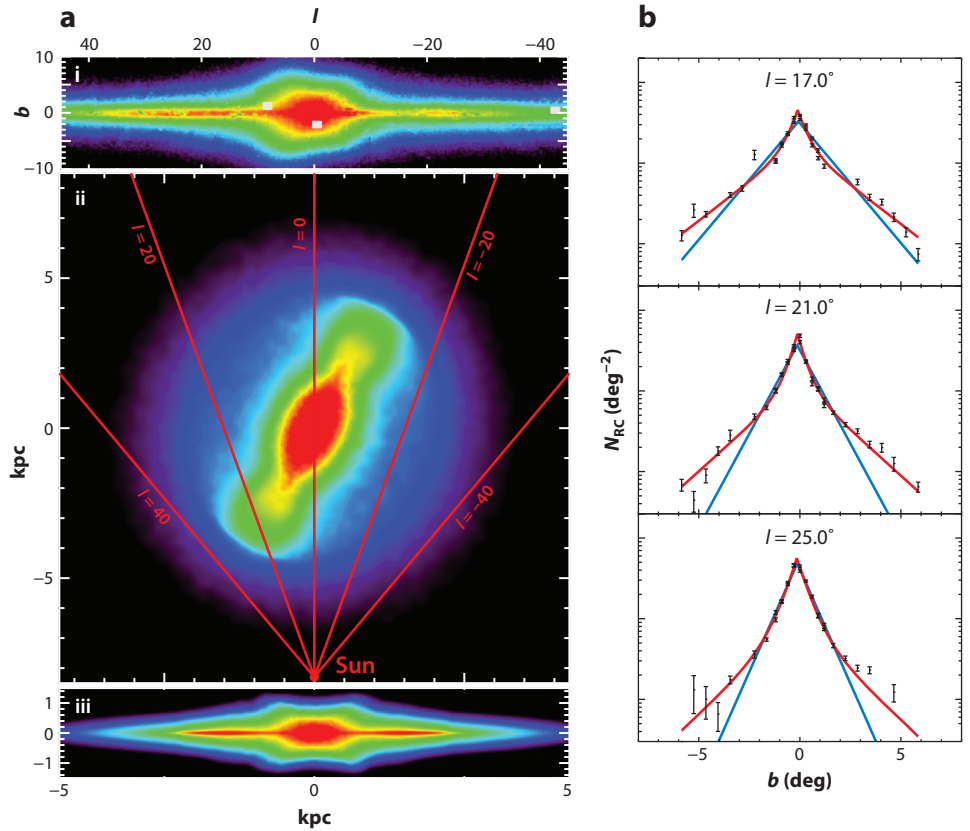


Figure 9

(a) Projections of the Galactic box/peanut (b/p) bulge and long bar reconstructed from near-IR (NIR) star counts. (i) Inner Galaxy as seen from the Sun, in bright star counts complete across several NIR surveys. (ii) Projection of best-fitting red clump giant (RCG) star count model as seen from the North Galactic Pole. Viewing directions from the Sun are indicated for longitudes $|l| = 0^\circ, 20^\circ, 40^\circ$. (iii) Side-on view showing the transition from the b/p bulge to the long bar and disk. (b) Vertical surface density profiles of RCG stars for several longitude slices in the long-bar region. Blue lines show single exponential fits. Red lines show the preferred double exponential model consisting of a superthin ($b_z = 45$ pc) and a thin bar component ($b_z = 180$ pc). The fraction of stars in the superthin component increases with longitude. Adapted from Wegg et al. (2015) with permission.

decreases outward roughly exponentially; it is reminiscent of the old thin disk near the Sun. The second, superthin bar component has $b_{\text{slb}} \simeq 45$ pc, and its density increases outward toward the bar end where it dominates the RCG counts. The short scale height is similar to the 60–80-pc superthin disk found in the edge-on spiral galaxy NGC 891 (Schechtman-Rook & Bershadsky 2013). Stars in this component have an estimated vertical velocity dispersion of $\sigma_z \simeq 20\text{--}30$ km s $^{-1}$ and should be younger than the thin component. However, to have formed RCGs they must have ages of at least >0.5 Gyr, but star-forming galaxies have a strong bias toward ages around ~ 1 Gyr (Salaris & Girardi 2002). Such a younger bar component could arise from star formation toward the bar end or from disk stars captured by the bar.

The dynamical mass of the long bar component has not yet been determined. The stellar mass was estimated by Wegg et al. (2015) from the RCG density using isochrones and a Kroupa

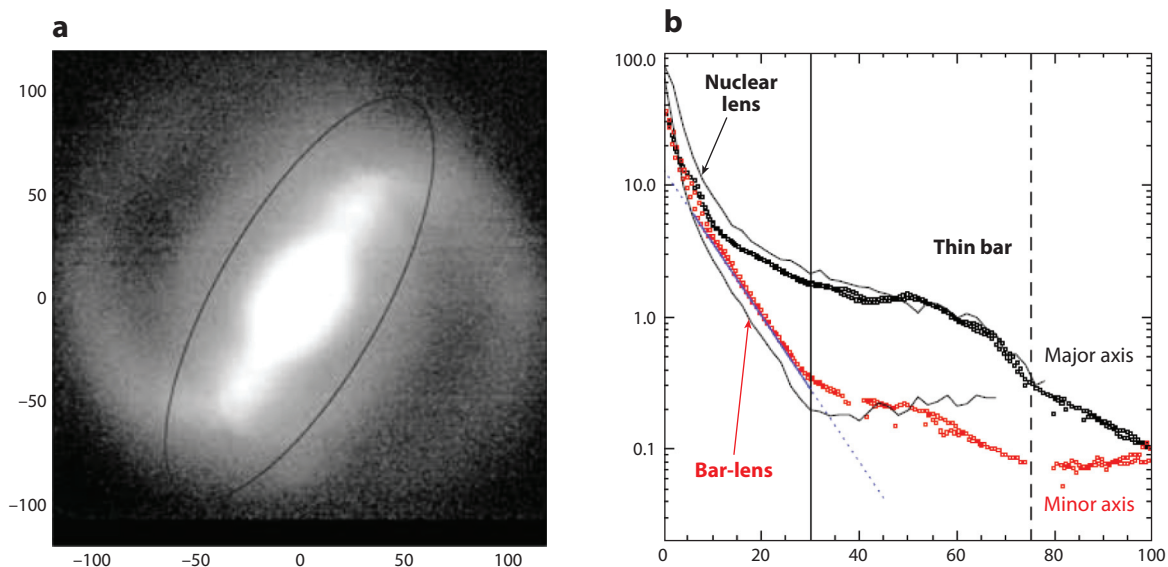


Figure 10

(a) *K*-band image of the bar-lens galaxy NGC 4314, with similar morphology as the face-on image of the Galactic box/peanut bulge and long bar in **Figure 9**. Scaled and reflected to the rotation of the Milky Way, the Sun would be located at roughly (−110 arcsec, −60 arcsec) in this image. Adapted from Laurikainen et al. (2011) with permission. (b) Major and minor axis surface brightness profiles for NGC 4314. Adapted from Laurikainen et al. (2014) with permission.

IMF. This resulted in a total nonaxisymmetric mass for the thin bar component of $M_{\text{tlb}} \simeq 6\text{--}8 \times 10^9 M_{\odot}$, assuming a 10-Gyr-old, α -enhanced population, and $M_{\text{slb}} \sim 3 \times 10^9 M_{\odot}$ for the superthin component, assuming a constant past SFR. Owing to its 5-kpc half-length and its total mass of $\sim 10^{10} M_{\odot}$, the long bar may have quite some impact on the dynamics of the Galactic disk inside the Solar Circle, particularly on the gas flow and the spiral arms but perhaps also on surface density and scale-length measurements in the disk (see **Figure 10**). In Section 4.4 below, we summarize constraints on the bar’s corotation radius, which must be larger than R_{lb} .

4.4. Pattern Speed

The pattern speed Ω_{b} of the b/p bulge and bar, or equivalently its corotation radius R_{CR} , has great importance for the dynamics of the bar and surrounding disk. Despite a number of different attacks on measuring Ω_{b} its value is currently not accurately known. An upper limit comes from determining the length of the bar and assuming that, like in external galaxies, the Galactic bar is a fast bar, i.e., $\mathcal{R} = R_{\text{CR}}/R_{\text{lb}} = 1.2 \pm 0.2$ (Aguerri et al. 2003, 2015). Here the 1.0 lower limit is based on the fact that theoretically bars cannot extend beyond their corotation radius because the main x_1 -orbit family supporting the bar becomes unstable (Contopoulos 1980, Athanassoula 1992). The length of the long bar from star counts is $R_{\text{lb}} \simeq 5.0 \pm 0.2$ kpc, and the length of the thin bar component alone is $R_{\text{tlb}} \simeq 4.6 \pm 0.3$ kpc (Wegg et al. 2015); thus a strong lower limit is $R_{\text{CR}} = 4.3$ kpc, and a more likely range is $R_{\text{CR}} = 5.0\text{--}7.0$ kpc, or $\Omega_{\text{b}} \sim 34\text{--}47 \text{ km s}^{-1} \text{ kpc}^{-1}$ for $\Theta_0 = 238 \text{ km s}^{-1} = \text{constant}$ (Section 6.4).

Early determinations appeared to give rather high values of Ω_{b} . The most direct method applied a modified version of the Tremaine-Weinberg continuity argument to a complete

Ω_b : pattern speed of
the Galactic bar,
 $43 \pm 9 \text{ km s}^{-1} \text{ kpc}^{-1}$

R_{CR} : corotation
radius of the Galactic
bar, 4.5–7.0 kpc

sample of OH/IR stars in the inner Galaxy (Debattista et al. 2002), giving $\Omega_b = 59 \pm 5 \pm 10$ (sys) $\text{km s}^{-1} \text{ kpc}^{-1}$ for $(R_0, \Theta_0) = (8 \text{ kpc}, 220 \text{ km s}^{-1})$ but depending sensitively on the radial motion of the local standard of rest (LSR).

More frequently, the pattern speed of the bar has been estimated from hydrodynamic simulations comparing the gas flow with observed Galactic CO and H I lv -diagrams. These simulations are sensitive to the gravitational potential, and generally reproduce a number of characteristic features in the lv -plot, but none reproduces all observed features equally well. Consequently, the derived pattern speeds depend somewhat on the gas features emphasized. Englmaier & Gerhard (1999) and Bissantz et al. (2003) estimated $55\text{--}65 \text{ km s}^{-1} \text{ kpc}^{-1}$ ($R_{CR} = 3.4 \pm 0.3 \text{ kpc}$), matching the terminal velocity curve, spiral arm tangents, and ridges in the lv -plot. Fux (1999) obtained $\sim 50 \text{ km s}^{-1} \text{ kpc}^{-1}$ ($R_{CR} = 4\text{--}4.5 \text{ kpc}$) from a comparison with various reference features in the CO lv -plot; Weiner & Sellwood (1999) obtained $42 \text{ km s}^{-1} \text{ kpc}^{-1}$ ($R_{CR} = 5.0 \text{ kpc}$) from matching the extreme H I velocity contour; Rodriguez-Fernandez & Combes (2008) obtained $30\text{--}40 \text{ km s}^{-1} \text{ kpc}^{-1}$ and $R_{CR} = 5\text{--}7 \text{ kpc}$ matching to the Galactic spiral arm pattern. The most recent analysis based on a range of potential parameters is that by Sormani et al. (2015). They conclude that overall a pattern speed of $\Omega_b = 40 \text{ km s}^{-1} \text{ kpc}^{-1}$ corresponding to $R_{CR} = 5.6 \text{ kpc}$ matches best the combined constraints from the terminal velocity envelope, the central velocity peaks, and the spiral arm traces in the lv -diagram (for $R_0, \Theta_0 = 8 \text{ kpc}, 220 \text{ km s}^{-1}$).

Stellar dynamical models of the Galactic b/p bulge also depend on Ω_b and give estimated ranges for its value. Shen et al. (2010) and Long et al. (2012) find $\Omega_b \simeq 40 \text{ km s}^{-1} \text{ kpc}^{-1}$ for the same N -body model matched to the BRAVA kinematic data. The recent models of Portail et al. (2015b) fitted additionally to the RCG density from Wegg & Gerhard (2013) give values in the range of $\Omega_b \sim 25\text{--}30 \text{ km s}^{-1} \text{ kpc}^{-1}$, placing corotation in the range of $R_{CR} > 7.2 \text{ kpc}$ (for $R_0, \Theta_0 = 8.3 \text{ kpc}, 220 \text{ km s}^{-1}$). These values could depend somewhat on the still uncertain gravitational potential in the long bar region.

A final method is based on the interpretation of star streams observed in the distribution of stellar velocities in the Solar Neighborhood as due to resonant orbit families near the outer Lindblad resonance of the bar (Kalnajs 1991, Dehnen 2000). Dehnen (2000) estimates $\Omega_b = (1.85 \pm 0.15) \Theta_0/R_0$ [$51 \pm 4 \text{ km s}^{-1} \text{ kpc}^{-1}$ for $(R_0, \Theta_0) = (8 \text{ kpc}, 220 \text{ km s}^{-1})$]. Minchev et al. (2007) find $\Omega_b = (1.87 \pm 0.04) \Theta_0/R_0$ ($51.5 \pm 1.5 \text{ km s}^{-1} \text{ kpc}^{-1}$). Chakrabarty (2007) and others argue that spiral arm perturbations need to be included, finding $R_0/R_{CR} \simeq 2.1 \pm 0.1$ and $\Omega_b \simeq 57.5 \pm 5 \text{ km s}^{-1} \text{ kpc}^{-1}$. The latest analysis of the Hercules stream by Antoja et al. (2014) gives $R_0/R_{CR} \simeq (1.83 \pm 0.02)$, $\Omega_b \simeq 53 \pm 0.5 \text{ km s}^{-1} \text{ kpc}^{-1}$, and $R_{CR} = 4.49 \pm 0.05 \text{ kpc}$ when rescaled to $(R_0, \Theta_0) = (8.2 \text{ kpc}, 238 \text{ km s}^{-1})$. This is the current most precise measurement but is model dependent; it would place corotation just inside the thin long bar and clearly within the superthin bar. It is just compatible with all the uncertainties; alternatively it may suggest that the Hercules stream has a different origin than the outer Lindblad resonance.

Considering all these determinations and the systematic uncertainties, we finally adopt a range of $R_{CR} = 4.5\text{--}7 \text{ kpc}$, or $\Omega_b \simeq 43 \pm 9 \text{ km s}^{-1} \text{ kpc}^{-1}$ for our best estimated $(R_0, \Theta_0) = (8.2 \text{ kpc}, 238 \text{ km s}^{-1})$. More accurate dynamical modeling of a wider set of stellar kinematical data, in particular from *Gaia*, is expected to narrow down this rather wide range in the coming years (Hunt & Kawata 2014).

5. STELLAR DISK

Our vantage point from within the Galaxy allows us to obtain vast amounts of unique information about galactic processes but this detail comes at a price. The Solar System falls between two spiral arms (**Figure 11**) at a small vertical distance from the Galactic Plane (Section 3.3). The

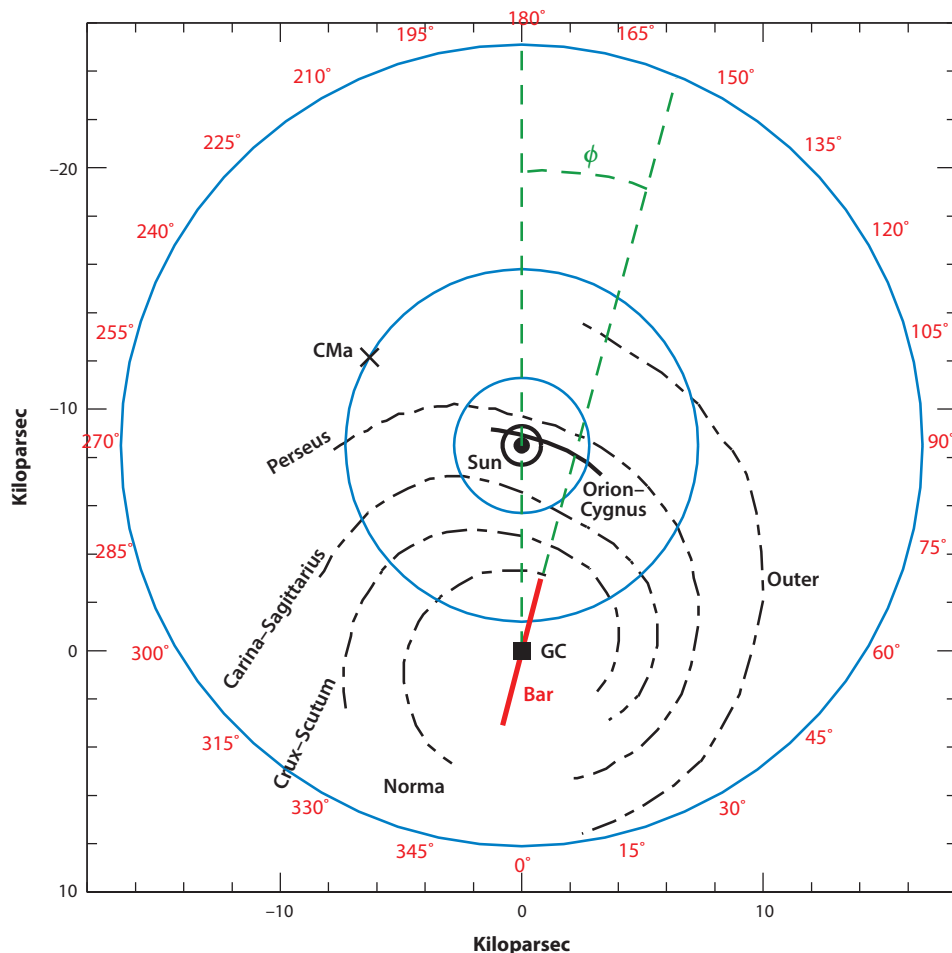


Figure 11

Plan elevation of the Galactic disk centered on the Sun's position showing the orientation and location of the main spiral arms. The numbered outer circle defines galactic longitude (ℓ). The Canis Major (CMa) overdensity is in the same general direction as the maximum disk warp. Adapted from Momany et al. (2006) with permission. Abbreviation: GC, Galactic Center.

thinness of the disk gives a fairly unobstructed view of the stellar halo and the outer bulge. But deprojecting the extended disk remains fraught with difficulty because of source confusion and interstellar extinction. Our off-center position at the Solar Radius is a distinct advantage except that it complicates any attempt to learn about large-scale, nonaxisymmetries across the Galaxy. We now have a better understanding of the structure of the inner Galaxy (Section 4), but the outer disk remains largely mysterious (see Section 5.5 below).

Over the past decade, we have learned much about the Galactic stellar disk, but few parameters are known with any precision. The local surface density and the vertical density profile of the summed disk component (gas, stars, background dark matter) are known to high certainty (Section 5.4.1). But although photometric scale lengths are well established in external galaxies (Lange et al. 2015), the radial scale lengths and vertical scale heights of the Galactic thin and

thick disks are uncertain. Unlike for the inner Galactic bar/bulge region (Section 4), we are not able to present a fully consistent picture for the disk at this time, although the key parameters are discussed and values recommended. Major reviews of the stellar disk include those by Freeman & Bland-Hawthorn (2002), Ivezić et al. (2012), and Rix & Bovy (2013); the gaseous disk is discussed at length by Kalberla & Dedes (2008).

One of the most interesting developments is the recognition of a Galactic thick disk that is distinct from the dominant thin disk through its unique chemistry (e.g., Bensby 2014, Hawkins et al. 2015, Masseron & Gilmore 2015), in addition to its older age and higher elevation. Originally recognized by Gilmore & Reid (1983), such disks appear to be ubiquitous in the local Universe (Yoachim & Dalcanton 2006). In external galaxies, deep stellar photometry reveals that the thick and thin disks have approximately equal scale lengths (e.g., Comerón et al. 2012). Whether these old red disks have a distinct formation history or have continuous properties with the old thin disk is unclear. Several authors have presented models in which the Galactic thick disk arises from a combination of stellar migration and/or flaring of the old disk stars, such that its history is tied to the formation of the thin disk even though its mean metallicity may be different (e.g., Schönrich & Binney 2009, Loebman et al. 2011, Minchev et al. 2015). In view of the distinct chemical signature of the thick disk, it is worthwhile to quantify its properties separately from the thin disk regardless of its origins.

5.1. Stellar Photometry

Early studies of the Galaxy would fit simple models to the projected star counts in a given optical or IR band (e.g., Bahcall & Soneira 1980). Without distance information, these authors found that a variety of models fit the data (including many combinations of two exponential functions) due to degeneracies between structural parameters. Historically, fits to star counts with vertical distance z have used a variety of functions but, today, the exponential function is widely used to match both disk photometry (Patterson 1940) and the peaked star counts close to the plane (Wainscoat et al. 1989).

By the end of the decade, we can expect accurate distances for millions of stars from the ESA *Gaia* survey. But for now, we are dependent on photometric parallaxes for determining stellar distances, which have a long history in their application to Milky Way structure (Gilmore & Reid 1983, Kuijken & Gilmore 1989, Chen et al. 2001). The term parallax echoes the use of nearby bright stars with established trigonometric parallaxes to calibrate the absolute magnitude–distance relation (e.g., Eggen 1951). (The term spectroscopic parallax refers to the spectral classification used to determine the absolute magnitude, rather than photometric colors.)

5.1.1. Scale heights. All photometric studies find an exponential scale height $z^{\dagger} = 220\text{--}450$ pc for the dominant old thin disk at the Sun’s location. The low extreme comes from multiband optical studies (e.g., Ojha 2001) that include stellar populations with a wide range of (especially younger) ages. These surveys suffer from various biases that tend to suppress the scale height (see below). The upper extreme is from early M dwarf studies in which confusion with halo M giants can lead to overestimates of the scale height (Reid 1993, Gould et al. 1996). M dwarfs, which account for roughly half of all stars in the Solar Neighborhood (Section 5.4.3), trace the underlying total stellar mass. The much larger M star survey by Jurić et al. (2008), discussed below, finds $z^{\dagger} \approx 300$ pc (to within 20%) after various biases are accounted for. This mid-range value is largely unchanged since Schmidt’s early determination (Schmidt 1963).

An improvement is to use two or more well-calibrated optical bands to compare the magnitude counts in different color bins. This led to Gilmore & Reid’s identification of the thick disk after

constructing the V and I luminosity functions for stars at or above the main-sequence turnoff (MSTO) at different distances from the plane and by ruling out biases due to interstellar extinction or metallicity gradients perpendicular to the disk. This classic study observed 12,500 stars toward the South Galactic Pole brighter than $I = 18$ and provided the first reliable stellar densities vertical to the Galactic Plane; their density profile continues to compare well with modern derivations (Section 5.4.1). They estimated $z^{\dagger} \approx 300$ pc in line with modern estimates, and $z^{\text{T}} \sim 1,450$ pc, somewhat higher than what is believed today.

After 2000, the quality and angular extent of photometric data from wide-field CCDs improved dramatically (e.g., Finlator et al. 2000). The internal accuracies of the multiband data led to improved estimates of photometric parallax and metallicity (robust in the range of $-2 < [\text{Fe}/\text{H}] < 0$) in wide-field surveys (see Ivezić et al. 2012). Notably, Siegel et al. (2002) observed select Kapteyn fields to derive photometric distances for 130,000 stars. They stressed the need to correct for unresolved multiplicities (of order 50%); otherwise, stellar distances (and therefore scale heights) are underestimated. The lower scale height estimates in the past are likely to have been underestimated for this reason. Even for old stars, there is some scale height variation among dwarfs: 280–300 pc for early-type dwarfs ($5.8 < M_R < 6.8$) rising to 350 pc for late-type dwarfs ($8.8 < M_R < 10.2$). When averaging over old dwarfs, before and after the correction, they obtain $z^{\dagger} \approx 290$ pc and $z^{\dagger} \approx 350$ pc, respectively; for the thick disk, they find $z^{\text{T}} = 700\text{--}1,000$ pc and $z^{\text{T}} = 900\text{--}1,200$ pc, respectively. (These are derived from exponential models; sech^2 fits lead to 10% smaller values after correction for the factor of two difference in scale height between the exponential and sech^2 functions.)

For our subsequent disk analysis, we focus on the SDSS *ugriz* northern sky survey with its excellent photometric quality (~ 0.02 mag). With photometric data for 48 million stars over $6,500 \text{ deg}^2$, this data set is the largest to date with precise color-magnitude versus metallicity relations made possible using cluster calibrations across the sky (Finlator et al. 2000, Chen et al. 2001). This survey gave rise to three major studies based on photometric parallax (Jurić et al. 2008), photometric metallicities (Ivezić et al. 2008), and kinematics (Bond et al. 2010) discussed in the next two sections.

Jurić et al. (2008) exploit the faint magnitude limit ($r \sim 22$ mag) of the SDSS survey and target two groups of M dwarfs: a late M group with $1.0 < r-i < 1.4$ and an early M/late K group with $0.65 < r-i < 1.0$. The late M group is favored because it is less sensitive to the halo population and to local substructure. At the Solar Circle, their formal model fits for both disk components are $z^{\dagger} \approx 245$ pc and $z^{\text{T}} \approx 740$ pc, respectively, before correction for multiplicity and closer to $z^{\dagger} \approx 300$ pc and $z^{\text{T}} \approx 900$ pc, respectively, after correction, both with 20% uncertainty. These constitute the most reliable values to date because of the SDSS coverage in galactic longitude and improved photometric distances over the required physical scales. Although the SDSS and 2MASS surveys are widely used in star count analyses, neither survey is ideal for determining the properties of the thick and thin disks simultaneously. Rather than cross-matching sources common to both catalogs (e.g., Finlator et al. 2000), future studies will need to combine both surveys in order to provide better input catalogs (Robin et al. 2014).

Although the thick disk was originally identified through stellar photometry, decompositions based on star counts are subject to degeneracies (Section 5.1.3). We include a limited discussion of the photometric estimates because of the historical context and because the thin disk values are broadly correct. But we stress that the thick and thin disk components are better separated through their distinct stellar chemistry. Numerous studies (Section 5.2) exploit either stellar abundances based on multiband photometry (large samples, large measurement errors) or spectroscopy (smaller samples, smaller errors).

5.1.2. Scale lengths. Although vertical scale heights are well determined at optical and IR wave bands due to the low extinction toward the poles, this is not true of disk radial scale lengths. We have analyzed 130 refereed papers on disk parameters, with scale lengths ranging from 1.8 to 6.0 kpc. In order to combat the effects of extinction, for observations that preceded the SDSS survey, the IR point source measurements are the most reliable because they tell a consistent story. This is particularly true for studies that target a broad extent in galactic longitude and observe in the anticenter direction to ensure they are less influenced by the presence of the central bar or by substructure. These include the Space Shuttle experiment (Kent et al. 1991), the Deep Near-Infrared Survey of the Southern Sky (DENIS; Ruphy et al. 1996) in the anticenter direction, COBE/FIRAS (Far Infrared Absolute Spectrophotometer; Freudenreich 1998, Drimmel & Spergel 2001), 2MASS (López-Corredoira et al. 2002, Cabrera-Lavers et al. 2005, Reylé et al. 2009), and GLIMPSE (Benjamin et al. 2005). A statistical analysis of the main papers (15 in all) on this topic leads to $R^t = 2.6 \pm 0.5$ kpc, which includes the highest value (3.9 kpc) from the GLIMPSE mid-IR survey. Our estimate drops to $R^t = 2.5 \pm 0.4$ kpc if we exclude the GLIMPSE study.

We have already stressed the importance of M stars. Jurić et al. (2008) determine $R^t \approx 2.6$ kpc (20% uncertainty) for the thin disk. Gould et al. (1996) and Zheng et al. (2001) used the *Hubble Space Telescope* to obtain scale lengths of $R^t = 3.0 \pm 0.4$ kpc and $R^t = 2.8 \pm 0.3$ kpc, respectively. All of these values are consistent with the IR measurements. A short scale length finds strong support from dynamical studies of the stellar kinematics in Section 5.4. From a study of monoabundance populations (MAPs), Bovy et al. (2012c) conclude that different populations give a scale length that is smoothly changing from 2 kpc in the inner disk (older populations) to 3 kpc or maybe even longer at $R = 12$ kpc (younger populations). However, the disk is dominated by old populations: A characteristic scale is meaningful when one considers the mass density profile of the disk. The IR photometric estimate of radial scale length is probably the most useful at the present time, although we recognize that an exponential decline in the mass distribution is a crude approximation (**Figure 10**). The thick disk scale length is discussed in the next section.

For the past thirty years, some have argued for a longer disk scale length when comparing the Galaxy, with its high mass and luminosity, with external galaxies (q.v. van der Kruit & Freeman 2011). The Galaxy and Mass Assembly survey (Driver et al. 2011) includes the largest bulge/disk decomposition survey to date using the *Viking K*-band imaging survey of 4,300 disk galaxies (Lange et al. 2015). This volume-limited survey has a high level of completeness to a redshift limit of $z < 0.06$ ($M_\star > 10^9 M_\odot$). Here only a few percent of galaxy disks exceed the Milky Way’s disk mass (Section 5.4.2), and their IR photometric scale lengths have a large spread (4 ± 2 kpc). The Galaxy’s high luminosity and small scale length may not be so unusual.

We highlight one spectacular result from the SDSS survey. The team was able to extract tomographic slices through the Galaxy vertical to the plane (e.g., **Figure 12**). **Figure 12** illustrates a problem with Galaxy model fits and goes some way to explaining the lack of convergence in disk parameters over three decades. Jurić et al. (2008) explicitly highlight important substructure across the Galaxy including the Virgo Overdensity and the Monoceros Ring (Newberg et al. 2002). Substructure is so prevalent that it is not possible to fit a smooth double exponential disk model in R and z to either the thick or thin disk without taking this component into account. This problem is well known for disk-halo fitting because the Sgr stream dominates so much of the halo.

5.1.3. Thick disk normalization. Several studies have tried to determine the local density normalization ($f_\rho = \rho^T / \rho^t$) of the thick disk compared with the thin disk with estimates ranging from 1% to 12% (e.g., Gilmore & Reid 1983, Siegel et al. 2002, Jurić et al. 2008). The large uncertainty in f_ρ is largely due to its degeneracy with the derived scale lengths for both components (Siegel

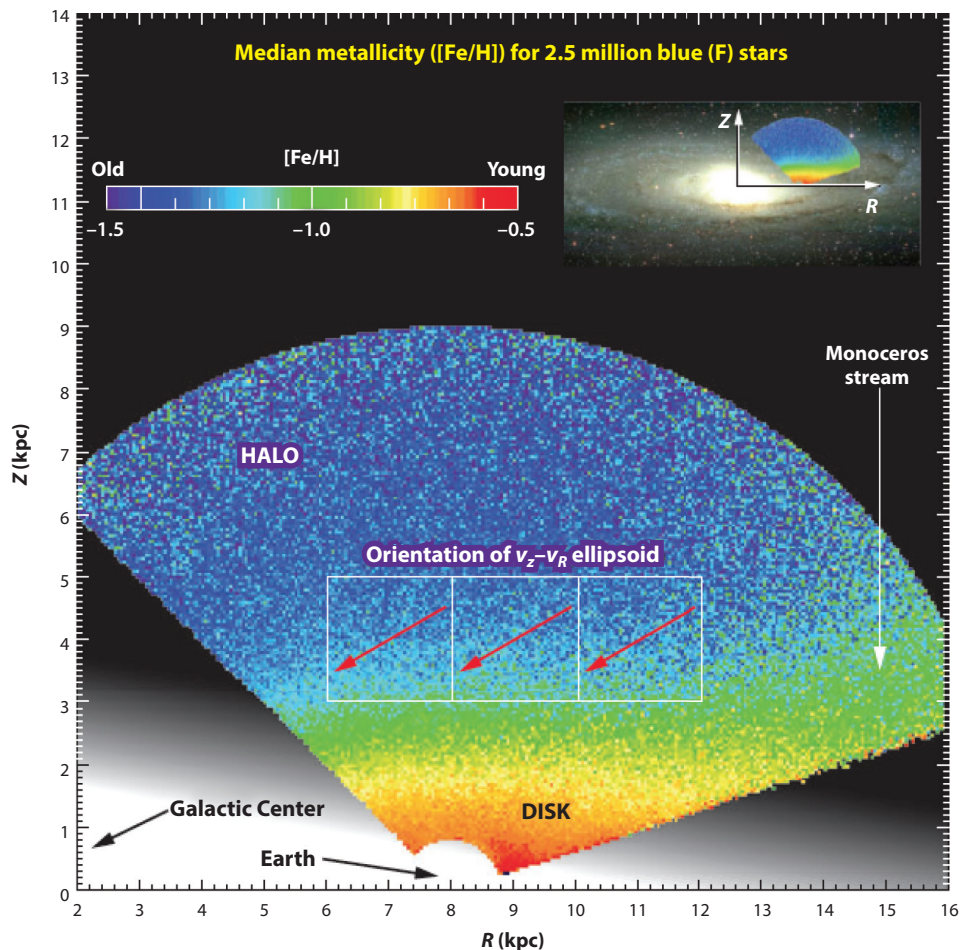


Figure 12

A tomographic slice showing the change in stellar metallicity through the Galaxy perpendicular to the Galactic Plane and passing through the Galactic Center and the Sun. The underlying stellar density is shown in half tone (Jurić et al. 2008). The dwarf star distances and metallicities are obtained from photometric parallax and photometric metallicities using the Sloan Digital Sky Survey (SDSS) *ugriz* data calibrated using globular clusters over a range of metallicities (Ivezić et al. 2008). The photometric metallicities are robust within the range $-2 < [\text{Fe}/\text{H}] < 0$. This projection highlights the difficulty of fitting simple composite models to the stellar disk, particularly in the outer reaches where the Monoceros stream and other substructures become apparent. The direction of the halo vertex deviation taken from Bond et al. (2010) is also shown. Adapted from Ivezić et al. (2012) with permission.

et al. 2002, Árnadóttir et al. 2009): Higher estimates of z^T are associated with lower estimates of f_ρ and vice versa. To aid comparison with most published results, we prefer this form for f_ρ rather than normalization to the total disk mass (e.g., Piffl et al. 2014a). We have analyzed all results from photometric surveys (25 in all) conducted since the discovery paper and arrive at $f_\rho = 4\% \pm 2\%$.

A detailed analysis of the degeneracy between disk parameters is given by Chen et al. (2001) for late-type dwarfs chosen from the SDSS survey in which the data are separated into two

z^{\dagger} : thin disk vertical scale length at R_0 , 300 ± 50 pc

z^{\dagger} : thick disk vertical scale length at R_0 , 900 ± 180 pc

f_{ρ} : thick/thin disk local density ratio at R_0 , $4\% \pm 2\%$

f_{Σ} : thick/thin disk surface density ratio at R_0 , $12\% \pm 4\%$

R^{\dagger} : thin disk radial scale length, 2.6 ± 0.5 kpc

R^{\dagger} : thick disk radial scale length, 2.0 ± 0.2 kpc

hemispheres. Our value of f_{ρ} is in line with their likelihood analysis (see their figure 9) for a thick disk scale height of $z^{\dagger} = 900 \pm 100$ kpc. It is also broadly consistent with dynamical fitting to the Solar Cylinder (e.g., $f_{\rho} \approx 6\% \pm 2\%$; Just & Jahreiß 2010).

The error is smaller when we compare the surface density of the thick and thin disks, i.e., $f_{\Sigma} = f_{\rho} z^{\dagger} / z^{\dagger}$. Here, we find $f_{\Sigma} = 12\% \pm 4\%$. Our analysis excludes all papers that do not fit simultaneously for the thin and thick disk. At this point, no separation is made on the basis of detailed stellar abundance information. A high thick disk local density ($f_{\rho} \approx 6\%$) is also found when spectroscopic abundances are used to define the high $[\alpha/\text{Fe}]$ population (Bovy et al. 2015), but this depends on how the abundance cut is made. A low value for f_{ρ} is in conflict with Jurić et al. (2008), who determine the thick disk to be more massive ($f_{\rho} \approx 12\%$) at the Solar Circle (cf. Fuhrmann 2008). Recent claims of a more massive thick disk may arise from the survey selection extending into the low $[\alpha/\text{Fe}]$ population (e.g., Snaith et al. 2014) or from the use of a tiny survey volume (e.g., Fuhrmann 2008).

5.2. Stellar Chemistry

5.2.1. Photometric metallicity. Ivezić et al. (2008) examined the vertical distribution in photometric metallicity of 2 million SDSS stars calibrated with SEGUE spectra of 60,000 F and G dwarfs ($0.2 < g - r < 0.6$). An additional refinement was to combine the Palomar Optical Sky Survey and the SDSS data to derive PMs (e.g., Munn et al. 2004). Here the tangential velocity accuracy for stars brighter than $g \sim 19$ is comparable with the RV accuracy of the SDSS spectroscopic survey (15 km s^{-1} for a star at 1 kpc; 100 km s^{-1} at 7 kpc). The aim was to look for the thin disk–thick disk transition at ~ 1 kpc, and the thick disk–halo transition at ~ 2.5 kpc, in metallicity and velocity. The SDSS team confirm earlier trends in declining metallicity and increasing lag at larger elevations (Figure 12) and find evidence for thick disk stars extending to $z > 5$ kpc. They could only discern a gradual transition in photometric metallicity and kinematics across the thin disk–thick disk divide, which is in conflict with the traditional two-component fit (cf. Bond et al. 2010). Although no kinematic modeling was conducted at this stage (see Section 5.3), the SDSS team find the data are more consistent with a gradual continuum from a thin young disk to an extended older disk. A better understanding of the thick disk versus thin disk separation had to wait for spectroscopic surveys (Section 5.2), providing both improved elemental abundances and 3D space velocities (Steinmetz et al. 2006, Allende Prieto et al. 2008).

5.2.2. Spectroscopic metallicity. In the past, some researchers have questioned the existence of a thick disk with discrete properties—chemistry, age, kinematics—beyond the obvious characteristic of physical extent (e.g., Norris & Ryan 1991). This is a fundamental question because it hinges on the formation and evolution of the major baryonic component of our Galaxy. In Figure 13, the stars of the thick disk are mostly older than those of the thin disk and have a distinct chemistry (Bensby et al. 2003, Haywood 2006, Schuster et al. 2006, Bensby 2014). It is recognized today that $[\alpha/\text{Fe}]$ is enhanced for the thick disk compared to the thin disk over a wide range in $[\text{Fe}/\text{H}]$, an effect that is easily seen in sufficiently high-resolution ($\mathcal{R} \gtrsim 20,000$) spectroscopic data (Fuhrmann 1998; Gratton et al. 2000; Prochaska et al. 2000; Reddy et al. 2003, 2006; Soubiran et al. 2003) and even possibly at $[\text{Fe}/\text{H}] \gtrsim 0$ (Hayden et al. 2015, Haywood et al. 2015, Kordopatis et al. 2015). Recent studies show that the earlier counter claims likely suffered from underestimating measurement errors (e.g., Nidever et al. 2014) or they incorrectly assumed that errors between measurements are uncorrelated (e.g., Schönrich et al. 2014).

The kinematic criteria often used to separate the disks inevitably lead to small stellar samples compared to photometric surveys. The Bensby studies exploit the Geneva-Copenhagen Survey

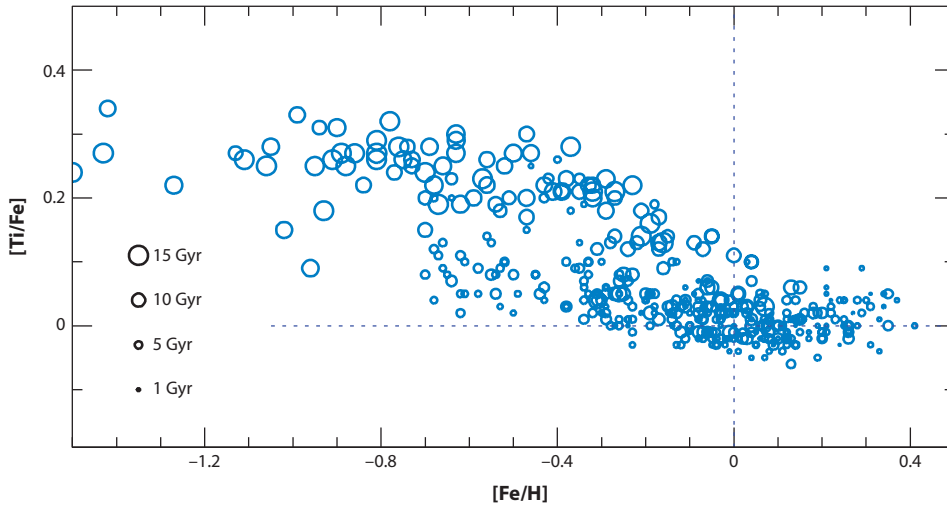


Figure 13

[Ti/Fe] versus [Fe/H] for 700 F and G dwarf stars with age determinations showing a uniformly old population, thick disk with enhanced $[\alpha/\text{Fe}]$ abundances and a dominant thin disk population with a spread of ages. The size of the circle scales with age, and the stars have uncertainties on the order of about a gigayear; the metallicity uncertainties are smaller than 0.1 dex. Note how the two-component disk appears to exist at the solar metallicity extreme. Adapted from Bensby (2014) with permission.

(GCS) of 16,000 nearby dwarfs with full 3D space velocities, and ages and metallicities from Strömgren photometry (Nordström et al. 2004). But a clean local separation is hampered in part by extensive kinematic substructure over the local volume: The Hercules stream, for example, comprises both thick and thin disk stars (Bensby et al. 2007). But even without kinematic separation, the chemical signature of two distinct populations is evident (Adibekyan et al. 2012, Haywood et al. 2015).

A new signature has emerged from the APOGEE survey that may help to separate the disks further. Masseron & Gilmore (2015) show that C/N is enhanced in the thick disk compared to the thin disk, presumably owing to the effects of dredge-up observed in old turnoff dwarfs and giants. The associated age (and mass) for the oldest stars is broadly consistent with **Figure 13**. At the present time, it is not possible to separate the thick disk from the oldest thin disk stars through age-dating, assuming such a distinction even exists. The detailed chemistry of the thick disk may provide a better discriminator than the use of phase space (\mathbf{x}, \mathbf{v}) and be the defining characteristic of this component. Kinematic criteria always leads to some overlap. Hawkins et al. (2015) emphasize that a more expanded chemical (\mathcal{C}) space may be called for to ensure that the thick disk can be separated from both the thin disk and the lower halo, i.e., $\mathcal{C}([\alpha/\text{Fe}], [\text{C}+\text{N}/\text{Fe}], [\text{Al}/\text{Fe}], [\text{Mg}/\text{Mn}])$. A high-quality “chemical tag” defined in this way requires both optical and IR data at high spectroscopic resolution.

The use of chemistry to define thick disk stars now gives a different perspective on defining the relative density and scales of the two disks. Bensby et al. (2010) found that the bimodal $[\alpha/\text{Fe}]$ distribution continues inside of the Solar Circle, in contrast to the outer disk where the enhanced $[\alpha/\text{Fe}]$ population is not detected, which led Bensby et al. (2011) to infer a shorter scale length for the thick disk. By dividing SEGUE dwarfs spectroscopically into MAPs, Bovy et al. (2012c) note the transition between a short scale length—e.g., “high $[\alpha/\text{Fe}]$, low $[\text{Fe}/\text{H}]$ ” population, with a scale height up to 1,000 pc—and a longer scale length—e.g., “low $[\alpha/\text{Fe}]$, high $[\text{Fe}/\text{H}]$ ”

population, with a scale height below 400 pc. But the more extensive APOGEE survey of 70,000 red giants reveals that the picture is more complicated (Bovy et al. 2015, Hayden et al. 2015). Looking outward, both tracks are evident, except the high $[\alpha/\text{Fe}]$ sequence disappears beyond 11 kpc, whereas the low sequence is seen to at least 15 kpc.

Toward the inner disk, the high $[\alpha/\text{Fe}]$ track dominates over the low $[\alpha/\text{Fe}]$ sequence even though an increasing fraction of stars pile up toward higher metallicities due to the thin disk abundance gradient. Over the innermost disk, the thick disk and bulge are more difficult to disentangle because they share kinematic and abundance characteristics, as observed in red giants (Alves-Brito et al. 2010, Ryde et al. 2010, Gonzalez et al. 2011b, Hill et al. 2011) and microlensed dwarf stars (Bensby et al. 2009, 2013).

In summary, estimates for the thick disk scale length range from 1.8 to 4.9 kpc (12 papers) (e.g., Larsen & Humphreys 2003, Cheng et al. 2012), but few of these make a distinction based on chemistry. There exists now some convergence on R^T from surveys over very different volumes and sample sizes. Bensby et al. (2011) estimate an exponential scale length of 2 kpc ($\approx 10\%$ accuracy), in good agreement with the high- $[\alpha/\text{Fe}]$ MAPs from SEGUE (Bovy et al. 2012c), although Cheng et al. (2012) measure $R^T \approx 1.8$ kpc using 7,000 MSTO dwarfs from the same survey, albeit with larger errors. More recently, Bovy et al. (2015) find $R^T = 2.2 \pm 0.2$ kpc for high- $[\alpha/\text{Fe}]$ MAPs using APOGEE RCGs. Overall, we conclude that $R^T = 2.0 \pm 0.2$ kpc in which the thick disk is defined in terms of the high- $[\alpha/\text{Fe}]$ population. When extrapolated to the GC, the ratios f_ρ and f_Σ are 2.6 times higher than the local values.

5.3. Stellar Kinematics

The large photometric surveys, with their photometric distance estimates, provide us with initial estimates of the structural parameters for each of the major Galactic components. Over a decade ago, the community recognized that progress would require kinematic information for many stars over large swaths of the sky. Since that time, there has been extensive investment in wide-field stellar kinematic surveys, some of which are still in progress: GCS (Nordström et al. 2004), SEGUE (Yanny et al. 2009), Radial Velocity Experiment (RAVE; Steinmetz et al. 2006), APOGEE (Allende Prieto et al. 2008), LAMOST Experiment for Galactic Understanding and Exploration (LEGUE; Deng et al. 2012), *Gaia* ESO Survey (GES; Gilmore et al. 2012), and Galactic Archaeology with Hermes (GALAH; De Silva et al. 2015). These surveys look at different parts of the sky and go to different depths. Some have been rendered dynamically as 3D visualizations at the following website: <https://www.rave-survey.org/project/gallery/movies>. The GCS survey covers the full sky but is confined to the Solar Neighborhood; the SEGUE, RAVE, and APOGEE surveys penetrate deeper into the Galaxy than earlier stellar surveys. By far the largest of the new surveys, the ESA *Gaia* mission will obtain both spectra and astrometric information for up to ~ 150 million stars (de Bruijne et al. 2015). By the end of the decade, we can expect to have RVs and stellar parameters for millions of stars, for dwarfs out to ~ 1 kpc, and for giants out to the halo.

Here we review the main insights to emerge from these surveys. We make a distinction between dynamical models of the Galaxy (e.g., Rix & Bovy 2013; see Section 6) and models that fit to the separate Galactic components without dynamical consistency (e.g., Catena & Ullio 2010), which we refer to as kinematic models. In a kinematic model, one specifies the stellar motions independently at each spatial location, and the gravitational field in which the stars move plays no role. In a dynamical model, the spatial density distribution of stars and their kinematics are self-consistently linked by the potential, under the assumption that the system is in steady state.

When fitting a model, there are important considerations. First, all surveys are defined by their selection function (e.g., magnitude, velocity, coordinates), and any biases must be accommodated

by the analysis. Secondly, it is important to make a stab at including a plausible star-formation history in the analysis (e.g., Schönrich & Binney 2009). Making more stars in the past places more old stars at higher galactic latitudes today and, therefore, at higher kinematic dispersion through the age-velocity dispersion relation (AVR) (e.g., Aumer & Binney 2009). But this adds to the complexity because (a) we are introducing new variables into an already crowded field; and (b) degeneracy exists between different parameters, e.g., the SFR and the slope of the IMF (Haywood et al. 1997).

An increasingly popular approach to fitting is to use Bayesian optimization over a broad set of free parameters (e.g., Catena & Ullio 2010). As a worked example, in the **Supplemental Text** (follow the **Supplemental Material** link from the Annual Reviews home page at <http://www.annualreviews.org>), we summarize the GALAXIA framework for fitting up to 20 disk parameters—this code is freely available at <http://sourceforge.net/p/galaxia/wiki/Home/>. The approach is theoretically simple and allows for useful constraints on local kinematic properties. The framework incorporates a constant SFR and a 3D Galactic dust model. Uniquely, it is designed to correct for an arbitrary survey selection function and can be used to fit data to analytic functions or numerical simulations (Sharma et al. 2011).

How Sharma et al. (2014) apply the method to the RAVE and GCS surveys by assuming the structural form of the disk $f(r)$ and then attempting to fit for $f(v|r)$ from the surveys is described in the **Supplemental Text**. They use only sky position and velocity for each star as these are the most accurate measurables. No distance information is supplied other than what is implicit in the model fitting. They fit both the Gaussian DF and the dynamically motivated Shu DF (Sharma & Bland-Hawthorn 2013); the latter performs better because it allows for asymmetric velocity distributions (relative to the Sun) due to noncircular motions experienced by most stars.

Groups that use Bayesian optimization (Bovy & Tremaine 2012, Sharma et al. 2014) typically fit for (a) the AVR (see below); (b) the radial scale lengths ($R_{\sigma,R}^t$, $R_{\sigma,R}^T$) of the velocity dispersion profile; (c) the mean stellar motion \bar{v}_ϕ with vertical height z ; and (d) the solar motion (\mathbf{v}_\odot). The RAVE team finds that earlier estimates of the LSR are unreliable if they neglect the vertical dependence of the mean azimuthal motion for a given population. Ultimately, even after this correction, global kinematic measures like Θ_0 are expected to have systematic uncertainties because of the initial assumption on $f(r)$ and the lack of dynamical consistency. We return to these measures in the next section.

5.3.1. Age-velocity dispersion relation. It is well established that the velocity dispersion of a disk stellar population $\sigma(R, \phi, z)$ increases with age (Strömberg 1925, Wielen 1977). Disks heat because a cold thin disk occupies a small fraction of phase space, and fluctuations in the gravitational field cause stars to diffuse through phase space to regions of lower phase-space density. These effects are very difficult to model reliably through numerical simulations. For the thin disk, the AVR is sometimes approximated as a power law in cosmic time (e.g., Aumer & Binney 2009) such that

$$\sigma(R, \phi, z) = \sigma_0(R, \phi, z) \left(\frac{\tau + \tau_{\min}}{\tau_{\max} + \tau_{\min}} \right)^{\beta_{R,\phi,z}}, \quad (1)$$

where $(\tau_{\min}, \tau_{\max})$ are priors. The power-law indices ($\beta_R, \beta_\phi, \beta_z$) provide important information on disk heating parameters (Binney 2013, Sellwood 2013); a summary of estimates is given in **Table 4**. The widely used value of $\beta = 1/3$ dates back to the cloud scattering model of Spitzer & Schwarzschild (1953). Though useful, this form is not universally accepted (e.g., Freeman 2001, Quillen & Garnett 2001); it makes no allowance for the thick disk, which must be treated separately. From existing data, it is very difficult to distinguish a continually rising AVR from one that steps or saturates at old ages (Aumer & Binney 2009, Casagrande et al. 2011). Some groups


 **Supplemental Material**

Table 4 Comparison of measured or quoted β indices in the age–velocity dispersion relation from stellar kinematic surveys

Reference	Survey	β_R	β_ϕ	β_z
Nordström et al. (2004)	GCS	0.31 ± 0.05	0.34 ± 0.05	0.47 ± 0.05
Seabroke & Gilmore (2007)	GCS	–	–	0.48 ± 0.26
Holmberg et al. (2007)	GCS	0.38	0.38	0.54
Holmberg et al. (2009)	<i>Hipparcos</i> , GCS	0.39	0.40	0.53
Aumer & Binney (2009)	<i>Hipparcos</i> , GCS	0.31	0.43	0.45
	<i>Hipparcos</i>	–	–	0.38
Just & Jahreiß (2010)				
Sharma et al. (2014)	GCS	0.20 ± 0.02	0.27 ± 0.02	0.36 ± 0.02
Sharma et al. (2014)	RAVE	0.19 ± 0.02	–	0.3–0.4
Sanders & Binney (2015)	SEGUE	0.33	–	0.4

Note: The quoted errors are statistical and do not include systematic errors that are typically larger. Dashes, –, indicate no data.

attempt to fit for age-metallicity trends in the thin disk, but such fits are less instructive at the present time (q.v. Freeman & Bland-Hawthorn 2002), although ultimately this information will need to be accommodated in a successful model (Sanders & Binney 2015).

5.3.2. Velocity dispersion profile. Pasetto et al. (2012) used the RAVE survey to learn about the variation of velocity dispersion in the (R, z) plane. They used singular value decomposition to compute the moments of the velocity distribution. As expected, the thin disk stars follow near-circular, corotational orbits with a low velocity dispersion (e.g., Edvardsson et al. 1993, Reddy et al. 2003). The velocity dispersion falls as a function of distance R from the GC, consistent with theoretical expectation (Cuddeford & Amendt 1992).

In an exponential disk, the stellar dispersion declines radially with the disk surface density Σ^i and scale height z^i as $\sigma^i(R) \propto \sqrt{z^i(R) \Sigma^i(R)}$. Sharma et al. (2014) combined Equation 1 with an exponential factor in radius (cf. van der Kruit 1986) in order to determine the radial scale lengths ($R_{\sigma,R}^i$, $R_{\sigma,R}^T$) of the dispersion profile (e.g., Lewis & Freeman 1989). For an isothermal disk, R_σ is expected to be roughly twice the disk density scale length (Bottema 1993). The RAVE study confirms that the dispersion profile declines with radius, yielding estimates of $R_{\sigma,R}^i \sim 14$ kpc and $R_{\sigma,R}^T \sim 7.5$ kpc. The thick disk value is in good agreement with a full dynamical analysis, which we return to below. The thin disk is insufficiently constrained in the RAVE survey because the elevated sightlines in latitude do not extend far enough in radius and are susceptible to vertical dispersion gradients (cf. Piffl et al. 2014a, Sanders & Binney 2015).

Bovy et al. (2012b) divided up the SEGUE survey into MAPs and argued that these constituted quasi-isothermal populations. (We refer the reader to Sanders & Binney 2015 for a different perspective on how to treat chemical information in fitting Galactic models.) Bovy found no break in vertical dispersion between the old thin and thick disk and suggested that the thick disk is a continuation of the thin disk rather than a separate entity (cf. Schönrich & Binney 2009). In contrast, kinematic and dynamic studies—which include a star-formation history and an AVR explicitly for the thin disk—do tend to find a break in the vertical stellar dispersion (e.g., Table 5). Future studies that exploit improved stellar ages and chemistry will be needed to resolve this issue.

Table 5 Parameter estimates from Galactic dynamical models with disk fitting

Parameter	M11	B12 ^a	BR13 ^b	P14	SB15	BP15
Kinematic data	Hi	GCS	SEGUE	RAVE	SEGUE	RAVE
R_0 (kpc)	8.3	[8.0–8.4]	[8.0]	[8.3]	[8.0]	[8.3]
Θ_0 (km s ⁻¹)	239	[220–241]	218	[240]	[220]	[240]
M_{200} (M _⊙)	1.3×10^{12}	–	–	1.3×10^{12}	–	1.4×10^{12}
M_{cold} (M _⊙) ^c	7.1×10^{10}	–	6.8×10^{10}	5.6×10^{10}	–	6.2×10^{10}
$f_{\text{cold}}^{\text{d}}$ (%)	4.9	–	–	4.3	–	4.2
R^{t} (kpc)	3.0	2.7–3.1	2.2	2.7 =	2.3	3.7 =
R^{T} (kpc)	3.3	2.1–3.6	–	2.7 =	3.5	3.7 =
$R_{\sigma_R}^{\text{t}}$ (kpc) ^e	–	3.6–20	–	9.0 =	7.8 =	$2 \times R_{\text{d}} =$
$R_{\sigma_z}^{\text{t}}$ (kpc)	–	–	–	9.0 =	7.8 =	$2 \times R_{\text{d}} =$
$R_{\sigma_R}^{\text{T}}$ (kpc)	–	–	–	13	6.2 =	11.6
$R_{\sigma_z}^{\text{T}}$ (kpc)	–	–	–	4.2	6.2 =	5.0
σ_R^{t} (km s ⁻¹)	–	40–42	–	34	48	35
σ_z^{t} (km s ⁻¹)	–	20–27	–	25	31	26
σ_R^{T} (km s ⁻¹)	–	25–28	–	51	51	53
σ_z^{T} (km s ⁻¹)	–	33–65	–	49	51	53

^aThe thin and thick disks are treated separately for two distinct potentials and parameter sets (b, c).

^b M_{cold} has been rescaled to $R_0 = 8.3$ kpc for ease of comparison with other results.

^c M_{cold} includes the stellar disk, the bulge, and the cold gas disk; the M11 total stellar mass has been corrected for a gas mass of 0.7×10^{10} M_⊙ in line with the other references, except that BP15 assumes a gas mass of 1.7×10^{10} M_⊙. M_{200} assumes a spherical halo ($q = 1$) with $q < 1$ leading to higher values; M_{cold} does not include the Galactic corona; thin disk dispersions are evaluated at 10 Gyr.

^d f_{cold} is the ratio of M_{cold} to the total galaxy mass.

^e R_{σ} is a parameter that sets the scale of the outward radial decline in velocity dispersion within the disk.

Note: All models (except M11) apply Bayesian fitting of action integrals. Brackets, [...], indicate a prior; dashes, –, indicate no data; equals sign, =, indicates values locked in fitting for R_{d} .

References: M11, McMillan (2011); B12, Binney (2012); BR13, Bovy & Rix (2013); P14, Piffl et al (2014a); SB15, Sanders & Binney (2015); BP15, Binney & Piffl (2015).

5.3.3. Solar motion and local standard of rest. Delhaye (1965) determined the solar motion \mathbf{v}_{\odot} with respect to the LSR defined in the reference frame of a circular orbit that passes through the Sun’s position today. Formally, for a coordinate system based at the Sun, where the \mathbf{i} unit vector points toward the GC, \mathbf{j} is in the direction of rotation, and \mathbf{k} is upward from the disk, $\mathbf{v}_{\odot} = U_{\odot}\mathbf{i} + V_{\odot}\mathbf{j} + W_{\odot}\mathbf{k}$. Delhaye studied different spectral classes and luminosity groups and arrived at $\mathbf{v}_{\odot} \approx (9, 12, 7)$ km s⁻¹, which is very respectable by modern standards.

The random stellar motions of a given population is a strong function of their mean age, color, metallicity, and scale height. Care must be taken to account for the asymmetric drift of stellar populations in taking the limit to the zero-dispersion LSR orbit. Using Strömberg’s relation, Dehnen & Binney (1998) measured $(U_{\odot}, V_{\odot}, W_{\odot}) = (10.0, 5.2, 7.2)$ km s⁻¹ from the *Hipparcos* survey, which for two ordinates are in excellent agreement with Delhaye’s early estimates. V_{\odot} was later revised upward close to the original value (Binney 2010, Schönrich et al. 2010); the latter paper showed that Strömberg’s linear asymmetric drift relation is invalidated by the metallicity gradient in the disk. Our values for \mathbf{v}_{\odot} in the margin note are averaged over most estimates since Delhaye’s original estimate. We have removed extreme outliers and ignored early values from any researcher who revised these at a later stage using a similar method. Thus, the Sun is moving

U_{\odot} : solar motion in U , $10.0 \pm 1 \text{ km s}^{-1}$

V_{\odot} : solar motion in V , $11.0 \pm 2 \text{ km s}^{-1}$

W_{\odot} : solar motion in W , $7.0 \pm 0.5 \text{ km s}^{-1}$

$|\mathbf{v}_{\odot}|$: solar vector motion, $15.5 \pm 3 \text{ km s}^{-1}$

$|\mathbf{v}_{\text{str}}|$: local standard of rest streaming motion, $0^{+15} \text{ km s}^{-1}$

inward toward the GC, upward toward the North Galactic Pole and, given z_0 , away from the plane.

Although (U_{\odot}, W_{\odot}) have converged on Delhaye’s original values within the errors (see the margin note), some uncertainty surrounds V_{\odot} when considered across the APOGEE, RAVE, and LEGUE surveys (Bovy et al. 2012a, Sharma et al. 2014, Tian et al. 2015). One reason for this may arise from local kinematic substructure or any systematic streaming motion \mathbf{v}_{str} in the Sun’s vicinity (Dehnen 2000, Siebert et al. 2011, Williams et al. 2013, Antoja et al. 2014). A local spiral arm density wave, for example, can impose kinematic fluctuations on the order of 10 km s^{-1} (Siebert et al. 2012). In addition, because the corotation radius of the Galactic bar may be as close as $\sim 2 \text{ kpc}$ inward from the Sun (Section 4.4), systematic streaming velocities may exist in the local Galactic disk due to perturbations from the bar and adjacent spiral arms. These could cause deviations of the zero-dispersion LSR orbit from the average circular velocity at R_0 , defined as the angular rotation velocity of a “fictitious” circular orbit in the axisymmetrically averaged gravitational potential, the so-called rotational standard of rest (RSR; see Shuter 1982, Bovy et al. 2012a). Analyzing two mostly independent samples of stars from APOGEE, RAVE, and GCS, Bovy et al. (2015) modeled the disk velocity field over $\sim 3\text{--}4\text{-kpc}$ scales and found such effects, with an implied tangential LSR streaming velocity of $14 \pm 3 \text{ km s}^{-1}$ relative to the RSR. However, Sharma et al. (2014) find little difference in V_{\odot} between the local GCS survey and the RAVE data, which extends to $\sim 2 \text{ kpc}$, and Reid et al. (2014), when fitting their maser velocities with a circular orbit velocity field, find no evidence for a deviation of the globally fitted V_{\odot} from the locally determined value. Globally determined values of U_{\odot} (Bovy et al. 2012a, Reid et al. 2014) agree well within errors with the locally determined $U_{\odot} = 10 \pm 1 \text{ km s}^{-1}$. Here, we adopt $|\mathbf{v}_{\text{str}}| = 0^{+15} \text{ km s}^{-1}$ because we cannot establish clear agreement on the magnitude of the streaming motion at the present time. Future studies are anticipated to compare the impending *Gaia* data with models including the central bar and spiral density waves in view of understanding both the random and streaming motions in the disk.

5.3.4. Vertex deviation. Binney et al. (2014) revisit the RAVE data but include distance estimates from Burnett et al. (2011). These were not employed by Sharma et al. (2014) because RAVE distances are susceptible to uncertainties in PMs and stellar parameters, e.g., $\log g$ (Zwitter et al. 2010, Anguiano et al. 2015). After excluding young stars, Binney finds that the velocity dispersion for a given stellar population increases as one moves vertically in z from the plane (cf. Smith et al. 2009). Furthermore, at any location in (R, z) , the velocity ellipsoid’s long axis (vertex deviation) points toward the GC (see **Figure 12**), indicating that the radial and vertical motions of stars are intimately coupled (cf. Siebert et al. 2008, Bond et al. 2010). This important result demonstrates that the stellar motions in R and z are entwined through the Galactic potential.

5.4. Stellar Dynamics

Kinematic models offer greater freedom than physics really allows. This can lead to systematic errors in parameter estimation, which typically swamp the statistical errors in the optimization scheme. The way forward is to consider dynamical models such that the spatial density distribution of stars and their kinematics are linked by the gravitational potential Φ , under the assumption that the system is in steady state. At present, dynamical models are used to estimate a subset of parameters explored by kinematic methods (see **Table 5**). Although there has been good progress in recent years, with the first signs of dynamical self-consistency beginning to emerge, there is no fully consistent framework at the present time. We refer the reader to Rix & Bovy (2013, their section 6) for a useful summary of the dynamical methods on offer.

Early methods that operate locally or in annular bins (e.g., Bienayme et al. 1987, Just & Jahreiß 2010) have given way to holistic treatments over one or more dynamical components of the Galaxy (e.g., Piffl et al. 2014a, Sanders & Binney 2015). Dynamical models assume an equilibrium figure such that the phase-space density of stars $f(\mathbf{x}, \mathbf{v})$ links only to the phase-space coordinates through the constants of motion (Jean’s theorem).

Binney (2010, 2012) has argued that action integrals (\mathbf{J}) are ideal for building dynamical models because they are adiabatic invariants. The most convenient action integrals are (a) L_z , the approximate symmetry axis of the Galaxy’s angular momentum, (b) J_z , to describe the action of a star perpendicular to the plane, and (c) J_R , to describe the radial action of the star. The DF at any point in the Galaxy has the form $f(L_z, J_z, J_R)$. Φ is derived through an iterative process starting with an initial guess Φ_i to get to the density $\rho_i = \int f d^3v$ integrated over the phase-space volume v . Poisson’s equation is used to compute an updated Φ_{i+1} , and the process is repeated until convergence is achieved. The numerical procedures are nontrivial and computationally expensive but entirely feasible for surveys involving thousands of stars (Binney & McMillan 2011).

Of the few action integral studies of the disk to date, we highlight the work of Binney (2012) using GCS, Bovy & Rix (2013) and Sanders & Binney (2015) using SEGUE, and Piffl et al. (2014a) and Binney & Piffl (2015) using RAVE. In **Table 5**, these studies attempt to arrive at unbiased parameter estimates through fitting the data with a consistent dynamical model. Binney (2012) introduced important new ideas in model fitting, including the use of the quasi-isothermal DFs to model the disk. But his focus on a very local sample led to the disk dispersions being underestimated due to the GCS bias toward younger stars. This work has been superseded by Piffl et al. (2014a), who determined the DF from the RAVE giants. The RAVE survey comprises roughly equal numbers of dwarfs and giants, most within about 2.5 kpc of the Sun, and is thus more representative of the extended disk (Sharma et al. 2011).

Bovy & Rix (2013) build on Binney (2012) using 16,300 G dwarfs from the SEGUE survey. They divide stars in the $[\alpha, \text{Fe}]$ abundance plane into MAPs: The more metal-rich MAPs trace the inner disk, whereas the metal-poor populations trace the disk beyond the Solar Circle. Their goal is to measure the Galactic disk’s mass profile by identifying a radius for each MAP where the modeling gives a tight (statistical) constraint on the local surface density. It is unclear whether (a) most MAPs can be treated as quasi-isothermal populations; and (b) the constraints at different radii from the MAPs are mutually consistent, i.e., free of systematic errors (e.g., Sanders & Binney 2015). The disk scale length is the most important unknown in disentangling the contributions from the disk and the dark halo to the mass distribution near the disk. In contrast to the photometric radial profile, without dynamical consistency, the mass-weighted radial profile cannot have been reliably measured in earlier kinematic studies.

Sanders & Binney (2015) revisit the SEGUE analysis and instead treat the chemical (and phase) space as a continuous distribution. They introduce the idea of an extended distribution function (EDF) $f(\mathbf{J}, \mathbf{Z})$ in place of the DF $f(\mathbf{J})$, where \mathbf{Z} defines the chemical domain. Though different abundance groups can have very diverse kinematics, they all necessarily reside within the same Galactic potential; the extra information in the EDF allows for a more accurate treatment of the selection function and associated errors across the survey. They determine that the thick disk vertical dispersion σ_z^T is a factor of two larger than the thin disk value ($\sigma_z^t \approx 25 \text{ km s}^{-1}$), in agreement with Sharma et al. (2014) and Piffl et al. (2014a). Unlike either of these studies, they obtain sensible numbers for both $R_{\sigma,R}^t$ and $R_{\sigma,R}^T$ for the first time, with a disk scale length R^t ($\approx 2.3 \text{ kpc}$) 35% smaller than that of the thick disk R^T (**Table 5**), but in conflict with the APOGEE survey (Hayden et al. 2015). (Although R_σ defines the scale of the outward decline of the stellar dispersion, it is not the exponential radial scale length used in the kinematic studies because DFs are expressed in terms of integrals of motion, not radii.) Sanders & Binney state that their analysis

σ_R^t : old thin disk radial velocity dispersion at R_0 , $35 \pm 5 \text{ km s}^{-1}$

σ_z^t : old thin disk vertical velocity dispersion at R_0 , $25 \pm 5 \text{ km s}^{-1}$

σ_R^T : thick disk radial velocity dispersion at R_0 , $50 \pm 5 \text{ km s}^{-1}$

σ_z^T : thick disk vertical velocity dispersion at R_0 , $50 \pm 5 \text{ km s}^{-1}$

is only preliminary because Φ was kept fixed throughout. Arguably, this study comes closest to the ideal of chemodynamical self-consistency. In the margin note, we adopt the RAVE velocity dispersions (Piffl et al. 2014a) as these are consistent across studies and extend further into the lower latitudes of the disk.

5.4.1. Vertical density and acceleration. Measurements of the local baryon and dark matter density have a long tradition in astronomy (Kapteyn 1922). From a survey of K giants toward the South Galactic Pole, Kuijken & Gilmore (1989) went further and attempted to derive the vertical density profile $\rho(z)$ and the gravitational acceleration K_z induced by the local disk that are related through Poisson’s equation $\nabla \cdot K_z = -4\pi G\rho$. This is transformed into a surface density Σ such that

$$\Sigma = -\frac{K_z}{2\pi G} + \Delta\Sigma \quad (2)$$

evaluated over the column $z = \pm 1.1$ kpc or $z = \pm \infty$. As McKee et al. (2015) point out, this must be done with care. The usual assumption that $\Delta\Sigma = 0$ for a flat rotation curve at the midplane leads to an error because, in this instance, the rotation curve cannot be flat at a fixed height off the plane. In any event, this is a difficult measurement to get right because stellar surveys are strongly biased toward more distant stars (cf. Zheng et al. 2001).

We can be confident that we do understand the local acceleration of the disk and the make-up of the local density (Section 5.4.3) over a vertical distance of $|z| = 1.1$ kpc (Kuijken & Gilmore 1989, Bovy & Tremaine 2012). A dynamical fit to 200,000 giants in the RAVE survey (Piffl et al. 2014a) leads to a local determination of K_z and its local gradient (**Figure 14b**), which are in generally good agreement with the SEGUE dwarf analysis.

The vertical density profile $\rho(z)$ determined by Gilmore & Reid (1983) for dwarf stars has survived the test of time (**Figure 14a**). Modern surveys are either too shallow (e.g., 2MASS) or too deep (e.g., SEGUE) to properly represent the disk, although good agreement is found with the SDSS dwarf photometry (Jurić et al. 2008) after careful reanalysis (Piffl et al. 2014a). Binney et al. (2014) note that the kinematics of the cool dwarfs and giants in RAVE are consistent, such that dynamical model fits for giants or dwarfs can reasonably adopt Gilmore & Reid (1983) as a starting point, as has been done by most dynamical studies.

Given Gilmore & Reid (1983) or a similar density profile (e.g., Kuijken & Gilmore 1989), the dynamical modeling attempts to find a self-consistent mass model–DF pair. This means that the mass distribution of the stellar disk implied by the DF in the potential is consistent with the mass distribution of the stellar disk assumed in the mass model. The action integral analysis of Piffl et al. (2014a) used $\sim 200,000$ giants in the RAVE survey. In **Figure 14b**, Piffl et al. find remarkable dynamic self-consistency in the local disk as defined above. Moving away from the Solar Neighborhood, they infer a declining vertical force with R as expected, in good agreement with the Bovy & Rix (2013) analysis of SEGUE dwarfs ($5 < R < 9$ kpc). The latter study derived a mass-weighted scale length of $R_M = 2.15 \pm 0.14$ kpc, which is smaller than the $R_M = 2.68$ kpc (without a quoted error) inferred by the RAVE analysis. R_M is dynamical by nature and is blind to the separate contributions of the ISM and the thin/thick disks.

5.4.2. Stellar disk mass. In **Table 5**, three of the dynamical studies (BR13, P14, and SB15) explicitly fit for an axisymmetric stellar disk, some with an assumed bulge. The total stellar mass of the disk rescaled to our value for R_0 is $4 \pm 1 \times 10^{10} M_\odot$, within the range inferred by Flynn et al. (2006). Thus, using the normalization in Section 5.1.3, we infer $M^t = 3.5 \pm 1 \times 10^{10} M_\odot$ and $M^T = 6 \pm 3 \times 10^9 M_\odot$. The total stellar disk mass is consistent with the models discussed in Section 6.4 if we include the long bar as part of the disk.

M^t : thin disk stellar mass,
 $3.5 \pm 1 \times 10^{10} M_\odot$

M^T : thick disk stellar mass,
 $6 \pm 3 \times 10^9 M_\odot$

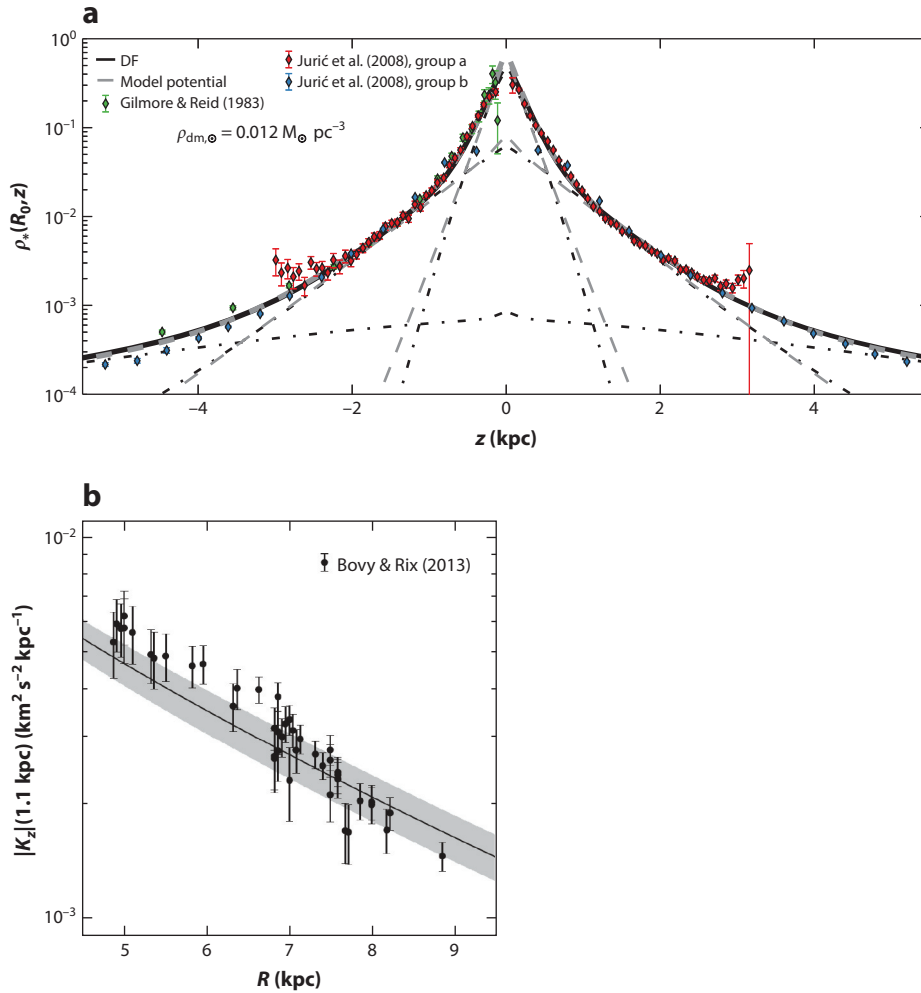


Figure 14

(a) The vertical density profile at the position of the Sun; the data points are from Gilmore & Reid (1983) and Jurić et al. (2008). The total density from the potential (sum of disk, bulge, and halo), shown as a dashed line, follows the predicted total density from the distribution function (DF) using the dynamical model shown as a solid line. The model fit exhibits a high degree of dynamical consistency over the local disk. (b) Estimates of K_z over the radial range $5 < R < 9$ kpc at a vertical height of $z = 1.1$ kpc. The data points are from the SEGUE dwarf survey (Bovy & Rix 2013) and the solid line (*gray band*) (uncertainty) is a dynamical model fit to the RAVE survey (Piffl et al. 2014a). Although the data have a slightly shorter scale length compared to the RAVE model, there is a moderate dynamical consistency between them. Adapted from Piffl et al. (2014a) with permission.

5.4.3. Local mass budget. In a new study, McKee et al. (2015) revise the local baryon inventory of Flynn et al. (2006) in light of new observations. Inter alia, they update the present-day stellar mass function as well as the vertical distributions and extents of both gas and stars. They find the baryon surface density integrated to infinity is $\Sigma_{\text{bary}} \approx 47 \pm 3 M_{\odot} \text{ pc}^{-2}$ comprising brown dwarfs ($1.2 M_{\odot} \text{ pc}^{-2}$), white dwarfs ($4.9 M_{\odot} \text{ pc}^{-2}$), ISM gas ($13.7 M_{\odot} \text{ pc}^{-2}$), and main sequence and giant stars ($27.0 M_{\odot} \text{ pc}^{-2}$). Interestingly, that least understood of main sequence stars—the

Σ_{tot} : total mass
surface density
 $|z| \leq 1.1$ kpc at R_0 ,
 $70 \pm 5 \text{ M}_\odot \text{ pc}^{-2}$

ρ_{tot} : local mass density
at R_0 , 0.097 ± 0.013
 $\text{M}_\odot \text{ pc}^{-3}$

ϵ_{tot} : local dark matter
energy density at R_0 ,
 $0.49 \pm 0.13 \text{ GeV cm}^{-3}$

M dwarf—makes up more than half of all stars by mass locally. Over the column $z = \pm 1.1$ kpc, there is general agreement that the total surface density (baryons + dark matter) is $\Sigma_{\text{tot}} \approx 70 \pm 5 \text{ M}_\odot \text{ pc}^{-2}$ (Kuijken & Gilmore 1989, Catena & Ullio 2010, McMillan 2011, Bovy & Rix 2013, Piffl et al. 2014a).

In terms of local density, the proportion of each mass constituent is very different due to the wide spread in scale heights. McKee et al. (2015) give the local mass density as $\rho_{\text{tot}} \approx 0.097 \pm 0.013 \text{ M}_\odot \text{ pc}^{-3}$ comprising stars ($0.043 \pm 0.04 \text{ M}_\odot \text{ pc}^{-3}$), gas ($0.041 \pm 0.04 \text{ M}_\odot \text{ pc}^{-3}$), baryons ($0.084 \pm 0.04 \text{ M}_\odot \text{ pc}^{-3}$), and dark matter ($0.013 \pm 0.003 \text{ M}_\odot \text{ pc}^{-3}$ or equivalently $0.49 \pm 0.13 \text{ GeV cm}^{-3}$).

5.5. Outer Disk

The physical extent and detailed structure of the outer disk are highly uncertain. Over the years, different authors have claimed evidence for an “edge” in the stellar disk in the range of $R_{\text{GC}} \sim 10$ – 15 kpc from both optical and IR surveys (Habing 1988, Robin et al. 1992, Ruphy et al. 1996, Minniti et al. 2011). When looking at external galaxies, what appear to be edges can be inflexions in the stellar density, i.e., a break in the exponential density profile. Such “breaks” are common (Pohlen & Trujillo 2006) but “continuously exponential” disks are also known, and the stars can extend to the observed edge of the H I disk (Bland-Hawthorn et al. 2005, Irwin et al. 2005, Ellis & Bland-Hawthorn 2007).

Many new observations confirm that the outer disk is very complicated. The outer disk warps slowly away from the Galactic Plane in both H I (May et al. 1993) and stars (Carney & Seitzer 1993). In addition to the warp, the outer disk flares in both stars and gas and possesses a fair degree of substructure. Moni Bidin et al. (2012) review the contradicting claims for the flaring stellar disk, but the comprehensive study by Momany et al. (2006) puts the issue beyond doubt. Carraro (2015) reviews the evidence for flaring in the outer disk in both young and old stellar populations (Cepheids, pulsars). The earlier claims of a disk edge did not consider the effect of a warping, flaring disk, so there is no strong evidence for a truncation to date in either old or young populations (López-Corredoira et al. 2002, Sale et al. 2009, Carraro et al. 2010).

A complicating factor is the presence of the near-planar Monoceros Ring at $R_{\text{GC}} \approx 15$ – 20 kpc (radial width ≈ 2 kpc) that appears to corotate at roughly the speed of the outer disk (Newberg et al. 2002, Ibata et al. 2003). The nature of this stream is unknown (cf. Xu et al. 2015): Unlike the Canis Major overdensity, which may be related to the warp, the ring appears to have its own identity after correcting for the warp (Momany et al. 2006) and may even rotate slightly faster than the disk (Ivezić et al. 2008).

Before the optical studies, H I observations by Burton (1988) and Diplas & Savage (1991) identified Galactic gas out to at least $R_{\text{GC}} \sim 25$ – 30 kpc (see also Hartmann & Burton 1997). Molecular gas clouds are seen to $R_{\text{GC}} \gtrsim 20$ kpc, some with ongoing star formation (Kobayashi et al. 2008, Yasui et al. 2008). Further evidence for recent star formation out to these distances is the presence of young stars and open clusters (Carraro et al. 2010, Magrini et al. 2015). Remarkably, Kalberla & Dedes (2008) have pushed the H I frontier to $R_{\text{GC}} \sim 60$ kpc, which is within range of the orbiting Magellanic Clouds. The stellar/gaseous warp may be highly transient, triggered by the passage of the Magellanic Clouds or Sgr dwarfs, with bending waves that travel at $\pi G \Sigma / \omega \sim 20 \text{ kpc Gyr}^{-1}$ near the Solar Circle; Σ and ω are the local surface density and angular velocity of the disk, respectively.

6. HALO

In this section, we review the stellar, gaseous, and dark matter halos of the Galaxy and finally put together a global rotation curve for the Milky Way. This analysis brings together many of

the key themes of the review. The stellar and dark matter halos share the property that they are 3D structures surrounding the disk and still grow by accreting matter. However, they do not necessarily share the same structural properties or formation histories. The gaseous halo is an important repository for a part of the Galaxy's baryonic mass and interacts with the environment through inflows and outflows.

All three components live in the same gravitational potential, which at intermediate radii ($\sim R_0$) is shaped by the Galactic bulge, disk, and dark halo, and at large (~ 100 kpc) radii is completely dominated by the dark matter. One important goal of studying the halo and the satellites around the Milky Way is to map out the large-scale gravitational potential—this is a major science goal of the ongoing *Gaia* mission.

6.1. Stellar Halo

The Milky Way's stellar halo, although containing just $\sim 1\%$ of the total stellar mass, is an important component for unravelling our Galaxy's formation history. It was first identified as a population of old, high-velocity, metal-poor stars near the Sun, similar to the stars in globular clusters. The halo stars showed large random motions, little if any rotation, and a spheroidal to spherical spatial distribution. Following the influential paper of Eggen et al. (1962), the classical view of the halo developed as that of a smooth envelope of ancient stars from the time when the Galaxy first collapsed. Subsequently, Searle & Zinn (1978) suggested that the halo is built up from independent infalling fragments, based on their observation that halo globular clusters showed a wide range of metal abundances independent of Galactocentric distance.

Modern data from large stellar surveys show that the stellar halo has a complex structure with multiple components and unrelaxed substructures and that it continues to accrete matter in the form of smaller galaxies, which are then tidally disrupted in the gravitational field (e.g., Ibata et al. 1997, Belokurov et al. 2006, Schlafman et al. 2009). This confirms the predictions of hierarchical galaxy-formation models. Because of the long dynamical timescales in the halo, tidal tails, shells, and other overdensities arising from accreted dwarf galaxies remain observable over gigayears, thus constituting a fossil record of the Milky Way's accretion history. Previous reviews on this subject have been written by Helmi (2008), De Lucia (2012), Belokurov et al. (2013).

Cosmological simulations reveal that the Galaxy should have accreted ~ 100 satellite galaxies that would mostly have been disrupted by the tidal field, causing the build-up of the stellar halo. Irregular density distributions are predicted in the outer halo due to shells and tidal streams, with a large variance between different galaxies of the same dark matter halo mass. In these models, the majority of the halo is often built at early times, ~ 10 Gyr ago, and most of the stellar halo stars come from the disruption of one or a few massive satellites accreted early on. The outer halo is built more recently than the inner halo, and the halo properties evolve, reflecting the history of accretion (Bullock & Johnston 2005, Font et al. 2006, De Lucia & Helmi 2008, Cooper et al. 2010, Pillepich et al. 2014).

Part of the inner halo may have formed in situ, i.e., within the main body of the Galaxy (Abadi et al. 2006). Recent simulations suggest that a fraction of stars formed in the early Galactic disk could have been ejected into the inner halo, and further in situ halo stars could have formed from gas stripped from infalling satellites (Font et al. 2011, McCarthy et al. 2012, Tissera et al. 2013, Cooper et al. 2015, Pillepich et al. 2015), but the quantitative importance of these processes is not yet fully understood. Observationally, evidence for a dual halo has been put forward by Carollo et al. (2007) and Beers et al. (2012), but see Schönrich et al. (2014).

In this section, we review the structural parameters of the Milky Way's stellar halo and put them in the context of these hierarchical models. Determination of the mass of the dark matter halo based on these data is discussed in Section 6.3.

α_{in} : inner halo density slope, -2.5 ± 0.3

α_{out} : outer halo density slope, $-(3.7-5.0)$

r_s : break radius, 25 ± 10 kpc

q_{in} : inner halo flattening, 0.65 ± 0.05

q_{out} : outer halo flattening, 0.8 ± 0.1

6.1.1. Halo flattening and average density profile. The stellar density of the halo is important because it reflects the cumulative past accretion history of the Milky Way. It has been extensively studied using several tracers for which good distances can be determined, including RR Lyrae stars (typical distance accuracy $\sim 7\%$, Vivas & Zinn 2006), blue horizontal branch (BHB) stars ($\sim 5\%$, Belokurov et al. 2013), red giant branch (RGB) stars ($\sim 16\%$, Xue et al. 2014), and near-main-sequence turnoff (nMSTO) stars ($\sim 10\%$ with multiple colors, Ivezić et al. 2008). RR Lyrae and BHB stars, which trace the old metal-poor populations, are rarer than RGB and nMSTO stars, but can reach to $r \sim 100$ kpc galactocentric radius. RGB stars trace all halo populations and currently reach to about $r \sim 50$ kpc, whereas nMSTO stars are abundant and best for the inner halo, i.e., $r \lesssim 20$ kpc.

A significant fraction of these halo tracer stars are found in large substructures (Section 6.1.2). Subtracting these leads to an estimate of a smooth halo component (e.g., Deason et al. 2011), which, however, may contain smaller, yet unresolved substructures (e.g., Sesar et al. 2013). The spatial distributions of the halo stars are typically fitted by spherical or axisymmetric density models with single power-law or double power-law (DPL) or Sérsic radial profiles, and with one or two flattening parameters for the inner and outer halo; **Table 6** shows recent results based on DPL models. The inner halo flattening is found to be $q_{\text{in}} = 0.65 \pm 0.05$ across various studies based on data reaching down to $r \sim 5$ kpc (see also Bell et al. 2008, Jurić et al. 2008). The inner power-law slope is encompassed by $\alpha_{\text{in}} = -2.5 \pm 0.3$. (The quoted formal fit errors are often quite small, but this could easily depend on the chosen parametric form, the data volume, and remaining substructures in the data.) No evidence is found for an outward gradient in q for the RR Lyrae and BHB samples, but Xue et al. (2015) with RGB and Pila-Díez et al. (2015) with nMSTO stars find an increase to $q_{\text{out}} = 0.8$ by $r = 30$ kpc.

There is clear evidence that the stellar halo profile steepens with radius; see **Table 6**. In the context of DPL models based on data reaching $r \sim 50$ kpc, the break radius between the inner and outer components scatters in the range $r_s = 25 \pm 10$ kpc. For RR Lyrae and BHB stars, the outer power-law slope is in the range of $\alpha_{\text{out}} = -4.5 \pm 0.5$, and Deason et al. (2014) found an even steeper profile beyond 50 kpc. For RGB stars the slope is somewhat shallower, $\alpha_{\text{out}} = -3.8 \pm 0.1$. The overall density profile is similar to an Einasto function (e.g., Xue et al. 2015), and qualitatively similar to density profiles predicted by halo formation models (Bullock & Johnston 2005, Cooper

Table 6 Recent measurements of stellar halo density parameters

Reference	Tracer	r (kpc)	$-\alpha_{\text{in}}$	q_{in}	r_s (kpc)	$-\alpha_{\text{out}}$
Xue et al. (2015)	RGB	10–60	2.1 ± 0.3	0.70 ± 0.02	18 ± 1	3.8 ± 0.1
Pila-Díez et al. (2015)	nMSTO	10–60	2.5 ± 0.04	0.79 ± 0.02	19.5 ± 0.4	4.85 ± 0.04
Sesar et al. (2011)	nMSTO	5–35	2.62 ± 0.04	0.70 ± 0.02	27.8 ± 0.8	3.8 ± 0.1
Deason et al. (2011)	BHB, BS	10–45	2.3 ± 0.1	0.59 ± 0.03	27.1 ± 1	4.6 ± 0.15
Faccioli et al. (2014)	RRL	9–49	2.8 ± 0.4	0.7 fixed	28.5 ± 5.6	4.4 ± 0.7
Sesar et al. (2013)	RRL	5–30	1–2.7	0.63 ± 0.05	16 ± 1	2.7 ± 0.3
Sesar et al. (2010)	RRL	9–49	2.8 ± 0.2	0.7 fixed	34.6 ± 2.8	5.8 ± 0.9
Watkins et al. (2009)	RRL	9–49	2.1 ± 0.3	0.59 fixed	26.9 ± 3.1	4.0 ± 0.3

Note: Halo density parameters from recent studies of halo tracer stars with oblate double power-law (DPL) models. Columns give reference, tracer used, covered Galactic radius range, inner power-law slope, inner halo axis ratio, break radius, and outer power-law slope (in these models, the outer $q_{\text{out}} = q_{\text{in}}$). Watkins et al. (2009) and Sesar et al. (2010) considered spherical DPL models; the numbers given in these lines are from a reanalysis by Faccioli et al. (2014).

Abbreviations: BHB, blue horizontal branch; BS, blue stragglers; nMSTO, near-main-sequence turnoff; RGB, red giant branch; RRL, RR Lyrae.

et al. 2010). Deason et al. (2013) use simulations to show that a distinct density break may be related to the accumulation of stars at their apocenters, following relatively massive accretion events. Lowing et al. (2014) point out that the measured density parameters depend strongly on the surveyed sightlines and halo accretion history.

6.1.2. Stellar halo mass and substructure fraction. Estimating the stellar halo mass from these density distributions is nontrivial, requiring determination of the mass normalization per halo tracer star from stellar population models and calibrations, as well as extrapolating beyond the survey volume through models. Bell et al. (2008) fitted DPL models to SDSS nMSTO stars and found a best-fit stellar halo mass within $r = 1\text{--}40$ kpc of $\sim(3.7 \pm 1.2) \times 10^8 M_\odot$. Deason et al. (2011) gave an estimate for the ratio of BHB stars per luminosity of $\sim 10^{-3}$, using data for Galactic globular clusters. With a mass-to-light ratio $M/L_V = 1.4 \pm 0.5$ for metal-poor Galactic globular clusters (Kimmig et al. 2015), the estimated stellar halo mass within $10\text{--}45$ kpc becomes $\sim 3 \times 10^8 M_\odot$.

The Milky Way halo contains numerous substructures that contain a significant fraction of its stellar mass (see Belokurov et al. 2013). The four largest stellar structures are the Sagittarius Stream, the Galactic Anticenter Stellar Structure, the Virgo Overdensity, and the Hercules-Aquila Cloud. Estimated masses for these structures are, respectively, $\sim 0.8\text{--}1.5 \times 10^8 M_\odot$ based on the luminosity from Niederste-Ostholt et al. (2010) and $M/L_V = 1.4 \pm 0.5$ from Kimmig et al. (2015); $\sim 10^8 M_\odot$ (Yanny et al. 2003, Belokurov et al. 2013); $\lesssim 10^6 M_\odot$ (Bonaca et al. 2012); and $\sim 10^7 M_\odot$ based on Belokurov et al. (2007), altogether summing to $\sim 2\text{--}3 \times 10^8 M_\odot$. A significant fraction of this substructure mass is within the volume traced by the SDSS nMSTO stars. We therefore add $\sim 50\%$ of this mass to the result of Bell et al. (2008) to obtain a rough estimate for the total stellar halo mass $M_s = 4\text{--}7 \times 10^8 M_\odot$. This is somewhat lower than the classical value based on Morrison (1993).

Bell et al. (2008) also quantified the fraction of mass in substructures from the ratio of the rms deviation of the density of nMSTO stars to the total density given through a smooth halo model. They find $\sigma/\text{total} = 40\%$, arguing that much of the halo was accreted from satellite galaxies. In their study of BHB stars, Deason et al. (2011) found a lower σ/total of $\sim 5\text{--}20\%$ with some increase for fainter stars (larger distances); on this basis they argue for a smooth halo with superposed additional substructures. Reasons for the discrepancy between both studies could be the less accurate nMSTO distances, leading to blurring of compact substructures; the lower resolution with the rarer BHB stars; or that the BHB stars trace an older, more mixed population of stars (Deason et al. 2011). Resolving this issue requires large samples of stars with accurate distances and velocities. The problem is that even a fully accreted halo will eventually mix to be smooth above a given scale and that mixing times are shortest in the high-density inner regions.

6.1.3. Halo rotation, velocity dispersion, and anisotropy. Bond et al. (2010) analyzed the largest sample so far of halo star velocities within ~ 10 kpc from the Sun, including $\sim 10^5$ SDSS stars with three velocity components. They found (a) a mean rotation of halo stars (see their figure 5) of $\bar{v}_\phi^s \simeq \Theta_0 + V_\odot - 205 \text{ km s}^{-1} \simeq 40 \text{ km s}^{-1}$ for our adopted $\Theta_0 = 238 \text{ km s}^{-1}$ and $V_\odot = 10.5 \text{ km s}^{-1}$ (Section 6.4); (b) a velocity ellipsoid whose principal axes align well with spherical coordinates; and (c) corresponding halo velocity dispersions $(\sigma_r^s, \sigma_\theta^s, \sigma_\phi^s) = (141, 75, 85) \text{ km s}^{-1}$, with a total error in each component of $\sim 5 \text{ km s}^{-1}$. These values are in excellent agreement with results from Smith et al. (2009). Note that the close alignment of the halo velocity ellipsoids with spherical coordinates does not imply a spherical potential (see Evans et al. 2016).

Figure 15 shows the RV dispersion profile in the outer halo based on several data sets. $\sigma_r(r)$ sharply decreases from the local 141 km s^{-1} to 100 km s^{-1} at $r \sim 20$ kpc, then remains

M_{sub} : stellar halo mass in substructures, $2\text{--}3 \times 10^8 M_\odot$

M_s : total stellar halo mass, $4\text{--}7 \times 10^8 M_\odot$

$(\sigma_r^s, \sigma_\theta^s, \sigma_\phi^s)$: spherical velocity ellipsoid of the local halo, $(141, 72, 85) \text{ km s}^{-1}$ ($\pm 5 \text{ km s}^{-1}$)

\bar{v}_ϕ^s : mean rotation of the local halo, $\sim 40 \text{ km s}^{-1}$

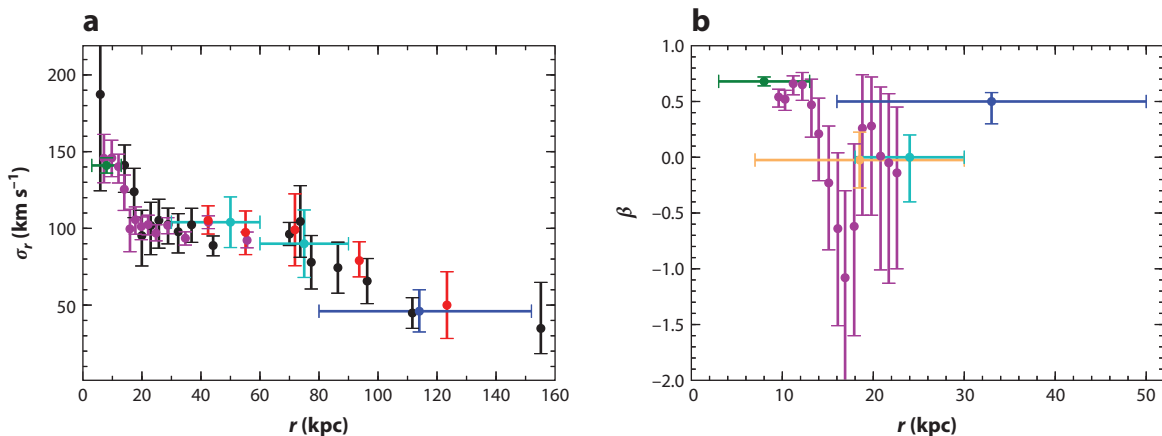


Figure 15

(a) Radial velocity dispersion profile for several outer halo tracers, including near-main-sequence turnoff (nMSTO) stars (Bond et al. 2010, *green*), blue horizontal branch (BHB) stars (Kafle et al. 2012, *purple*; Deason et al. 2013, *blue*), blue straggler stars (Deason et al. 2012, *cyan*), K giants (Kafle et al. 2014, *black*), and mixed tracers (Battaglia et al. 2005, *red*). (b) Measurements of orbital anisotropy in the halo, for nearby (Bond et al. 2010, *green*) and distant nMSTO stars (Deason et al. 2013, *cyan*), and BHB stars (Kafle et al. 2012, *purple*; Sirko et al. 2004, *yellow*; Deason et al. 2012, *blue*).

approximately flat until $r \sim 70$ kpc, and finally decreases to about 35 km s^{-1} at ~ 150 kpc. At the largest radii, where the stellar density profile is largely unknown (see **Table 6**), the very low σ_r values are consistent with a tidal truncation of an extrapolated steep $n \propto r^{-4.5}$ power law (Kafle et al. 2014).

Tangential velocities can be estimated from the variation of LOS velocities across the sky and from PMs. Fermani & Schönrich (2013) used BHB stars reaching to $r \sim 50$ kpc and with both kinds of methods find no rotation in either the inner or outer halo and no trend with metallicity. Tangential velocity dispersions and the spherical anisotropy parameter $\beta(r)$ were determined in the outer halo by several authors and are shown in **Figure 15**. The radial anisotropy $\beta = 0.5$ – 0.7 at small and large radii is consistent with predictions for accreted halos (Abadi et al. 2006). The tangential anisotropy at radii around $r \sim 17$ kpc was confirmed by King et al. (2015) but was suggested to be transient based on orbit simulations (Bird & Flynn 2015), perhaps due to a yet unknown substructure in the halo.

6.2. Hot Halo

The existence of a diffuse hot plasma (or corona) surrounding the Galactic disk has been widely discussed since Spitzer’s early observation that the ubiquitous H I clouds must be confined by an external medium (Spitzer 1956). But it remains uncertain how much of the gas lies close to the Galactic Plane, and how much of it extends into the halo (Bland-Hawthorn & Cohen 2003). Strong evidence for extended coronae have come from the first reliable detections of hot halos around nearby massive disk galaxies (e.g., Anderson & Bregman 2011). The Galactic corona also explains the remarkable observation of gas depletion in all dwarfs within a radius of about 270 kpc, with the exception of the high-mass LMC and SMC dwarfs (Grcevich & Putman 2009), which is well understood in terms of ram-pressure stripping by a hot medium (Nichols & Bland-Hawthorn 2011, Gatto et al. 2013). Such an extended hot phase is supported by numerical simulations (Nuza et al. 2014), which focus on the properties and distribution of the multiphase gas in and around

Table 7 Estimates of gas density and temperature in the Galactic halo (corona)

Reference	d (kpc)	n_p (10^{-5} cm^{-3})	T_e (10^6 K)	M_{hot} ($10^{10} M_{\odot}$)	Method
Blitz & Robishaw (2000)	$\lesssim 250$	$\gtrsim 2.4^a$	1–1.4	1	Ram-pressure stripping of gas in dwarf spheroidals
Stanimirović et al. (2002)	15 ^b	100	1 ^c	—	Pressure equilibrium between
	45 ^b	30	1 ^c	—	HVCs (MS) and coronal gas
Sembach et al. (2003)	≈ 70	1–10	> 1	—	OVI absorption (100 LOS)
Bregman & Lloyd-Davies (2007)	< 20	90 ^d	2 ^c	0.04 ^e	OVII absorption (25 LOS) Uniform spherical halo
Anderson & Bregman (2010)	50 ^f	50 ^{a,d}	3.5	1.2–1.5	LMC pulsar dispersion measures
Gatto et al. (2013)	50–90	36–13 ^a	1.8 ^c	3.4–4.8	Ram-pressure stripping of gas in Carina and Sextans
Miller & Bregman (2015)	10–100	200–4 ^a	2 ^c	2.7–4.7	OVII/OVIII emission (650 LOS)
Salem et al. (2015)	48.2 ± 5	11 ± 4.5	—	2.6 ± 1.4^g	Ram-pressure stripping of the LMC disk

^aAverage density out to the given distance.

^bDistance from the Galactic Plane.

^cAssumed.

^dElectron density.

^eMass enclosed within 20 kpc.

^fDistance from the Sun.

^gMass enclosed within ~ 300 kpc.

Note: Unless otherwise indicated, all coronal masses M_{hot} are integrated out to r_{vir} ; the gas density is quoted as a total particle density unless otherwise indicated. Dashes, —, indicate no data.

Abbreviations: HVC, high-velocity cloud; LMC, Large Magellanic Cloud; LOS, line of sight; MS, main sequence.

two simulated galaxies chosen as an M31-Galaxy analogue. They found the hot ($T \gtrsim 10^5$ K) gas has a uniform temperature profile around each of the simulated galaxies and good agreement between the observed profile (Miller & Bregman 2015) and the density profile of the simulated Galaxy.

We tabulate the most recent observations of the Galactic corona in **Table 7**. The best evidence for a hot corona comes from bright active galactic nucleus sight lines with detections of OVI and OVII in absorption, and in high-resolution X-ray spectra (Paerels & Kahn 2003) of a nearly ubiquitous soft X-ray background with energies in the range of 0.1–1.0 keV (implying temperatures of $\sim 10^{6-7}$ K), with some contribution of OVI and OVII in emission (Snowden et al. 1997, Henley & Shelton 2012). The sensitivity of current X-ray spectroscopy limits OVI and OVII detections to a handful (~ 30) of sight lines. There is an additional difficulty in disentangling the contribution of the Local Bubble, a supernova remnant in which the Solar System is embedded (Snowden et al. 1990), and the contribution from solar wind charge-exchange processes, which produce soft X-ray emission throughout the Solar System (Cravens et al. 2001). Consequently, the detailed structure (density, temperature, entropy profile) of the Galactic corona, and hence its total mass, is uncertain.

The Galactic hot halo is likely to comprise two main components: one exponentially decaying, high-metallicity ($Z > 0.3 Z_{\odot}$) component with a scale height of a few kiloparsecs, which dominates the X-ray observations; and an extended ($\gtrsim 100$ kpc), more diffuse, low-metallicity halo (Yao &

M_{hot} :	Galactic corona baryonic mass ($r \lesssim r_{\text{vir}}$), $2.5 \pm 1 \times 10^{10} M_{\odot}$
M_{bary} :	Galactic total baryonic mass ($r \lesssim r_{\text{vir}}$), $8.5 \pm 1.3 \times 10^{10} M_{\odot}$
f_{bary} :	Galactic baryonic mass fraction, $7 \pm 1\%$

Wang 2007). Purely exponential gas density profiles (i.e., not characterized by a single temperature) overpredict the coronal temperature and X-ray surface brightness by factors of a few (Fang et al. 2013).

Early attempts to model the corona using X-ray observations assumed (unphysically) that it was isothermal and at a constant density (Bregman & Lloyd-Davies 2007, Gupta et al. 2012). The studies arrived at wildly different conclusions: The first study derived an electron density $n_e = 9 \times 10^{-4} \text{ cm}^{-3}$ at $r = 19 \text{ kpc}$; the second found $n_e \geq 2 \times 10^{-4} \text{ cm}^{-3}$ at $r \geq 139 \text{ kpc}$ (cf. Wang & Yao 2012). Fang et al. (2013) favored a picture in which the corona is composed of adiabatic (isentropic) gas in hydrostatic equilibrium with the Galactic potential, in conflict with evidence that the Galactic halo is far from having a constant entropy profile (Crain et al. 2010, Miller & Bregman 2015). It is now well established that the halo temperature as inferred from X-ray observations is fairly uniform across the sky and with little scatter around $T \approx 2 \times 10^6 \text{ K}$ (Henley et al. 2010), although this does not demand that the halo is strictly isothermal.

A new all-sky catalog of OVII and OVIII emission lines (Henley & Shelton 2012) has been studied by Miller & Bregman (2013, 2015). They used this catalog in combination with X-ray measurements to determine that the halo density is of order 10^{-5} cm^{-3} to 10^{-4} cm^{-3} at $10 \text{ kpc} \lesssim r \lesssim 100 \text{ kpc}$. They determine a coronal gas mass of $\sim 10^{10} M_{\odot}$ within $r \approx 250 \text{ kpc}$. These results rely on key assumptions: (a) the density profile of the hot gas is well described by a spherically symmetric β -model of the form $n(r) \propto r^{-\beta/2}$, consistent with a truncated King model for the halo potential; (b) the halo is isothermal with a temperature $T = 2 \times 10^6 \text{ K}$; (c) the gas is in collisional ionization equilibrium. Miller & Bregman’s model can be justified if the dark matter halo of the Galaxy is well described by a spherically symmetric isothermal sphere with a core radius $r_c \sim 0.1 \text{ kpc}$ and if the gas is quasi-isothermal and in approximate hydrostatic equilibrium with the potential.

Tepper-Garcia et al. (2015) bring all of this work together and search for a physically plausible corona that is consistent with the observed stellar halo dynamics and with the UV/X-ray measurements (Table 7). They normalize the dark matter halo to the density profile and total mass inferred from the kinematics of halo stars (Kafle et al. 2012). If the dark matter halo is isothermal, the core radius is somewhat larger than inferred from Miller & Bregman’s model, i.e., $r_c \approx 0.5 \text{ kpc}$. The halo velocity dispersion implies a gas temperature of $T \sim 10^6 \text{ K}$, leading to a density profile that is in broad agreement with Miller & Bregman (2015) and Nuza et al. (2014) with about the same total gas mass. The most likely baryonic mass range for the Galactic corona is $M_{\text{hot}} \sim 2.5 \pm 1 \times 10^{10} M_{\odot}$.

The dynamical analyses presented in Section 5.4 are relatively consistent in their estimates of the baryonic mass fraction of the Galaxy (stars + cold gas), i.e., $M_{\text{cold}} \sim 6 \pm 1 \times 10^{10} M_{\odot}$ (Table 5). We now add the likely contribution from the hot corona M_{hot} within r_{vir} to arrive at a total baryonic mass, $8.5 \pm 1.3 \times 10^{10} M_{\odot}$. This leads to a baryonic mass fraction out to r_{vir} of $f_{\text{bary}} = M_{\text{bary}}/M_{\text{vir}} \approx 7 \pm 1\%$, which falls well short of the universal value ($\approx 16\%$; Hinshaw et al. 2003).

6.3. Dark Halo

An accurate measurement of the Galaxy’s total mass is central to our understanding of how it fits into the cold dark matter paradigm. We need to know the mass of the dark matter that has had time to virialize in the Galaxy, the so-called virial mass M_{vir} defined within the virial radius r_{vir} . There is some confusion in the literature on the convention for a galaxy’s total mass, i.e., how it should be defined and at what epoch (Shull 2014). M_{vir} is usually expressed as the mass within a region around the center in which the average density exceeds a multiple of the mean density of the Universe (either the closure density or the mass density). We follow the definition of Klypin

et al. (2002) and Kafle et al. (2014), where $\rho_{\text{vir}} = \Delta_{\text{vir}} \Omega_{\text{M}} \rho_{\text{crit}}$ ($\Delta_{\text{vir}} = 340$) such that

$$r_{\text{vir}} = 258 \left(\frac{\Delta_{\text{vir}} \Omega_{\text{M}}}{102} \right)^{-1/3} \left(\frac{M_{\text{vir}}}{10^{12} M_{\odot}} \right)^{1/3} \text{ kpc.} \quad (3)$$

Because the mass enclosed depends on the product $\Delta_{\text{vir}} \Omega_{\text{M}}$, our values are within 5% of estimators that use $(\Delta_{\text{vir}}, \Omega_{\text{M}}) = (360, 0.27)$ (e.g., van der Marel et al. 2012a). Note that if the dark matter can be represented by a Navarro, Frenk & White (NFW) halo, its scale length is $r_b \approx 25$ kpc, assuming a concentration parameter $c \approx 10$ (**Figure 1**; van der Marel et al. 2012a). Another widely used mass estimator is M_{200} , where the average density within r_{200} is $\rho_{200} = 200 \rho_{\text{crit}}$, which is 16% smaller than M_{vir} for our adopted parameters (Bryan & Norman 1998, Klypin et al. 2002). M_{vir} is not strictly a total mass because the dark matter profiles are thought to extend (and rapidly truncate) beyond the virial radius.

One constraint for the total mass of the Milky Way comes from the “timing mass” argument (Kahn & Woltjer 1959): The masses of M31 and the Galaxy must be sufficient to overcome universal expansion to explain their present-day kinematics being consistent with a head-on collision and a future merger in ~ 6 Gyr (van der Marel et al. 2012b). Timing mass estimates in early work (e.g., Li & White 2008) are now thought to be consistently too high. These have come down significantly owing to improved relative motions for both galaxies and a more accurate estimate of the solar reflex motion (Section 6.4). By selecting galaxy pairs in the Millennium simulations (after Li & White), van der Marel et al. (2012a) determine a (virial) timing mass of $4.9 \pm 1.6 \times 10^{12} M_{\odot}$ for the mass within the virial radius of both galaxies ($4.1 \pm 1.4 \times 10^{12} M_{\odot}$ for $r \leq r_{200}$). After considering the orbit of M33 about M31, they further reduce the total timing mass to $M_{\text{vir, timing}} = 3.2 \pm 0.6 \times 10^{12} M_{\odot}$. Modern mass estimates for M31 reveal that it is comparable with the Milky Way (van der Marel et al. 2012a) such that the timing mass provides an upper limit of $M_{\text{vir}} \lesssim 1.6 \times 10^{12} M_{\odot}$ for the Galaxy.

Unlike the timing mass, most mass estimators are limited to the region explored by the available tracer population, whose spatial distribution and kinematics are used to estimate the enclosed mass. Estimates of the Milky Way’s mass have been obtained based on the kinematics of halo stars, the kinematics of satellite galaxies and globular clusters, the evaluation of the local escape velocity, and the modeling of satellite galaxy tidal streams. A list of direct mass determinations is compiled in **Table 8**. Dynamical analysis of halo star kinematics typically results in relatively low total mass, $M_{200} \lesssim 10^{12} M_{\odot}$ (Xue et al. 2008; Deason et al. 2012; Kafle et al. 2012, 2014). The main uncertainties in such determinations are the lack of stellar tangential velocities from PMs, and/or the need to extrapolate from spatially limited samples to the scale of the virial radius. Such extrapolation is often done using simulated galaxy halos, which then fixes the dark matter density profile, or by assuming parametric forms for the density distribution and fitting for the best parameters.

Mass estimates based on satellite and globular cluster kinematics typically result in higher values, $M_{200} = 1\text{--}2 \times 10^{12} M_{\odot}$ when the Leo I dwarf satellite galaxy is assumed to be bound to the Milky Way; however, if Leo I with its large LOS velocity is considered unbound, values more similar to $M_{200} \lesssim 10^{12} M_{\odot}$ result (Wilkinson & Evans 1999, Li & White 2008, Watkins et al. 2010). Satellite galaxies reach to larger radii, but here the main uncertainties come from small numbers and the similar lack of PM information. Determinations of the escape velocity from RVs of stars near the Sun also lead to $M_{200} = 1\text{--}2 \times 10^{12} M_{\odot}$ (Smith et al. 2007, Piffl et al. 2014b), again with the uncertainties of extrapolating the mass distributions to large radii. Modeling stellar positions and velocities along the orbit of the Sagittarius dwarf galaxy, or matching the apocenter radii of its trailing and leading arms, leads to a range of enclosed masses of $M_{\text{kpc}}^{100} = 0.4\text{--}2 \times 10^{11} M_{\odot}$ (Gibbons et al. 2014). The Galaxy’s mass can also be estimated by comparing Milky

Table 8 Total mass estimates for the Galaxy

Reference	Method	M_{200}	M_{100}	M_{kpc}^r	R_{200}	R_{100}	r
Wilkinson & Evans (1999)	Distribution function based	1.67	2.39	0.54	243.9	346.0	50
Sakamoto et al. (2003)	Mixed halo object kinematics	1.67	2.39	0.54	243.9	346.0	50
Dehnen et al. (2006)	Halo star kinematics	1.75	1.96	1.05	247.7	324.3	120
Smith et al. (2007)	Escape velocity	1.03	1.43	0.39	207.7	291.7	50
Xue et al. (2008)	Halo star kinematics	0.87	0.91	0.40	196.1	267.0	60
Gnedin et al. (2010)	Hypervelocity star kinematics	1.33	1.74	0.69	226.4	311.3	80
Watkins et al. (2010)	Satellite galaxy kinematics	2.62	3.05	2.70	283.4	375.4	300
McMillan (2011)	Modeling local observables	1.26	1.76	0.84	222.0	312.7	100
Kafle et al. (2012)	Halo star kinematics	1.21	1.99	0.21	219.1	325.5	25
Deason et al. (2012)	Halo star kinematics	0.87	1.03	0.75	196.0	261.9	150
Gonzalez et al. (2013)	Satellite galaxy kinematics	1.15	1.39	–	215.3	289.0	–
Kafle et al. (2014)	Halo star kinematics	0.72	0.80	–	184.2	239.1	–
Piffl et al. (2014b)	Escape velocity	1.60	1.90	–	235.0	322.0	–
Gibbons et al. (2014)	Stream modeling	0.55	0.68	0.41	168.7	227.3	100

Note: M_Δ is the mass within the radius defined with respect to the overdensity Δ ; the radius computed by the authors is indicated by R_Δ . M_{kpc}^r is the mass within radius r in kiloparsecs as indicated. All masses are in units of $10^{12} M_\odot$; all radii are in units of kiloparsecs. Dashes, –, indicate no data.

Way properties with various predictions of a cold dark matter simulation, such as the number of satellite galaxies larger than a given mass (Cautun et al. 2014). But these estimates are not reliable until the models improve. Finally, McMillan (2011) determined a value for the Milky Way mass from fitting parameterized mass models to a range of observations.

The halo stellar kinematic studies comprise the largest and, arguably, the most reliable data sets. These estimates lead to a straight average for $M_{200} = 1.1 \pm 0.3 \times 10^{12} M_\odot$, or equivalently $M_{\text{vir}} = 1.3 \pm 0.3 \times 10^{12} M_\odot$, consistent with the upper limit from the timing mass. Interestingly, if we derive M31’s mass from a simple scaling of peak rotation, i.e., $(260 \text{ km s}^{-1}/\Theta_0)^4 M_{\text{vir}}$, or a mass that is 40% higher than the Galaxy, this leads to a virial timing mass for the Galaxy that is equal to our estimate for M_{vir} above. The Galaxy’s virial mass cannot be much lower than $10^{12} M_\odot$ if it is to provide sufficient angular momentum to the observed baryons over its lifetime.

Besides the total halo mass, another property of considerable interest is the shape of the dark matter halo. In dark matter only simulations, halo shapes are strongly flattened, prolate-triaxial, with mean $\langle c/a \rangle = 0.5 \pm 0.1$ (e.g., Dubinski & Carlberg 1991, Allgood et al. 2006). When baryons are included, the halos become more spherical and evolve toward oblate at all radii but mostly in their inner parts (e.g., Kazantzidis et al. 2004, Bailin et al. 2005, Abadi et al. 2010). In the Milky Way, constraints on the shape of the dark halo are based on the Sgr orbit, tidal streams, SDSS kinematics, flaring of the H I layer, and combining rotation curve and vertical acceleration measurements (see the review by Read 2014).

The orbit of the Sgr dwarf, whose leading and trailing arms can each be followed $\sim 180^\circ$ across the sky, constrain the halo shape in the range $R = 20\text{--}100 \text{ kpc}$ (Belokurov et al. 2013). The geometry of the stream on the sky has been shown to require an oblate near-spherical halo (Ibata et al. 2001, Johnston et al. 2005), whereas LOS velocities favor a prolate shape (Helmi 2004). Thus Law & Majewski (2010) proposed a triaxial halo model for the Milky Way that is in fact

r_{vir} : Galactic virial radius, $282 \pm 30 \text{ kpc}$ (scaled to $\Omega_M = 0.3$)

M_{200} : Galactic mass within R_{200} , $1.1 \pm 0.3 \times 10^{12} M_\odot$

M_{vir} : Galactic virial mass, $1.3 \pm 0.3 \times 10^{12} M_\odot$

nearly oblate but with its short axis in the plane of the disk and with questionable stability. For this reason, most authors continue to use spherical models for the outer halo (Ibata et al. 2013, Gibbons et al. 2014).

On 20-kpc scales, Koposov et al. (2010) and Küpper et al. (2015) determined the flattening of the dark halo to be $q_z = 0.95 \pm 0.15$, i.e., essentially spherical, from modeling of the tidal streams of GD-1 and Pal 5. Loebman et al. (2012) claimed evidence for a strongly oblate shape from SDSS data. Kalberla et al. (2007) found evidence from HI data for a ring-like distribution of dark matter around $r \sim 15$ kpc. Near the Sun, the local shape of the dark matter halo is constrained by the ratio of the local dark matter density to the average enclosed spherical dark matter density (Garbari et al. 2012, Read 2014). Within large error bars the measurements are most consistent with a spherical or even prolate local halo shape (Garbari et al. 2012, Bovy & Rix 2013, Zhang et al. 2013), i.e., no dark disk (Read 2014). On the whole, constraints on the dark matter halo shape in the Milky Way are still weak, and no consistent picture has yet emerged.

6.4. Rotation Curve and Baryon Fraction Profile

Compared to the extended distribution of dark matter, the baryonic mass component in the Milky Way is centrally concentrated and dominates the mass in the central few kiloparsecs. In this section, we review the total circular velocity at R_0 and the rotation curve of the Milky Way, and then use illustrative dynamical models to estimate the contribution of stars and gas to the rotation curve, as well as the baryon fraction as a function of radius.

6.4.1. Solar tangential velocity. We recall from Section 3.4 the total angular velocity of the Sun, $\Omega_{g,\odot} = 30.24 \pm 0.12 \text{ km s}^{-1} \text{ kpc}^{-1}$, derived from the VLBI PM of Sgr A* in the Galactic Plane and the assumption that Sgr A* is at rest at the GC. For $R_0 = 8.2 \pm 0.1$ kpc (Section 3.2), the corresponding total solar tangential velocity is $V_{g,\odot} = 248 \pm 3 \text{ km s}^{-1}$. These values agree within errors with a number of independent recent measurements: Modeling trigonometric parallaxes and PMs of masers in HMSFR in the Galactic disk, Reid et al. (2014) derive $\Omega_{g,\odot} = 30.57 \pm 0.43 \text{ km s}^{-1} \text{ kpc}^{-1}$, giving $V_{g,\odot} = 251 \pm 5 \text{ km s}^{-1}$. The analysis of the nearby velocity field from SEGUE by Schönrich (2012), at fixed $R_0 = 8.2$ kpc, results in $V_{g,\odot} = 248 \pm 6 \text{ km s}^{-1}$. Bovy et al. (2012a) determine $V_{g,\odot} = 242^{+10}_{-3} \text{ km s}^{-1}$ from APOGEE data, whereas Sharma et al. (2014) obtain $V_{g,\odot} = 244 \text{ km s}^{-1}$ from fitting RAVE data. Here, we interpolated to $R_0 = 8.2$ kpc and estimate a systematic error of $\sim 5 \text{ km s}^{-1}$ from their results. Küpper et al. (2015) find $V_{g,\odot} = 254 \pm 16 \text{ km s}^{-1}$ from modeling the tidal stream of Pal 5. In what follows, we use $V_{g,\odot} = 248 \pm 3 \text{ km s}^{-1}$ from the PM of Sgr A*.

6.4.2. Circular velocity at R_0 . In an axisymmetric Galaxy, the circular velocity Θ_0 is simply related to $V_{g,\odot} = (\Theta_0 + V_\odot)$. Here V_\odot is the Sun's peculiar velocity along the direction of rotation with respect to the LSR, with the LSR defined as the streaming velocity of local stellar populations relative to the Sun in the limit of vanishing velocity dispersion (e.g., Schönrich et al. 2010). In Section 5.3.3, we estimated $V_\odot = 10.5 \pm 1.5 \text{ km s}^{-1}$. In our barred Galaxy, the LSR could itself have an additional streaming velocity V_{LSR} relative to the circular velocity in the axisymmetrically averaged gravitational potential (the RSR, see Section 5.3.3), due to perturbations from the bar and spiral arms. As discussed in Section 5.3.3, our estimate for the total LSR streaming velocity is $|\mathbf{v}_{\text{str}}| = 0^{+15} \text{ km s}^{-1}$, which could mostly be directed in the forward direction of rotation. If we take $V_{\text{LSR}} = \pm |\mathbf{v}_{\text{str}}| = 0 \pm 15 \text{ km s}^{-1}$, $V_{g,\odot}$ and Θ_0 are now related by $V_{g,\odot} = (\Theta_0 + V_{\text{LSR}} + V_\odot)$; this results in $\Theta_0 = 238 \pm 15 \text{ km s}^{-1}$ and $\Omega_0 = \Theta_0/R_0 = 29.0 \pm 1.8 \text{ km s}^{-1} \text{ kpc}^{-1}$.

$V_{g,\odot} = \Theta_0 + V_{\text{LSR}} + V_\odot$: the Sun's total tangential velocity relative to Sgr A*, $248 \pm 3 \text{ km s}^{-1}$

V_{LSR} : tangential velocity of the local standard of rest relative to the rotational standard of rest, $0 \pm 15 \text{ km s}^{-1}$

Θ_0 : circular rotation velocity at the Sun, $238 \pm 15 \text{ km s}^{-1}$

Ω_0 : circular orbit frequency at the Sun, $29.0 \pm 1.8 \text{ km s}^{-1} \text{ kpc}^{-1}$

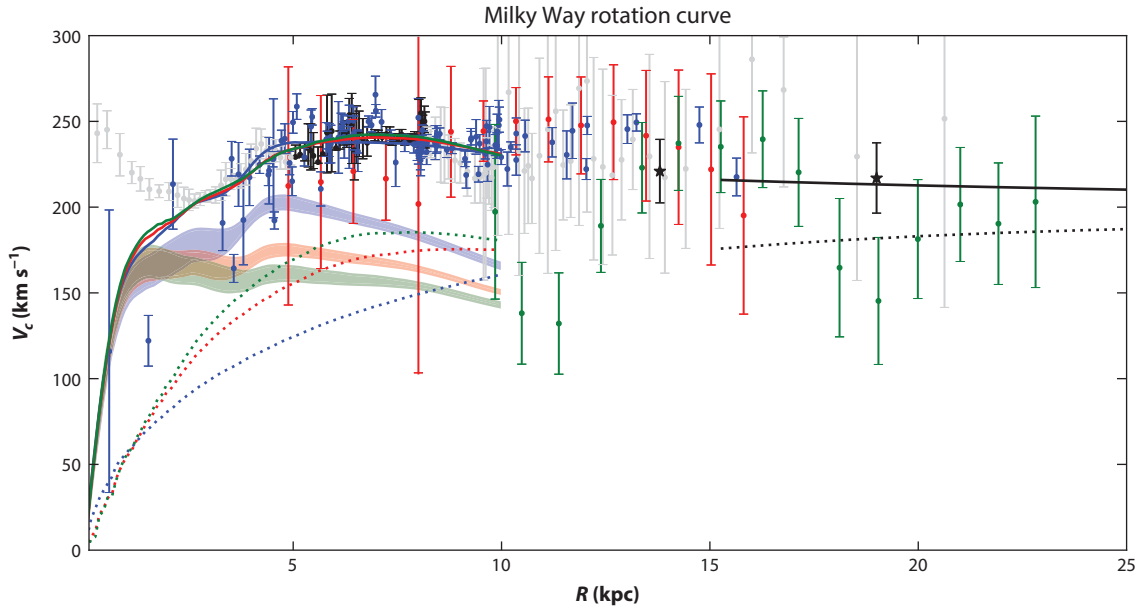


Figure 16

Galactic rotation curve. Sources for data points are: maser proper motions (PMs) and radial velocities (RVs) associated with high-mass disk stars (Reid et al. 2014, *blue*), inner Galaxy terminal velocities and outer disk velocities collected by Sofue et al. [2009, *black* ($5 \text{ kpc} < R < R_0$) and *gray* (elsewhere)], PMs of disk red clump giants (RCGs) from López-Corredoira (2014, *red*), Jeans-equation converted RV data for blue horizontal branch (BHB) stars (Kafle et al. 2012, *green*), and stream modeling for GD-1 and Pal-5 (Koposov et al. 2010 and Küpper et al. 2015, *black stars*). All data were approximately converted to ($R_0 = 8.2 \text{ kpc}$, $\Theta_0 = 238 \text{ km s}^{-1}$). The colored bands show azimuthally averaged circular velocities for illustrative dynamical models with bulge, long bar, disk, and dark halo (Portail et al. 2016). In the bulge region, these models are based on stellar kinematic data (Portail et al. 2015b) and thus are more reliable than the (misleading) terminal velocities. The bulge and long bar stellar mass in these models corresponds to a Kroupa IMF $\pm 10\%$, whereas the disk has fixed local stellar surface density $38 \text{ M}_\odot \text{ pc}^{-2}$ and scale length $R_d = (2.15, 2.6, 3.0) \text{ kpc}$ (*blue, red, green*, respectively) and includes a gas disk with surface density $13 \text{ M}_\odot \text{ pc}^{-2}$ and twice the stellar scale length. In each case, the lower band shows the rotation curve from the baryonic component, the dotted line shows the median dark halo profile, and the upper band shows the total rotation curve. In these models, the baryonic component provides (86%, 73%, 65%) of the circular velocity at $2.2 R_d$. The outer dotted and full lines show the rotation curves for a Navarro, Frenk & White (NFW) halo with virial mass $M_{\text{vir}} = 1.3 \times 10^{12} \text{ M}_\odot$ (Section 6.3) and concentration $c = 16$, which matches with the inner halo at $R \simeq 12 \text{ kpc}$, and for this NFW halo combined with the $R_d = 2.6 \text{ kpc}$ disk.

Traditionally, Oort's constants A and B were defined for the local disk as a means to estimate the circular velocity $\Theta_0(R_0)$ and its gradient from RV and PM data for nearby stellar populations, viz., $A - B = \Theta_0/R_0$; $A + B = -(\partial\Theta_0/\partial R)_{R_0}$. The quantity $A - B$ has been measured by many authors for different stellar populations (Feast & Whitelock 1997, Uemura et al. 2000, Elias et al. 2006) with values in the range of $27\text{--}32 \text{ km s}^{-1} \text{ kpc}^{-1}$. For the rotation gradient $-(A + B)$, different authors find positive, zero, and negative values. Catena & Ullio (2010) argue for $A + B = 0.18 \pm 0.47 \text{ km s}^{-1} \text{ kpc}^{-1}$ from an SDSS study of M stars (Fuchs et al. 2009).

6.4.3. Rotation curve. Figure 16 assembles rotation velocity measurements from various sources as explained in the caption. The data indicate a nearly flat rotation curve in the range $R = 5\text{--}13 \text{ kpc}$ (Reid et al. 2014) with a slight decrease at larger radii (Kafle et al. 2012, Küpper et al. 2015). PM data from *Gaia* will clarify this. The rotation velocities determined by Sofue et al. (2009, see also original references therein) from terminal velocities and a circular rotation model are unreliable

in the region dominated by the Galactic bar (e.g., Englmaier & Gerhard 1999, Fux 1999), as is clearly visible in the central ~ 3 kpc. Points inside $R = 5$ kpc (the half-length of the Galactic bar, Section 4.3) are therefore plotted in light shade.

Is the disk maximal? As shown with the illustrative models in **Figure 16**, the answer to this question largely depends on the disk (mass) scale length. These models include a bulge with dynamical mass fitted to the BRAVA kinematic data and stellar mass corresponding to a Kroupa IMF with $\pm 10\%$ margins (Portail et al. 2015b). The disk has local stellar surface density of $38 M_{\odot}/\text{pc}^2$ (Bovy & Rix 2013) and scale lengths $R_d = 2.15$ kpc (Bissantz & Gerhard 2002, Bovy & Rix 2013), 2.6 kpc (Robin et al. 2003, Jurić et al. 2008), and 3.0 kpc (Kent et al. 1991, Gould et al. 1996) and includes a gas disk with surface density of $13 M_{\odot}/\text{pc}^2$ and twice the stellar scale length. A short scale length R_d has important implications: The Galaxy’s disk (summed over all stellar and gaseous components) is then maximal (Sackett 1997) in the sense that the disk and bulge dominate the rotation curve, i.e., contribute 85% of the rotational velocity and $\sim 70\%$ of the rotational support at $2.2R_d$. We included the bulge in the definition here because it mostly originates from the disk (Section 4.2). For the three scale lengths shown, the baryonic component provides a median fraction $f_v = (86\%, 73\%, 65\%)$ of the circular velocity and (74%, 53%, 42%) of the radial force at $2.2R_d$. Thus the Milky Way’s disk is maximal only for the shortest scale length (see also Sackett 1997, Gerhard 1999, Bovy & Rix 2013, Piffl et al. 2014a), but even for the longer R_d its contribution to the rotational velocity is at the upper limit of that inferred for typical spiral galaxies by Martinsson et al. (2013, $f_v = 0.4\text{--}0.7$; but see Aniyani et al. 2016).

6.4.4. Baryonic mass fraction with radius. The dynamical models shown in **Figure 16** have median total stellar masses of $(5.7, 5.0, 4.7) \times 10^{10} M_{\odot}$. Of this, the stellar mass of the bulge and the disk embedded in the bulge region is $\sim 1.5 \times 10^{10} M_{\odot}$. The remaining mass is consistent with the total disk mass given in Section 5, if we consider the mass of the long bar ($\sim 1 \times 10^{10} M_{\odot}$) as part of the disk mass. Thus our estimate of the total stellar mass in the Milky Way is $M_{\star} = 5 \pm 1 \times 10^{10} M_{\odot}$. Adding the mass in cold gas and the $2.9 \times 10^{10} M_{\odot}$ (this model has higher mass than those in Section 6.2) in hot gas resulting from Tepper-Garcia et al. (2015) for the NFW halo shown in **Figure 16** ($M_{\text{vir}} = 1.3 \times 10^{12} M_{\odot}$, Section 6.3; $c = 16$), the total baryonic mass fraction of the Galaxy becomes again 0.07 ± 0.01 . The resulting total baryonic mass fraction within radius r from stars, cold gas, and hot gas is shown in **Figure 17**.

M_{\star} : total stellar mass
in the Galaxy,
 $5 \pm 1 \times 10^{10} M_{\odot}$

7. CONCLUDING REMARKS

The ultimate goal of Galactic research is to understand how the Milky Way has evolved from cosmological initial conditions to its present state and how its future evolution will proceed. Our first task is to describe its current state in some detail; this allows us to connect to similar galaxies nearby and to studies of galaxies at high redshift. Characterizing the Galaxy’s dominant components and measuring their main parameters is an important step in this process.

The past few years have seen significant progress in several areas, driven by the impressive data from past and ongoing surveys such as SDSS, VVV, APOGEE, and RAVE. We now have a quantitative description of the b/p structure of the Galactic bulge and, to a lesser extent, of its continuation into the Galactic Plane, the long bar. We know that the thin and thick disks contain distinct sequences in abundance ratios and age. The velocity field in the disk near the Sun has been charted, and dynamical models have been developed to link these data self-consistently to the gravitational potential. In the Galactic halo, multiple satellites and substructures have been discovered, and density and velocity measurements have been made to beyond > 50 kpc. However, we still lack good understanding of, e.g., the radial scale length of the large-scale Galactic disk, the

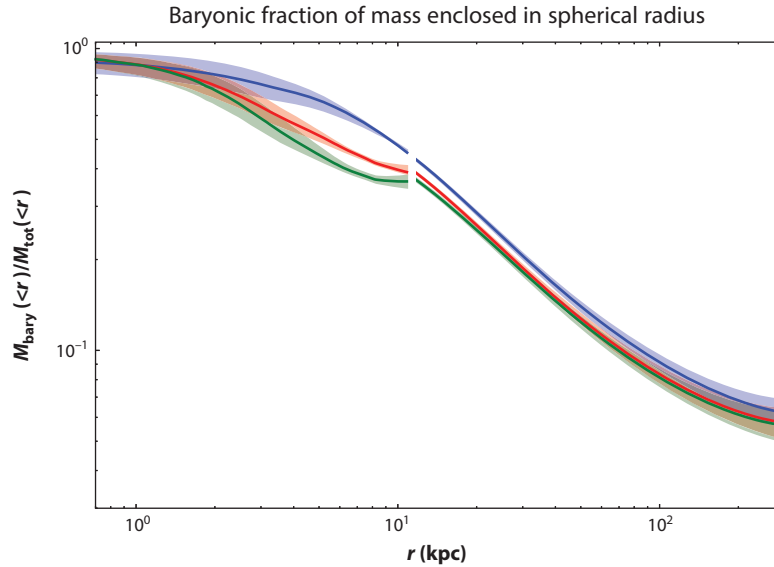


Figure 17

Fraction of baryonic mass within radius r including the stellar and cold gas mass from the dynamical models shown in **Figure 16** and the additional mass in hot gas predicted by *Tepper-Garcia et al. (2015)* with an assumed uncertainty of 35% (Section 6.2).

transition region between the Galactic bar and the surrounding disk, the properties of the nuclear disk, the mass of the stellar halo, and the outer rotation curve of the Milky Way. Constructing a complete structural model for the Milky Way is one of the main challenges for the coming years.

Half of all stars in the Universe formed before a redshift of unity. Detailed chemistry for millions of stars will provide important new information on the early formation of the different components. Until recently, most of our understanding of stars has come from the Solar Neighborhood, but high-resolution stellar surveys have now begun to reach more representative regions of the Galaxy. We still do not have a complete chemical inventory for any component over its full physical extent. In principle, such data for enough stars will enable chemical tagging of dynamically distinct subsystems. If even a few disrupted stellar systems with different ages can be recovered, we can learn about the role of secular evolution and stellar migration over cosmic time from their dispersal across the disk (*Bland-Hawthorn et al. 2010*). But accurate elemental abundances are hampered by the difficulty of measuring good stellar parameters (e.g., $\log g$, effective temperature). The differential abundance technique shows great promise, but this works best if the stars have a similar spectral type, thereby limiting the sample size. But we are encouraged by the revolution that is now under way to improve the state of the art in achieving consistent stellar abundances (*Jofré et al. 2014*, *Ness et al. 2015*).

We are looking forward to a golden age for Galactic research exemplified by ESA *Gaia*, the astrometric space mission that was successfully deployed at the end of 2013. The ongoing or upcoming deep all-sky photometric (DES, LSST, JWST, WFIRST), spectroscopic (APOGEE-2, GALAH, WEAVE, PFS, 4MOST), and seismological surveys (COROT, K2, TESS, PLATO) are well placed to advance our understanding of stellar populations. The large and extremely large telescopes will also play an important role, particularly with high-resolution spectroscopy (e.g., MOONS on VLT, G-CLEF on GMT).

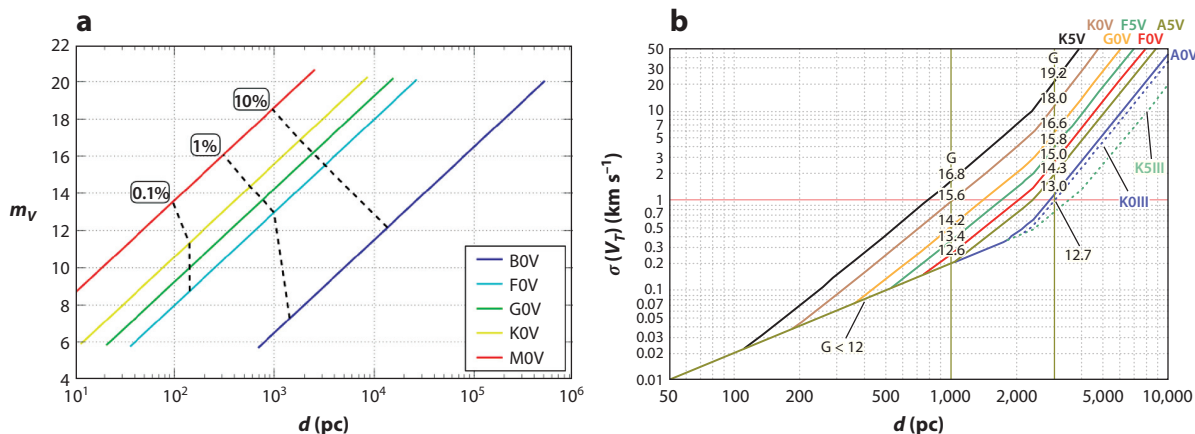


Figure 18

(a) The distance accuracy of *Gaia* for dwarf stars: the 0.1%, 1%, and 10% “accuracy horizons” are shown as dashed lines as a function of V magnitude. The different dwarf types are indicated by colored lines. This figure is made with the *PyGaia* package developed by A.G.M. Brown. Adapted from Read (2014) with permission. (b) The accuracy in the *Gaia* transverse velocity for dwarf stars as a function of their distance; the uncertainties arise from errors in both the proper motions and parallaxes. Adapted from Mignard (2011) with permission.

The LSST co-added survey will reach up to four magnitudes deeper than SDSS: For stars with $0.2 < g - r < 0.6$ and $g < 23.5$, LSST will achieve a metallicity error of 0.1 dex for metal-rich stars and 0.2 dex for metal-poor stars for about 200 million F/G main-sequence stars (Ivezić et al. 2008). In a single exposure, LSST will detect metal-poor MSTO stars to ~ 140 kpc and HB and RR Lyrae stars to ~ 500 kpc, going several times further in the final co-added data. LSST will also provide PM measurements and parallaxes for stars below $r \sim 20$, where *Gaia* lacks sensitivity (Ivezić et al. 2012). This will revolutionize photometric parallax and metallicity studies such as those reviewed in Section 5.

The *Gaia* astrometric mission will be even more far reaching for Galactic research. *Gaia* will have an enormous impact on our understanding of 6D phase space (\mathbf{x}, \mathbf{v}) for the stars, particularly in the near field, but with important new information for giants extending into the outer halo. By the end of the decade, *Gaia* will have obtained positions and velocities for up to two billion stars, i.e., phase space information for a few percent of stars that dominate the visible light in the Galaxy. In **Figure 18a**, many F/G dwarfs to be observed by LSST will have distances and PMs with 10% accuracy out to ~ 3 kpc from the Sun. Moreover, in **Figure 18b**, dwarfs brighter than $V \sim 15$ will have transverse velocities at least as good as the measured RVs. Such precise 6D phase space information will allow us to unravel the complex chemistry and dynamics of the local disk components to unprecedented levels.

Putting all the different strands together is not going to be easy. Increasingly sophisticated dynamical methods will be needed to accommodate the 6D phase-space information in a complex multicomponent potential and to combine this with the chemical information $\mathcal{C}([\text{Fe}/\text{H}], [\alpha/\text{Fe}], \dots)$, but good progress is already being made (Hunt & Kawata 2014, Sanders & Binney 2015). Eventually, we will need to consider the departures from dynamical equilibrium that arise from internal evolution and interactions with the outside (Binney 2013).

The Galaxy resembles a complex organism that evolves in a self-regulated fashion according to the laws of gravity, star formation, dynamics, and chemical evolution while subject to mass accretion and external influences from its cosmological neighborhood. Its low gas content, position

in the green valley of the color-magnitude diagram, and secularly evolved central parts of old stars indicate that it is in its late stages of evolution.

N-body and hydrodynamic simulations are becoming increasingly useful to help understand both formation and evolutionary processes (Stinson et al. 2013, Minchev et al. 2014, Scannapieco et al. 2015, Feng et al. 2016). These simulations will need to continue to grow in size to resolve smaller particle masses in both gas and dark matter and to ultimately resolve individual star clusters. More thought must be given to how we “evaluate” the goodness of fit of a complex dynamical model, or a numerical simulation, when comparing with the high-dimensional data space available to Galactic researchers (Sharma et al. 2011). Through these comparisons Galactic studies will improve galaxy-formation simulations and lead to an improved understanding of galaxy-formation processes in general.

Ultimately, we may never arrive at a complete understanding of the Galaxy, much like any complex physical system. Most often, we learn about the physical laws through a series of approximations that become progressively more refined. But our search for understanding is noble all the same as we seek answers to the many wonders around us.

DISCLOSURE STATEMENT

The authors are not aware of any affiliations, memberships, funding, or financial holdings that might be perceived as affecting the objectivity of this review.

ACKNOWLEDGMENTS

The initial idea for a review on the Galaxy’s global and structural parameters came from John Kormendy. It has been challenging to write not least because this is a vibrant and dynamic field of research, and major uncertainties still exist. But our motto throughout—keep calm and carry on—has sustained us even when at times no clear picture has emerged. Inevitably, with imposed page limits, there are missing topics and references for which we apologize in advance. We thank our referee Tim Beers for his oversight of the review, and Ken Freeman, Rosie Wyse, and James Binney for their historical perspective, wisdom, and insight. We are indebted to various colleagues for their support and help with figures and tables: C. Correa, P. Kafle, T. Licquia, F. Mignard, Y. Momany, M. Portail, J. Read, T. Tepper-Garcia, D. Webster, and C. Wegg; and for additional advice, perspectives, and comments: M. Arnaboldi, B. Benjamin, T. Bensby, J. Bovy, M. Boylan-Kolchin, R. Drimmel, S. Gillessen, Z. Ivezić, R. Lange, P. McMillan, D. Nataf, M. Reid, R. Schödel, and R. Schönrich. J.B.H. acknowledges the Kavli Institute, UC Santa Barbara, for their hospitality during the early planning of this review. J.B.H. is supported by an Australian Research Council Australian Laureate Fellowship. O.G. is grateful for the support of the Max Planck Institute for Extraterrestrial Physics and acknowledges a visiting fellowship from the Hunstead Fund for Astrophysics at the University of Sydney and the hospitality of the Mount Stromlo Observatory during the final stages of the review.

LITERATURE CITED

- Abadi MG, Navarro JF, Fardal M, Babul A, Steinmetz M. 2010. *MNRAS* 407:435
Abadi MG, Navarro JF, Steinmetz M. 2006. *MNRAS* 365:747
Adibekyan VZ, Santos NC, Sousa SG, et al. 2012. *Astron. Astrophys.* 543:89
Aguerri JAL, Debattista VP, Corsini EM. 2003. *MNRAS* 338:465
Aguerri JAL, Méndez-Abreu J, Falcón-Barroso J, et al. 2015. *Astron. Astrophys.* 576:A102

- Aihara H, Allende Prieto C, An D, et al. 2011. *Ap. J. Suppl.* 193:29
- Alard C. 2001. *Astron. Astrophys.* 379:L44
- Allende Prieto C, Majewski S, Schiavon R, et al. 2008. *Astron. Nachr.* 329:1018
- Allgood B, Flores R, Primack J, et al. 2006. *MNRAS* 367:1781
- Alves-Brito A, Meléndez J, Asplund M, Ramírez I, Yong D. 2010. *Astron. Astrophys.* 513:A35
- Anderson M, Bregman J. 2010. *Ap. J.* 714:320
- Anderson M, Bregman J. 2011. *Ap. J.* 737:22
- Anguiano B, Zucker DB, Scholz RD, et al. 2015. *MNRAS* 451:1229
- Aniyan S, Freeman KC, Gerhard OE, Arnaboldi M, Flynn C. 2016. *MNRAS* 456:1484
- Antoja T, Helmi A, Dehnen W, et al. 2014. *Astron. Astrophys.* 563:A60
- Antonini F, Capuzzo-Dolcetta R, Mastrobuono-Battisti A, Merritt D. 2012. *Ap. J.* 750:111
- Árnadóttir AS, Feltzing S, Lundström I. 2009. In *The Galaxy Disk in Cosmological Context, Proc. LAU Symp. Colloq.* 254, ed. J Andersen, B Nordström, J Bland-Hawthorn, p. 5. Cambridge, UK: Cambridge Univ. Press
- Athanassoula E. 1992. *MNRAS* 259:328
- Athanassoula E. 2005. *MNRAS* 358:1477
- Aumer M, Binney JJ. 2009. *MNRAS* 397:1286
- Aumer M, Schönrich R. 2015. *MNRAS* 454:3166
- Babusiaux C, Gilmore G. 2005. *MNRAS* 358:1309
- Babusiaux C, Gómez A, Hill V, et al. 2010. *Astron. Astrophys.* 519:A77
- Bahcall J, Soneira R. 1980. *Ap. J. Suppl.* 44:73
- Bailin J, Kawata D, Gibson B, et al. 2005. *Ap. J. Lett.* 627:L17
- Bajkova AT, Bobylev VV. 2015. *Baltic Astron.* 24:43
- Balick B, Brown RL. 1974. *Ap. J.* 194:265
- Bartko H, Martins F, Fritz TK, et al. 2009. *Ap. J.* 697:1741
- Battaglia G, Helmi A, Morrison H, et al. 2005. *MNRAS* 364:433
- Beaulieu SF, Freeman KC, Kalnajs AJ, Saha P, Zhao H. 2000. *Astron. J.* 120:855
- Becklin EE, Neugebauer G. 1968. *Ap. J.* 151:145
- Beers TC, Carollo D, Ivezić Ž, et al. 2012. *Ap. J.* 746:34
- Bell EF, Zucker DB, Belokurov V, et al. 2008. *Ap. J.* 680:295
- Beloborodov AM, Levin Y, Eisenhauer F, et al. 2006. *Ap. J.* 648:405
- Belokurov V, Evans NW, Bell EF, et al. 2007. *Ap. J. Lett.* 657:L89
- Belokurov V, Koposov SE, Evans NW, et al. 2013. *MNRAS* 437:116
- Belokurov V, Zucker DB, Evans NW, et al. 2006. *Ap. J. Lett.* 642:L137
- Benjamin R, Churchwell E, Babler B, et al. 2005. *Ap. J. Lett.* 630:L149
- Bensby T. 2014. *Astron. Astrophys.* 562:A71
- Bensby T, Alves-Brito A, Oey M, Yong D, Meléndez J. 2010. *Astron. Astrophys.* 516:L13
- Bensby T, Alves-Brito A, Oey M, Yong D, Meléndez J. 2011. *Ap. J. Lett.* 735:L46
- Bensby T, Feltzing S, Lundström I. 2003. *Astron. Astrophys.* 410:527
- Bensby T, Johnson J, Cohen J, et al. 2009. *Astron. Astrophys.* 499:737
- Bensby T, Oey M, Feltzing S, Gustafsson B. 2007. *Ap. J. Lett.* 655:L89
- Bensby T, Yee J, Feltzing S, et al. 2013. *Astron. Astrophys.* 549:A147
- Benson A, Bower R, Frenk C, et al. 2003. *Ap. J.* 599:38
- Bica E, Bonatto C, Barbay B, Ortolani S. 2006. *Astron. Astrophys.* 450:105
- Bienayme O, Robin A, Creze M. 1987. *Astron. Astrophys.* 180:94
- Binney J. 2010. *MNRAS* 401:2318
- Binney J. 2012. *MNRAS* 426:1328
- Binney J. 2013. *New Astron. Rev.* 57:29
- Binney J, Burnett B, Kordopatis G, et al. 2014. *MNRAS* 439:1231
- Binney J, Gerhard O, Spergel D. 1997. *MNRAS* 288:365
- Binney J, Gerhard OE, Stark AA, Bally J, Uchida KI. 1991. *MNRAS* 252:210
- Binney J, McMillan P. 2011. *MNRAS* 413:1889
- Binney J, Piffl T. 2015. *MNRAS* 454:3653

- Bird SA, Flynn C. 2015. *MNRAS* 452:2675
- Bissantz N, Englmaier P, Gerhard O. 2003. *MNRAS* 340:949
- Bissantz N, Gerhard O. 2002. *MNRAS* 330:591
- Blaauw A, Gum CS, Pawsey JL, Westerhout G. 1959. *Ap. J.* 130:702
- Blaauw A, Gum CS, Pawsey JL, Westerhout G. 1960. *MNRAS* 121:123
- Bland-Hawthorn J, Cohen M. 2003. *Ap. J.* 582:246
- Bland-Hawthorn J, Krumholz M, Freeman K. 2010. *Ap. J.* 713:166
- Bland-Hawthorn J, Vlajić M, Freeman K, Draine B. 2005. *Ap. J.* 629:239
- Blanton M, Moustakas J. 2009. *Annu. Rev. Astron. Astrophys.* 47:159
- Blanton M, Roweis S. 2007. *Astron. J.* 133:734
- Blitz L, Robishaw T. 2000. *Ap. J.* 541:675
- Bobylev VV. 2013. *Astron. Lett.* 39:95
- Böker T. 2010. In *Star Clusters: Basic Galactic Building Blocks Throughout Time and Space, Proc. IAU Symp. 266*, ed. R de Grijs, JRD Lépine, 5:58–63. Cambridge, UK: Cambridge Univ. Press
- Bonaca A, Jurić M, Ivezić Ž, et al. 2012. *Astron. J.* 143:105
- Bond NA, Ivezić Ž, Sesar B, et al. 2010. *Ap. J.* 716:1
- Bottema R. 1993. *Astron. Astrophys.* 275:16
- Bovy J, Allende Prieto C, Beers TC, et al. 2012a. *Ap. J.* 759:131
- Bovy J, Bird JC, Pérez AEG, et al. 2015. *Ap. J.* 800:83
- Bovy J, Rix HW. 2013. *Ap. J.* 779:115
- Bovy J, Rix HW, Hogg DW. 2012b. *Ap. J.* 751:131
- Bovy J, Rix HW, Liu C, et al. 2012c. *Ap. J.* 753:148
- Bovy J, Tremaine S. 2012. *Ap. J.* 756:89
- Bower GC, Falcke H, Herrnstein RM, et al. 2004. *Science* 304:704
- Bregman J, Lloyd-Davies E. 2007. *Ap. J.* 669:990
- Brook C, Stinson G, Gibson B, et al. 2012. *MNRAS* 426:690
- Bryan GL, Norman ML. 1998. *Ap. J.* 495:80
- Buchholz RM, Schödel R, Eckart A. 2009. *Astron. Astrophys.* 499:483
- Bullock JS, Johnston KV. 2005. *Ap. J.* 635:931
- Bureau M, Aronica G, Athanassoula E, et al. 2006. *MNRAS* 370:753
- Burnett B, Binney J, Sharma S, et al. 2011. *Astron. Astrophys.* 113:14
- Burton WB. 1988. In *Galactic and Extragalactic Radio Astronomy*, ed. GL Verschuur, KI Kellerman, pp. 295–358. Berlin, New York: Springer. 2nd ed.
- Cabrera-Lavers A, Garzón F, Hammersley P. 2005. *Astron. Astrophys.* 433:173
- Cabrera-Lavers A, González-Fernández C, Garzón F, Hammersley P, López-Corredoira M. 2008. *Astron. Astrophys.* 491:781
- Cabrera-Lavers A, Hammersley P, González-Fernández C, et al. 2007. *Astron. Astrophys.* 465:825
- Calamida A, Sahu KC, Casertano S, et al. 2015. *Ap. J.* 810:8
- Cao L, Mao S, Nataf D, Rattenbury NJ, Gould A. 2013. *MNRAS* 434:595
- Carney B, Seitzer P. 1993. *Astron. J.* 105:2127
- Carollo D, Beers TC, Lee YS, et al. 2007. *Nature* 450:1020
- Carraro G. 2015. *Bull. Assoc. Argent. Astron.* 57:7
- Carraro G, Vázquez RA, Costa E, Perren G, Moitinho A. 2010. *Ap. J.* 718:683
- Casagrande L, Schönrich R, Asplund M, et al. 2011. *Astron. Astrophys.* 530:A138
- Catelan M, Pritzl BJ, Smith HA. 2004. *Ap. J. Suppl.* 154:633
- Catena R, Ullio P. 2010. *J. Cosmol. Astropart. Phys.* 2010:4
- Cautun M, Frenk CS, van de Weygaert R, Hellwing WA, Jones BJT. 2014. *MNRAS* 445:2049
- Chabrier G. 2003. *Publ. Astron. Soc. Pac.* 115:763
- Chakrabarty D. 2007. *Astron. Astrophys.* 467:145
- Chatzopoulos S, Fritz TK, Gerhard O, et al. 2015. *MNRAS* 447:948
- Chen B, Figueras F, Torra J, et al. 1999. *Astron. Astrophys.* 352:459
- Chen B, Stoughton C, Smith JA, et al. 2001. *Ap. J.* 553:184
- Cheng J, Rockosi C, Morrison H, et al. 2012. *Ap. J.* 752:51

- Chomiuk L, Povich M. 2011. *Astron. J.* 142:197
- Clarkson W, Sahu K, Anderson J, et al. 2008. *Ap. J.* 684:1110
- Combes F, Debbasch F, Friedli D, Pfenniger D. 1990. *Astron. Astrophys.* 233:82
- Comerón S, Elmegreen, BG, Salo H, et al. 2012. *Ap. J.* 759:98
- Conti PS, Vacca WD. 1990. *Astron. J.* 100:431
- Contopoulos G. 1980. *Astron. Astrophys.* 81:198
- Cooper AP, Cole S, Frenk CS, et al. 2010. *MNRAS* 406:744
- Cooper AP, Parry OH, Lowing B, Cole S, Frenk C. 2015. *MNRAS* 454:3185
- Correa C, Wyithe J, Schaye J, Duffy A. 2015. *MNRAS* 452:1217
- Cox T, Loeb A. 2008. *MNRAS* 386:461
- Crain R, McCarthy I, Frenk C, Theuns T, Schaye J. 2010. *MNRAS* 407:1403
- Cravens T, Robertson I, Snowden S. 2001. *J. Geophys. Res.* 106:24883
- Cuddeford P, Amendt P. 1992. *MNRAS* 256:166
- Dambis AK. 2009. *MNRAS* 396:553
- de Bruijne J, Allen M, Azaz S, et al. 2015. *Astron. Astrophys.* 576:A74
- De Lucia G. 2012. *Astron. Nachr.* 333:460
- De Lucia G, Helmi A. 2008. *MNRAS* 391:14
- de Rossi M, Tissera P, De Lucia G, Kauffmann G. 2009. *MNRAS* 395:210
- De Silva GM, Freeman KC, Bland-Hawthorn J, et al. 2015. *MNRAS* 449:2604
- de Vaucouleurs G. 1983. *Ap. J.* 268:468
- de Vaucouleurs G, Pence W. 1978. *Astron. J.* 83:1163
- Deason AJ, Belokurov V, Evans NW. 2011. *MNRAS* 416:2903
- Deason AJ, Belokurov V, Evans NW, An J. 2012. *MNRAS* 424:L44
- Deason AJ, Belokurov V, Evans NW, Johnston KV. 2013. *Ap. J.* 763:113
- Deason AJ, Belokurov V, Koposov SE, Rockosi CM. 2014. *Ap. J.* 787:30
- Debattista VP, Gerhard O, Sevenster MN. 2002. *MNRAS* 334:355
- Dehnen W. 1998. *Astron. J.* 115:2384
- Dehnen W. 2000. *Astron. J.* 119:800
- Dehnen W, Binney JJ. 1998. *MNRAS* 298:387
- Dehnen W, McLaughlin DE, Sachania J. 2006. *MNRAS* 369:1688
- Dékány I, Minniti D, Catelan M, et al. 2013. *Ap. J. Lett.* 776:L19
- Dékány I, Minniti D, Majaess D, et al. 2015. *Ap. J. Lett.* 812:L29
- Delhaye J. 1965. In *Galactic Structure*, Vol. 5: *Stars and Stellar Systems*, ed. A Blaauw, M Schmidt, pp. 61–84. Chicago & London: Univ. Chicago Press and Toronto, Can.: Univ. Toronto Press
- Deng LC, Newberg H, Liu C, et al. 2012. *Res. Astron. Astrophys.* 12:735
- Di Matteo P, Haywood M, Gómez A, et al. 2014. *Astron. Astrophys.* 567:A122
- Diplas A, Savage B. 1991. *Ap. J.* 377:126
- Do T, Martinez GD, Yelda S, et al. 2013. *Ap. J. Lett.* 779:L6
- Doeleman SS, Weintraub J, Rogers AEE, et al. 2008. *Nature* 455:78
- Drimmel R, Spergel D. 2001. *Ap. J.* 556:181
- Driver SP, Hill DT, Kelvin LS, et al. 2011. *MNRAS* 413:971
- Dubinski J, Carlberg R. 1991. *Ap. J.* 378:496
- Dwek E, Arendt R, Hauser M, et al. 1995. *Ap. J.* 445:716
- Eckart A, Genzel R. 1997. *MNRAS* 284:576
- Eckart A, Genzel R, Hofmann R, Sams BJ, Tacconi-Garman LE. 1995. *Ap. J. Lett.* 445:L23
- Edvardsson B, Andersen J, Gustafsson B, et al. 1993. *Astron. Astrophys.* 275:101
- Efremov Y. 2011. *Astron. Rep.* 55:108
- Eggen O. 1951. *Ap. J.* 113:657
- Eggen OJ, Lynden-Bell D, Sandage AR. 1962. *Ap. J.* 136:748
- Eisenhauer F, Schdel R, Genzel R, et al. 2003. *Ap. J. Lett.* 597:L121
- Elias F, Alfaro EJ, Cabrera-Caño J. 2006. *Astron. J.* 132:1052
- Ellis SC, Bland-Hawthorn J. 2007. *MNRAS* 377:815
- Englmaier P, Gerhard O. 1999. *MNRAS* 304:512

- Evans NW, Sanders JL, Williams AA, et al. 2016. *MNRAS* 456:4506
- Faccioli L, Smith MC, Yuan HB, et al. 2014. *Ap. J.* 788:105
- Fang T, Bullock J, Boylan-Kolchin M. 2013. *Ap. J.* 762:20
- Feast M, Whitelock P. 1997. *MNRAS* 291:683
- Feldmeier A, Neumayer N, Seth A, et al. 2014. *Astron. Astrophys.* 570:A2
- Feng Y, Di Matteo TD, Croft R, et al. 2015. *MNRAS* 455:2778
- Fermani F, Schönrich R. 2013. *MNRAS* 432:2402
- Finlator K, Ivezić Ž, Fan X, et al. 2000. *Astron. J.* 120:2615
- Flynn C, Holmberg J, Portinari L, Fuchs B, Jahreiß H. 2006. *MNRAS* 372:1149
- Font AS, Johnston KV, Bullock JS, Robertson BE. 2006. *Ap. J.* 638:585
- Font AS, McCarthy IG, Crain RA, et al. 2011. *MNRAS* 416:2802
- Forero-Romero JE, Hoffman Y, Bustamante S, Gottloeber S, Yepes G. 2013. *Ap. J.* 767:5
- Fox AJ, Wakker BP, Barger KA, et al. 2014. *Ap. J.* 787:147
- Francis C, Anderson E. 2014. *MNRAS* 441:1105
- Freeman K. 2001. In *Galaxy Disks and Disk Galaxies*, ed. JG Funes, EM Corsini. *ASP Conf. Ser.* 230:91. San Francisco: ASP
- Freeman K, Bland-Hawthorn J. 2002. *Annu. Rev. Astron. Astrophys.* 40:487
- Freudenreich HT. 1998. *Ap. J.* 492:495
- Fritz TK, Chatzopoulos S, Gerhard O, et al. 2016. *Ap. J.* 821:44
- Fritz TK, Gillessen S, Dodds-Eden K, et al. 2011. *Ap. J.* 737:73
- Fuchs B, Dettbarn C, Rix HW, et al. 2009. *Astron. J.* 137:4149
- Fuhrmann K. 1998. *Astron. Astrophys.* 330:626
- Fuhrmann K. 2008. *MNRAS* 384:173
- Fux R. 1999. *Astron. Astrophys.* 345:787
- Garbari S, Liu C, Read JI, Lake G. 2012. *MNRAS* 425:1445
- Gatto A, Fraternali F, Read J, et al. 2013. *MNRAS* 433:2749
- Genzel R, Eisenhauer F, Gillessen S. 2010. *Rev. Mod. Phys.* 82:3121
- Genzel R, Pichon C, Eckart A, Gerhard OE, Ott T. 2000. *MNRAS* 317:348
- Gerhard O, Martinez-Valpuesta I. 2012. *Ap. J. Lett.* 744:L8
- Gerhard OE. 1999. In *Galaxy Dynamics: A Rutgers Symposium*, ed. DR Merritt, M Valluri, JA Sellwood. *ASP Conf. Ser.* 182:307. San Francisco: ASP
- Ghez AM, Klein BL, Morris M, Becklin EE. 1998. *Ap. J.* 509:678
- Ghez AM, Salim S, Weinberg NN, et al. 2008. *Ap. J.* 689:1044
- Gibbons SLJ, Belokurov V, Evans NW. 2014. *MNRAS* 445:3788
- Gillessen S, Eisenhauer F, Fritz TK, et al. 2009a. *Ap. J. Lett.* 707:L114
- Gillessen S, Eisenhauer F, Fritz TK, et al. 2013. In *Advancing the Physics of Cosmic Distances, Proc. IAU Symp.* 289, ed. R de Grijs, 8:29–35. Cambridge, UK: Cambridge Univ. Press
- Gillessen S, Eisenhauer F, Trippe S, et al. 2009b. *Ap. J.* 692:1075
- Gilmore G, Randich S, Asplund M, et al. 2012. *Messenger* 147:25
- Gilmore G, Reid N. 1983. *MNRAS* 202:1025
- Girardi L. 2016. *Annu. Rev. Astron. Astrophys.* 54:95–133
- Gnedin OY, Brown WR, Geller MJ, Kenyon SJ. 2010. *Ap. J. Lett.* 720:L108
- Gonzalez OA, Gadotti DA. 2016. In *Galactic Bulges*, ed. E Laurikainen, R Peletier, D Gadotti. *Ap. Space Sci. Lib.* 418:199–232. Cham, Switz.: Springer
- Gonzalez OA, Rejkuba M, Minniti D, et al. 2011a. *Astron. Astrophys.* 534:L14
- Gonzalez OA, Rejkuba M, Zoccali M, et al. 2011b. *Astron. Astrophys.* 530:A54
- Gonzalez OA, Rejkuba M, Zoccali M, et al. 2012. *Astron. Astrophys.* 543:A13
- Gonzalez OA, Rejkuba M, Zoccali M, et al. 2013. *Astron. Astrophys.* 552:A110
- Goodman AA, Alves J, Beaumont CN, et al. 2014. *Ap. J.* 797:53
- Gould A, Bahcall JN, Flynn C. 1996. *Ap. J.* 465:759
- Gratton R, Carretta E, Matteucci F, Sneden C. 2000. *Astron. Astrophys.* 358:671
- Grcevich J, Putman M. 2009. *Ap. J.* 696:385
- Groenewegen MAT, Blommaert JADL. 2005. *Astron. Astrophys.* 443:143

- Groenewegen MAT, Udalski A, Bono G. 2008. *Astron. Astrophys.* 481:441
- Guedes J, Mayer L, Carollo M, Madau P. 2013. *Ap. J.* 772:36
- Gupta A, Mathur S, Krongold Y, Nicastro F, Galeazzi M. 2012. *Ap. J. Lett.* 756:L8
- Habing H. 1988. *Astron. Astrophys.* 200:40
- Habing HJ, Sevenster MN, Messineo M, van de Ven G, Kuijken K. 2006. *Astron. Astrophys.* 458:151
- Hammer F, Puech M, Flores H, et al. 2012. *Eur. Phys. J. Web Conf.* 19:01004
- Hammersley P, Garzón F, Mahoney T, López-Corredoira M, Torres M. 2000. *MNRAS* 317:L45
- Harris WE. 2010. arXiv:1012.3224
- Hartmann D, Burton WB. 1997. *Atlas of Galactic Neutral Hydrogen*. 243 pp. Cambridge, UK: Cambridge Univ. Press
- Hawkins K, Jofre P, Masseron T, Gilmore G. 2015. *MNRAS* 453:758
- Hayden MR, Bovy J, Holtzman JA, et al. 2015. *Ap. J.* 808:132
- Haywood M. 2006. *MNRAS* 371:1760
- Haywood M, Matteo PD, Snaith O, Lehnert MD. 2015. *Astron. Astrophys.* 579:5
- Haywood M, Robin AC, Crézé M. 1997. *Astron. Astrophys.* 320:428
- Helmi A. 2004. *Ap. J. Lett.* 610:L97
- Helmi A. 2008. *Astron. Astrophys. Rev* 15:145
- Henley D, Shelton R. 2012. *Ap. J. Suppl.* 202:14
- Henley D, Shelton R, Kwak K, Joung M, Mac Low MM. 2010. *Ap. J.* 723:935
- Hill V, Lecureur A, Gómez A, et al. 2011. *Astron. Astrophys.* 534:A80
- Hinshaw G, Spergel D, Verde L, et al. 2003. *Ap. J. Suppl.* 148:135
- Holmberg J, Nordström B, Andersen J. 2007. *Astron. Astrophys.* 475:519
- Holmberg J, Nordström B, Andersen J. 2009. *Astron. Astrophys.* 501:941
- Honma M, Bushimata T, Choi YK, et al. 2007. *Publ. Astron. Soc. Jpn.* 59:889
- Honma M, Nagayama T, Ando K, et al. 2012. *Publ. Astron. Soc. Jpn.* 64:136
- Hopkins P, Kereš D, Oñorbe J, et al. 2014. *MNRAS* 445:581
- Humphreys RM, Larsen JA. 1995. *Astron. J.* 110:2183
- Hunt JAS, Kawata D. 2014. *MNRAS* 443:2112
- Ibata R, Lewis GF, Irwin M, Totten E, Quinn T. 2001. *Ap. J.* 551:294
- Ibata R, Lewis GF, Martin NF, Bellazzini M, Correnti M. 2013. *Ap. J. Lett.* 765:L15
- Ibata RA, Irwin M, Lewis G, Ferguson A, Tanvir N. 2003. *MNRAS* 340:L21
- Ibata RA, Wyse RFG, Gilmore G, Irwin MJ, Suntzeff NB. 1997. *Astron. J.* 113:634
- Irwin M, Ferguson A, Ibata R, Lewis G, Tanvir N. 2005. *Ap. J. Lett.* 628:L105
- Ivezić Ž, Beers TC, Jurić M. 2012. *Annu. Rev. Astron. Astrophys.* 50:251
- Ivezić Ž, Sesar B, Jurić M, et al. 2008. *Ap. J.* 684:287
- Jofré P, Heiter U, Soubiran C, et al. 2014. *Astron. Astrophys.* 564:A133
- Johnson CI, Rich MR, Fulbright JP, Valenti E, McWilliam A. 2011. *Ap. J.* 732:108
- Johnston KV, Law DR, Majewski SR. 2005. *Ap. J.* 619:800
- Jurić M, Ivezić Ž, Brooks A, et al. 2008. *Ap. J.* 673:864
- Just A, Jahreiß H. 2010. *MNRAS* 402:461
- Kafle PR, Sharma S, Lewis GF, Bland-Hawthorn J. 2012. *Ap. J.* 761:98
- Kafle PR, Sharma S, Lewis GF, Bland-Hawthorn J. 2014. *Ap. J.* 794:59
- Kalberla PMW, Dedes L. 2008. *Astron. Astrophys.* 487:951
- Kalberla PMW, Dedes L, Kerp J, Haud U. 2007. *Astron. Astrophys.* 469:511
- Kalnajs AJ. 1991. In *Dynamics of Disc Galaxies*, ed. B Sundelius, p. 323. Gothenburg: Göteborgs Univ.
- Kapteyn J. 1922. *Ap. J.* 55:302
- Kazantzidis S, Kravtsov A, Zentner A, et al. 2004. *Ap. J. Lett.* 611:L73
- Kent SM. 1992. *Ap. J.* 387:181
- Kent SM, Dame TM, Fazio G. 1991. *Ap. J.* 378:131
- Kerr FJ, Lynden-Bell D. 1986. *MNRAS* 221:1023
- Kimmig B, Seth A, Ivans II, et al. 2015. *Astron. J.* 149:53
- King C, Brown WR, Geller MJ, Kenyon SJ. 2015. *Ap. J.* 813:89
- Klypin A, Zhao H, Somerville RS. 2002. *Ap. J.* 573:597

- Kobayashi N, Yasui C, Tokunaga A, Saito M. 2008. *Ap. J.* 683:178
- Koposov SE, Rix HW, Hogg DW. 2010. *Ap. J.* 712:260
- Kordopatis G, Wyse RFG, Gilmore G, et al. 2015. *Astron. Astrophys.* 582:122
- Kormendy J. 2013. In *XXIII Canary Isl. Winter Sch. Astrophys.*, ed. J. Falcon-Barroso, JH Knapen, p. 1. Cambridge: Cambridge Univ. Press
- Kormendy J, Barentine JC. 2010. *Ap. J. Lett.* 715:L176
- Kormendy J, Drory N, Bender R, Cornell M. 2010. *Ap. J.* 723:54
- Kormendy J, Ho LC. 2013. *Annu. Rev. Astron. Astrophys.* 51:511
- Krabbe A, Genzel R, Eckart A, et al. 1995. *Ap. J.* 447:L95
- Kroupa P. 2001. *MNRAS* 322:231
- Kuijken K, Gilmore G. 1989. *MNRAS* 239:571
- Kunder A, Koch A, Rich R, et al. 2012. *Astron. J.* 143:57
- Kunder A, Rich RM, Koch A, Storm J, Nataf DM, et al. 2016. *Ap. J. Lett.* 821:L25
- Küpper AHW, Balbinot E, Bonaca A, et al. 2015. *Ap. J.* 803:80
- Lacy JH, Townes CH, Geballe TR, Hollenbach DJ. 1980. *Ap. J.* 241:132
- Lange R, Driver S, Robotham A, et al. 2015. *MNRAS* 447:2603
- Larsen JA, Humphreys RM. 2003. *Astron. J.* 125:1958
- Launhardt R, Zylka R, Mezger PG. 2002. *Astron. Astrophys.* 384:112
- Laurikainen E, Salo H, Athanassoula E, Bosma A, Herrera-Endoqui M. 2014. *MNRAS* 444:L80
- Laurikainen E, Salo H, Buta R, Knapen JH. 2011. *MNRAS* 418:1452
- Law DR, Majewski SR. 2010. *Ap. J.* 714:229
- Lewis JR, Freeman KC. 1989. *Astron. J.* 97:139
- Li YS, White SDM. 2008. *MNRAS* 384:1459
- Li ZY, Shen J. 2012. *Ap. J. Lett.* 757:L7
- Licquia TC, Newman JA. 2015. *Ap. J.* 806:96
- Licquia TC, Newman JA, Brinchmann J. 2015. *Ap. J.* 809(1):96
- Lindqvist M, Habing HJ, Winnberg A. 1992. *Astron. Astrophys.* 259:118
- Loebman SR, Ivezić Ž, Quinn TR, et al. 2012. *Ap. J. Lett.* 758:L23
- Loebman SR, Roskar R, Debattista VP, et al. 2011. *Ap. J.* 737:8
- Long RJ, Mao S, Shen J, Wang Y. 2012. *MNRAS* 428:3478
- López-Corredoira M. 2014. *Astron. Astrophys.* 563:A128
- López-Corredoira M, Cabrera-Lavers A, Garzón F, Hammersley P. 2002. *Astron. Astrophys.* 394:883
- López-Corredoira M, Cabrera-Lavers A, Gerhard O. 2005. *Astron. Astrophys.* 439:107
- Lowing B, Wang W, Cooper A, et al. 2014. *MNRAS* 446:2274
- Magrini L, Randich S, Donati P, et al. 2015. *Astron. Astrophys.* 580:A85
- Maíz-Apellániz J. 2001. *Astron. J.* 121:2737
- Majaess D. 2010. *Acta Astron.* 60:55
- Malhotra S, Spergel D, Rhoads J, Li J. 1996. *Ap. J.* 473:687
- Malkin Z. 2013. In *Advancing the Physics of Cosmic Distances, Proc. IAU Symp. 289*, ed. R de Grijs, 8:406–9. Cambridge, UK: Cambridge Univ. Press
- Martinez-Valpuesta I, Gerhard O. 2013. *Ap. J. Lett.* 766:L3
- Martinsson TPK, Verheijen MAW, Westfall KB, et al. 2013. *Astron. Astrophys.* 557:A131
- Masseron T, Gilmore G. 2015. *MNRAS* 453:1855
- Matsunaga N, Feast MW, Kawadu T, et al. 2013. *MNRAS* 429:385
- Matsunaga N, Kawadu T, Nishiyama S, et al. 2009. *MNRAS* 399:1709
- Matsunaga N, Kawadu T, Nishiyama S, et al. 2011. *Nature* 477:188
- May J, Bronfman L, Alvarez H, Murphy D, Thaddeus P. 1993. *Astron. Astrophys. Suppl.* 99:105
- McCarthy IG, Font AS, Crain RA, et al. 2012. *MNRAS* 420:2245
- McKee C, Williams J. 1997. *Ap. J.* 476:144
- McKee CF, Parravano A, Hollenbach DJ. 2015. *Ap. J.* 814:1
- McMillan PJ. 2011. *MNRAS* 414:2446
- McWilliam A, Zoccali M. 2010. *Ap. J.* 724:1491
- Mendez RA, van Altena WF. 1998. *Astron. Astrophys.* 330:910

- Merritt D. 2013. *Dynamics and Evolution of Galactic Nuclei*. Princeton, NJ: Princeton Univ. Press
- Merritt D, Berczik P, Laun F. 2007. *Astron. J.* 133:553
- Mignard F. 2011. ftp://ftp.oca.eu/pub/mignard/TN_Gaia/GAIA-CA-TN-OCA-FM-048.pdf
- Mihalas D, Binney J. 1981. *Galactic Astronomy: Structure and Kinematics*. San Francisco: WH Freeman
- Miller M, Bregman J. 2013. *Ap. J.* 770:118
- Miller M, Bregman J. 2015. *Ap. J.* 800:14
- Minchev I, Chiappini C, Martig M. 2014. *Astron. Astrophys.* 572:A92
- Minchev I, Famaey B. 2010. *Ap. J.* 722:112
- Minchev I, Martig M, Streich D, et al. 2015. *Ap. J. Lett.* 804:L9
- Minchev I, Nordhaus J, Quillen AC. 2007. *Ap. J. Lett.* 664:L31
- Minniti D, Lucas PW, Emerson JP, et al. 2010. *New Astron.* 15:433
- Minniti D, Saito R, Alonso-García J, Lucas P, Hempel M. 2011. *Ap. J. Lett.* 733:L43
- Molinari S, Bally J, Noriega-Crespo A, et al. 2011. *Ap. J. Lett.* 735:L33
- Momany Y, Zaggia S, Gilmore G, et al. 2006. *Astron. Astrophys.* 451:515
- Moni Bidin C, Carraro G, Méndez RA. 2012. *Ap. J.* 747:101
- Morris MR, Meyer L, Ghez AM. 2012. *Res. Astron. Astrophys.* 12:995
- Morrison HL. 1993. *Astron. J.* 106:578
- Munn J, Monet D, Levine S, et al. 2004. *Astron. J.* 127:3034
- Mutch SJ, Croton DJ, Poole GB. 2011. *Ap. J.* 736:84
- Nataf DM, Gould A, Fouqué P, et al. 2013. *Ap. J.* 769:88
- Nataf DM, Udalski A, Gould A, Fouqué P, Stanek K. 2010. *Ap. J. Lett.* 721:L28
- Nataf DM, Udalski A, Skowron J, et al. 2015. *MNRAS* 447:1535
- Ness M, Freeman K, Athanassoula E, et al. 2012. *Ap. J.* 756:22
- Ness M, Freeman K, Athanassoula E, et al. 2013a. *MNRAS* 430:836
- Ness M, Freeman K, Athanassoula E, et al. 2013b. *MNRAS* 432:2092
- Ness M, Hogg D, Rix HW, Ho A, Zasowski G. 2015. *Ap. J.* 808:16
- Newberg H, Yanny B, Rockosi C, et al. 2002. *Ap. J.* 569:245
- Nichols M, Bland-Hawthorn J. 2011. *Ap. J.* 732:17
- Nidever DL, Bovy J, Bird JC, et al. 2014. *Ap. J.* 796:38
- Niederste-Ostholt M, Belokurov V, Evans NW, Peñarrubia J. 2010. *Ap. J.* 712:516
- Nishiyama S, Nagata T, Baba D, et al. 2005. *Ap. J. Lett.* 621:L105
- Nishiyama S, Nagata T, Sato S, et al. 2006. *Ap. J.* 647:1093
- Nishiyama S, Nagata T, Tamura M, et al. 2008. *Ap. J.* 680:1174
- Nishiyama S, Yasui K, Nagata T, et al. 2013. *Ap. J. Lett.* 769:L28
- Nissen PE, Schuster WJ. 2011. *Astron. Astrophys.* 530:A15
- Nordström B, Mayor M, Andersen J, et al. 2004. *Astron. Astrophys.* 418:989
- Norris J, Ryan S. 1991. *Ap. J.* 380:403
- Nuza S, Parisi F, Scannapieco C, et al. 2014. *MNRAS* 441:2593
- Obreja A, Domínguez-Tenreiro R, Brook C, et al. 2013. *Ap. J.* 763:26
- Ojha DK. 2001. *MNRAS* 322:426
- Oort JH, Rougoor GW. 1960. *MNRAS* 121:171–73
- Ortolani S, Renzini A, Gilmozzi R, et al. 1995. *Nature* 377:701
- Paczynski B, Stanek KZ. 1998. *Ap. J. Lett.* 494:L219
- Paerels F, Kahn S. 2003. *Annu. Rev. Astron. Astrophys.* 41:291
- Pandey AK, Bhatt BC, Mahra HS. 1988. *Astron. Astrophys.* 189:66
- Parkinson H, Cole S, Helly J. 2008. *MNRAS* 383:557
- Pasetto S, Grebel EK, Zwitter T, et al. 2012. *Astron. Astrophys.* 547:A70
- Patterson FS. 1940. *Harv. Coll. Obs. Bull.* 914:9
- Paumard T, Genzel R, Martins F, et al. 2006. *Ap. J.* 643:1011
- Peebles P, Tully R. 2013. arXiv:1302.6982
- Perryman M, Spergel DN, Lindegren L. 2014. *Ap. J.* 789:166
- Pfenniger D, Friedli D. 1991. *Astron. Astrophys.* 252:75
- Pfuhl O, Fritz TK, Zilka M, et al. 2011. *Ap. J.* 741:108

- Piddington JH, Minnett HC. 1951. *Aust. J. Sci. Res.* A4:459
- Pietrukowicz P, Kozłowski S, Skowron J, et al. 2015. *Ap. J.* 811:113
- Piffl T, Binney J, McMillan PJ, et al. 2014a. *MNRAS* 445:3133
- Piffl T, Scannapieco C, Binney JJ, et al. 2014b. *Astron. Astrophys.* 562:A91
- Pila-Díez B, de Jong JTA, Kuijken K, van der Burg RFJ, Hoekstra H. 2015. *Astron. Astrophys.* 579:A38
- Pillepich A, Madau P, Mayer L. 2015. *Ap. J.* 799:184
- Pillepich A, Vogelsberger M, Deason A, et al. 2014. *MNRAS* 444:237
- Pipino A, Matteucci F, D’Ercole A. 2008. In *Formation and Evolution of Galaxy Bulges, Proc. IAU Symp. 245*, ed. M Bureau, E Athanassoula, B Barbuy, 3:19–22. Cambridge, UK: Cambridge Univ. Press
- Pohlen M, Trujillo I. 2006. *Astron. Astrophys.* 454:759
- Portail M, Wegg C, Gerhard O. 2015a. *MNRAS* 450:L66
- Portail M, Wegg C, Gerhard O, Martinez-Valpuesta I. 2015b. *MNRAS* 448:713
- Prada F, Klypin A, Simonneau E, et al. 2006. *Ap. J.* 645:1001
- Prochaska J, Naumov S, Carney B, McWilliam A, Wolfe A. 2000. *Astron. J.* 120:2513
- Putman M, Gibson B, Staveley-Smith L, et al. 1998. *Nature* 394:752
- Quillen A, Garnett D. 2001. In *Galaxy Disks and Disk Galaxies*, ed. JG Funes, EM Corsini. *ASP Conf. Ser.* 230:87. San Francisco: ASP
- Raha N, Sellwood JA, James RA, Kahn FD. 1991. *Nature* 352:411
- Rattenbury NJ, Mao S, Sumi T, Smith MC. 2007. *MNRAS* 378:1064
- Read JI. 2014. *J. Phys. G. Nucl. Part. Phys.* 41:63101
- Reddy B, Lambert D, Allende Prieto C. 2006. *MNRAS* 367:1329
- Reddy B, Tomkin J, Lambert D, Allende Prieto C. 2003. *MNRAS* 340:304
- Reid MJ. 1993. *Annu. Rev. Astron. Astrophys.* 31:345
- Reid MJ. 2008. In *A Giant Step: From Milli- to Micro- Arcsecond Astrometry, Proc. IAU Symp. 248*, ed. W Jin, I Platais, MAC Perryman, 3:141–47. Cambridge, UK: Cambridge Univ. Press
- Reid MJ. 2009. *Int. J. Mod. Phys. D* 18:889
- Reid MJ, Brunthaler A. 2004. *Ap. J.* 616:872
- Reid MJ, Menten KM, Brunthaler A, et al. 2014. *Ap. J.* 783:130
- Reid MJ, Menten KM, Genzel R, et al. 2003. *Ap. J.* 587:208
- Reid MJ, Menten KM, Zheng XW, et al. 2009a. *Ap. J.* 700:137
- Reid MJ, Menten KM, Zheng XW, Brunthaler A, Xu Y. 2009b. *Ap. J.* 705:1548
- Reylé C, Marshall D, Robin A, Schultheis M. 2009. *Astron. Astrophys.* 495:819
- Rich RM. 2013. In *Planets, Stars and Stellar Systems*, Vol. 5: *Galactic Structure and Stellar Populations*, ed. T Oswalt, G Gilmore, pp. 271–346. Dordrecht, Neth.: Springer Netherlands
- Rix HW, Bovy J. 2013. *Astron. Astrophys. Rev.* 21:61
- Robin AC, Creze M, Mohan V. 1992. *Ap. J. Lett.* 400:L25
- Robin AC, Reylé C, Derrière S, Picaud S. 2003. *Astron. Astrophys.* 409:523
- Robin AC, Reylé C, Fliri J, et al. 2014. *Astron. Astrophys.* 569:A13
- Robotham ASG, Baldry IK, Bland-Hawthorn J, et al. 2012. *MNRAS* 424:1448
- Rodriguez-Fernandez N, Combes F. 2008. *Astron. Astrophys.* 489:115
- Rojas-Arriagada A, Recio-Blanco A, Hill V, et al. 2014. *Astron. Astrophys.* 569:A103
- Ruphy S, Robin A, Epchtein N, et al. 1996. *Astron. Astrophys.* 313:L21
- Ryde N, Gustafsson B, Edvardsson B, et al. 2010. *Astron. Astrophys.* 509:A20
- Sackett PD. 1997. *Ap. J.* 483:103
- Saglia RP, Opitsch M, Erwin P, et al. 2016. *Ap. J.* 818:47
- Saha K, Martinez-Valpuesta I, Gerhard O. 2012. *MNRAS* 421:333
- Saito R, Minniti D, Dias B, et al. 2012. *Astron. Astrophys.* 544:A147
- Sakamoto T, Chiba M, Beers TC. 2003. *Astron. Astrophys.* 397:899
- Salaris M, Girardi L. 2002. *MNRAS* 337:332
- Sale SE, Drew JE, Unruh YC, et al. 2009. *MNRAS* 392:497
- Salem M, Besla G, Bryan G, et al. 2015. *Ap. J.* 815:77
- Samland M, Gerhard O. 2003. *Astron. Astrophys.* 399:961
- Sanders J, Binney J. 2015. *MNRAS* 449:3479

- Sato M, Reid MJ, Brunthaler A, Menten KM. 2010. *Ap. J.* 720:1055
- Scannapieco C, Creasey P, Nuza SE, et al. 2015. *Astron. Astrophys.* 577:A3
- Schechtman-Rook A, Bershadsky MA. 2013. *Ap. J.* 773:45
- Schlaufman KC, Rockosi CM, Prieto CA, et al. 2009. *Ap. J.* 703:2177
- Schmidt M. 1963. *Ap. J.* 137:758
- Schödel R, Feldmeier A, Kunneriath D, et al. 2014. *Astron. Astrophys.* 566:A47
- Schödel R, Feldmeier A, Neumayer N, Meyer L, Yelda S. 2014b. *Class. Quantum Gravity* 31:244007
- Schönrich R. 2012. *MNRAS* 427:274
- Schönrich R, Asplund M, Casagrande L. 2014. *Ap. J.* 786:7
- Schönrich R, Aumer M, Sale SE. 2015. *Ap. J. Lett.* 812:L21
- Schönrich R, Binney J. 2009. *MNRAS* 396:203
- Schönrich R, Binney JJ, Dehnen W. 2010. *MNRAS* 403:1829
- Schuster W, Moitinho A, Márquez A, Parrao L, Covarrubias E. 2006. *Astron. Astrophys.* 445:939
- Seabroke GM, Gilmore G. 2007. *MNRAS* 380:1348
- Searle L, Zinn R. 1978. *Ap. J.* 225:357
- Sellwood JA, Binney J. 2002. *MNRAS* 336:785
- Sellwood JA. 2013. *Ap. J. Lett.* 769:L24
- Sellwood JA. 2014. *Rev. Mod. Phys.* 86:1
- Sembach K, Wakker B, Savage B, et al. 2003. *Ap. J. Suppl.* 146:165
- Sesar B, Ivezić Ž, Grammer SH, et al. 2010. *Ap. J.* 708:717
- Sesar B, Ivezić Ž, Stuart JS, et al. 2013. *Astron. J.* 146:21
- Sesar B, Jurić M, Ivezić Ž. 2011. *Ap. J.* 731:4
- Shapley H. 1918. *Ap. J.* 48:154
- Sharma S, Bland-Hawthorn J. 2013. *Ap. J.* 773:183
- Sharma S, Bland-Hawthorn J, Binney J, et al. 2014. *Ap. J.* 793:51
- Sharma S, Bland-Hawthorn J, Johnston KV, Binney J. 2011. *Ap. J.* 730:3
- Shen J, Li ZY. 2016. In *Theoretical Models of the Galactic Bulge*, ed. E Laurikainen, R Peletier, D Gadotti. *Ap. Space Sci. Libr.* 118:233–60. Cham, Switz.: Springer
- Shen J, Rich RM, Kormendy J, et al. 2010. *Ap. J. Lett.* 720:L72
- Shen ZQ, Lo KY, Liang MC, Ho PTP, Zhao JH. 2005. *Nature* 438:62
- Shull JM. 2014. *Ap. J.* 784:142
- Shuter WLH. 1982. *MNRAS* 199:109
- Siebert A, Bienaymé O, Binney J, et al. 2008. *MNRAS* 391:793
- Siebert A, Famaey B, Binney J, et al. 2012. *MNRAS* 425:2335
- Siebert A, Famaey B, Minchev I, et al. 2011. *MNRAS* 412:2026
- Siegel MH, Majewski SR, Reid IN, Thompson IB. 2002. *Ap. J.* 578:151
- Sirko E, Goodman J, Knapp GR, et al. 2004. *Astron. J.* 127:914
- Skrutskie MF, Cutri RM, Stiening R, et al. 2006. *Astron. J.* 131:1163
- Smith MC, Evans NW, Belokurov V, et al. 2009. *MNRAS* 399:1223
- Smith MC, Ruchti GR, Helmi A, et al. 2007. *MNRAS* 379:755
- Snaith O, Haywood M, Di Matteo P, et al. 2014. *Ap. J. Lett.* 781:L31
- Snowden S, Cox D, McCammon D, Sanders W. 1990. *Ap. J.* 354:211
- Snowden S, Egger R, Freyberg M, et al. 1997. *Ap. J.* 485:125
- Sofue Y, Honma M, Omodaka T. 2009. *Publ. Astron. Soc. Jpn.* 61:227
- Sofue Y, Nagayama T, Matsui M, Nakagawa A. 2011. *Publ. Astron. Soc. Jpn.* 63:867
- Sormani MC, Binney J, Magorrian J. 2015. *MNRAS* 454:1818
- Soto M, Rich RM, Kuijken K. 2007. *Ap. J. Lett.* 665:L31
- Soubiran C, Bienaymé O, Siebert A. 2003. *Astron. Astrophys.* 398:141
- Spitzer L. 1956. *Ap. J.* 124:20
- Spitzer L, Schwarzschild M. 1953. *Ap. J.* 118:106
- Stanek K, Udalski A, Szymanski M, et al. 1997. *Ap. J.* 477:163
- Stanimirović S, Dickey J, Krčo M, Brooks A. 2002. *Ap. J.* 576:773
- Steinmetz M, Zwitter T, Siebert A, et al. 2006. *Astron. J.* 132:1645

- Stewart K, Bullock J, Wechsler R, Maller A, Zentner A. 2008. *Ap. J.* 683:597
- Stinson G, Bovy J, Rix HW, et al. 2013. *MNRAS* 436:625
- Stothers R, Frogel JA. 1974. *Astron. J.* 79:456
- Strömberg G. 1925. *Ap. J.* 61:363
- Tepper-García T, Bland-Hawthorn J, Sutherland RS. 2015. *Ap. J.* 813:94
- Tian HJ, Liu C, Carlin JL, et al. 2015. *Ap. J.* 809:145
- Tissera PB, Scannapieco C, Beers TC, Carollo D. 2013. *MNRAS* 432:3391
- Toller GN. 1990. In *Galactic and Extragalactic Background Radiation, Proc. IAU Symp. 139*, ed. S Bowyer, C Leinert, pp. 21–34. Dordrecht, Neth.: Kluwer Acad.
- Tripp S, Gillessen S, Gerhard OE, et al. 2008. *Astron. Astrophys.* 492:419
- Tully R, Courtois H, Hoffman Y, Pomarède D. 2014. *Nature* 513:71
- Udalski A, Szymanski MK, Soszynski I, Poleski R. 2008. *Acta Astron.* 58:69
- Uemura M, Ohashi H, Hayakawa T, et al. 2000. *Publ. Astron. Soc. Jpn.* 52:143
- Valenti E, Zoccali M, Gonzalez OA, et al. 2016. *Astron. Astrophys.* 587:L6
- van den Bergh S. 1999. *Astron. Astrophys. Rev.* 9:273
- van der Kruit P. 1986. *Astron. Astrophys.* 157:230
- van der Kruit PC, Freeman KC. 2011. *Annu. Rev. Astron. Astrophys.* 49:301
- van der Marel RP, Fardal M, Besla G, et al. 2012a. *Ap. J.* 753:8
- van der Marel RP, Besla G, Cox TJ, Sohn ST, Anderson J. 2012b. *Ap. J.* 753:9
- van Tulder JJM. 1942. *Bull. Astron. Inst. Neth.* 9:315
- Vanhollebeke E, Groenewegen MAT, Girardi L. 2009. *Astron. Astrophys.* 498:95
- Vivas AK, Zinn R. 2006. *Astron. J.* 132:714
- Wainscoat R, Freeman K, Hyland A. 1989. *Ap. J.* 337:163
- Wang Q, Yao Y. 2012. arXiv:1211.4834
- Watkins LL, Evans NW, An JH. 2010. *MNRAS* 406:264
- Watkins LL, Evans NW, Belokurov V, et al. 2009. *MNRAS* 398:1757
- Wegg C, Gerhard O. 2013. *MNRAS* 435:1874
- Wegg C, Gerhard O, Portail M. 2015. *MNRAS* 450:4050
- Weiland J, Arendt R, Berriman G, et al. 1994. *Ap. J. Lett.* 425:L81
- Weiner BJ, Sellwood JA. 1999. *Ap. J.* 524:112
- Wetzel AR, Hopkins PF, Kim JH, et al. 2016. arXiv:1602.05957
- Wielen R. 1977. *Astron. Astrophys.* 60:263
- Wilkinson MI, Evans NW. 1999. *MNRAS* 310:645
- Williams MEK, Steinmetz M, Binney J, et al. 2013. *MNRAS* 436:101
- Xu Y, Newberg H, Carlin J, et al. 2015. *Ap. J.* 801:105
- Xue XX, Ma Z, Rix HW, et al. 2014. *Ap. J.* 784:170
- Xue XX, Rix HW, Ma Z, et al. 2015. *Ap. J.* 809:144
- Xue XX, Rix HW, Zhao G, et al. 2008. *Ap. J.* 684:1143
- Yanny B, Newberg HJ, Grebel EK, et al. 2003. *Ap. J.* 588:824
- Yanny B, Rockosi C, Newberg HJ, et al. 2009. *Astron. J.* 137:4377
- Yao Y, Wang Q. 2007. *Ap. J.* 666:242
- Yasui C, Kobayashi N, Tokunaga A, Terada H, Saito M. 2008. *Ap. J.* 675:443
- Yepes G, Gottlöber S, Hoffman Y. 2014. *New Astron. Rev.* 58:1
- Yoachim P, Dalcanton J. 2006. *Astron. J.* 131:226
- Zhang L, Rix HW, van de Ven G, et al. 2013. *Ap. J.* 772:108
- Zhao H, Spergel DN, Rich RM. 1994. *Astron. J.* 108:2154
- Zheng Z, Flynn C, Gould A, Bahcall J, Salim S. 2001. *Ap. J.* 555:393
- Zhu Z, Shen M. 2013. In *Advancing the Physics of Cosmic Distances, Proc. IAU Symp. 289*, ed. R de Grijs, 8:444–47. Cambridge, UK: Cambridge Univ. Press
- Zoccali M, Cassisi S, Frogel JA, et al. 2000. *Ap. J.* 530:418
- Zoccali M, Gonzalez OA, Vasquez S, et al. 2014. *Astron. Astrophys.* 562:A66
- Zoccali M, Hill V, Lecureur A, et al. 2008. *Astron. Astrophys.* 486:177
- Zwitter T, Matijević G, Breddels MA, et al. 2010. *Astron. Astrophys.* 522:A54